1986

The structure of Laves phases in zirconium alloys.

Xianying. Meng
University of Windsor

CANADIAN THESES

THÈSES CANADIENNES

NOTICE

The quality of this microfiche is heavily dependent upon the quality of the original thesis submitted for microfilming. Every effort has been made to ensure the highest quality of reproduction possible.

If pages are missing, contact the university which granted the degree.

Some pages may have indistinct print especially if the original pages were typed with a poor typewriter ribbon or if the university sent us an inferior photocopy.

Previously copyrighted materials (journal articles, published tests, etc.) are not filmed.

Reproduction in full or in part of this film is governed by the Canadian Copyright Act, R.S.C. 1970, c. C-30.

AVIS

La qualité de cette microfiche dépend grandement de la qualité de la thèse soumise au microfilmage. Nous avons tout fait pour assurer une qualité supérieure de reproduction.

S'il manque des pages, veuillez communiquer avec l'université qui a conféré le grade.

La qualité d'impression de certaines pages peut laisser à désirer, surtout si les pages originales ont été dactylographiées à l'aide d'un ruban usé ou si l'université nous a fait parvenir une photocopie de qualité inférieure.

Les documents qui font déjà l'objet d'un droit d'auteur (articles de revue, examens publiés, etc.) ne sont pas microfilmés.

La reproduction, même partielle, de ce microfilm est soumise à la Loi canadienne sur le droit d'auteur, SRC 1970, c. C-30.

THIS DISSERTATION
HAS BEEN MICROFILMED
EXACTLY AS RECEIVED

LA THÈSE A ÉTÉ
MICROFILMÉE TELLE QUE
NOUS L'AVONS REÇUE

NL-339 (r.86/06)

Canada

THE STRUCTURE OF LAVES PHASES IN ZIRCONIUM ALLOYS

by

Xianying Meng

A Thesis
submitted to the
Faculty of Graduate Studies and Research
through the Department of
Engineering Materials in Partial Fulfillment
of the requirements for the Degree
of Master of Applied Science at
the University of Windsor

Windsor, Ontario, Canada

1986

ISBN 0-315-31994-1

(c) Xianying Meng

ABSTRACT

The intermetallic precipitates in Zircaloy-4 have been identified as the C15 type $Zr(CrFe)_2$ Laves phase using high order Laue zones and series diffraction patterns from the transmission electron microscope. A model for the transformation from the α-Zr matrix to the $Zr(CrFe)_2$ Laves phase has been constructed using the data on orientation relationships obtained from TEM diffraction patterns.

C15 type $Zr(CrFe)_2$ Laves phase precipitates have also been found in a Zr-1.15 wt% Cr-0.1 wt% Fe alloy. Twinned, multiple twinned and dislocation structures have been found in the precipitates. The orientation relationships $(\bar{1}1\bar{1})_L // (11\bar{2}0)_\alpha$, $[110]_L // [0001]_\alpha$ between the $Zr(CrFe)_2$ Laves phase precipitates and α-Zr matrix in the Zr-Cr-Fe alloy give the same type of model for the transformation as suggested for Zircaloy-4.

Hexagonal polytype structures (H) have been found in $ZrCr_2$ and $Zr(CrFe)_2$ Laves phases in both bulk stoichiometric alloys and in precipitates in Zircaloy-4. Rhombohedral polytype structures (R) were found in both Zircaloy-4 and Zr-1.15wt%Cr-0.1wt%Fe alloys where the Laves phase is in the form of a precipitate.

Good agreement was obtained with respect to possible polytype structures between the diffraction patterns and lattice fringe images in electron microscopy. A comparison of observed and calculated relative diffraction intensities show the polytype structures to be of the 6H, 8H, 12H and 14H modifications.

DEDICATION

To my mother

ACKNOWLEDGEMENTS

The author wishes to express my gratitude to Dr. Derek O. Northwood for his supervision, guidance and friendship throughout the course of this study and during my entire tenure at the University of Windsor.

I sincerely acknowledge Dr. D.F. Watt, Dr. W.V. Youdelis and Dr. H. Yamauchi for stimulating and informative directions and discussions. I would also like to thank Mr. J.W. Robinson and Mr. G.A. Vazsonyi for the technical assistance.

I would like to thank to all of members of my family for their support and encouragement.

Finally, acknowledgements are due to the Natural Sciences and Engineering Research Council of Canada for provision of research grant and the Beijing Center of Physical and Chemical Analysis and Beijing Council of Science and Technique for their support.

CONTENTS

FIGURES

TABLES

Chapter I

INTRODUCTION

Zirconium and its alloys are widely used in nuclear power engineering and in particular in the construction of nuclear reactors since these alloys have a much lower neutron absorption per unit strength than other commercially available structural materials. In CANDU-PHW (CANada Deuterium Uranium-Pressurised Heavy Water) reactors Zircaloy-2 (1.2-1.7 wt%Sn, 0.07-0.20 wt%Fe, 0.05-0.15 wt%Cr, 0.03-0.08 wt%Ni) is used as pressure tubing and Zircaloy-4 (1.2-1.7 wt%Sn, 0.18-0.24 wt%Fe, 0.07-0.13 wt%Cr) is used as fuel sheathing. The iron content of Zircaloy-4 is increased over that in Zircaly-2 to make up for any loss in corrosion resistance resulting from the reduction of nickel content to lower levels. The Zr-2 at%Cr-0.16 at%Fe alloy (referred to as Zr-Cr-Fe alloy) was developed at the General Electric Company, U.S.A. as a fuel sheathing alloy for water-cooled reactors. Its properties include good corrosion resistance, and low hygrogen absorption in a boiling water/steam environment between 300°C and 500°C and its low susceptibility to hydrogen embrittlement.

The intermetallic phases formed from iron, chromium, nickel, tin and zirconium are stable phases in Zircaloy-2,

Zircaloy-4 and the Zr-Cr-Fe alloys because of the low solubility of iron and chromium in α-Zr, as shown in the phase diagrams i.e. Fig. 1 [1]. The distribution and morphology of these second phase particles influences the corrosion resistance and machinability of the alloys. The corrosion resistance of the Zr-Cr-Fe alloy is very dependent on metallurgical condition, and particularly the size and distribution of the $ZrCr_2$ precipitates. The good corrosion resistance is attributed partly to a uniform dispersion of fine $ZrCr_2$ particles. Northwood and Kahen [2] have reported that for optimum corrosion resistance in steam the size of $ZrCr_2$ particles must be less than 1 μm. The size and distribution of the precipitates depends on the heat treatment and other fabrication details of the tubing [3,4].

Zirconium alloys have been also studied as the hydrogen storage materials. MM'_2-type zirconium alloys, such as $ZrMn_2$, $ZrCr_2$, ZrV_2 etc. are hydrogen storage compounds. The compounds $ZrMn_2$, $ZrCr_2$ and ZrV_2 tend to form hydrides that are quite stable, thereby limiting their application. One method of lowering stability is to substitute some of the Mn, Cr or V with Fe or Co, i.e. using pseudobinary alloys of the type $Zr(M_xM'_{1-x})_2$ where M=Fe, Co, M'=Mn, Cr. In this case, stabilities can be reduced to more practical levels, without markedly lowering hydrogen capacity.

Since the binary $ZrCr_2$ and pseudobinary $Zr(Cr_xFe_{1-x})_2$ Laves phase compounds are important in both nuclear reactor

and hydrogen storage applications an investigation of their structure appeared warranted.

In 1912 Baumbauer [5] first discovered and described the phenomenon of polytypism, and since that time polytypic structures have also been found in Laves phases, such as Mg-Cu-Al, Mg-Zn-Ni etc. In the present study polytytic structures have also been found in the zirconium based Laves phases. It is difficult to both resolve the small $Zr(CrFe)_2$ Laves phase precipitates in zirconium alloys using optical microscopy and X-ray diffraction techniques, and also to identify the polytypic structures since invariably several structures can coexist in a single specimen. Fortunately electron microscopy has been developed to the extent that it is a major research tool in physico-chemical studies. In particular high resolution electron microscopy, which can give lattice or structure images, has developed rapidly in the last fifteen years and electron microscopy techniques have come to be preferred for the analysis of micro-areas for evidence of polytypism and the identification of precipitates.

In present work the structure of $Zr(CrFe)_2$ Laves phases, existing either as bulk alloys or as precipitates in the Zircaloy-4 and the Zr-Cr-Fe alloys, have been studied using transmission electron microscopy (TEM), energy dispersive X-ray spectroscopy (EDS) and a scanning electron microscopy (SEM). These studies have been supplemented by computer aided analysis of the electron diffraction patterns.

Chapter II

LITERATURE REVIEW

2.1 Laves Phase

Laves phases, with the general formula MM'_2, can have one of three related structures, namely the $MgCu_2$, $MgZn_2$, or $MgNi_2$ structures based on magnesium. These three structures correspond to C15-cubic, C14-hexagonal and C36-hexagonal structures respectively.

The M or M' atoms may come from any part of the periodic table, and the same element may play different roles in two Laves phases. The three structures, i.e. C14, C15 and C36, are closely related. The main reason for the existence of the three phases is considered to lie in the fact the geometrical space of the lattices can be conveniently filled in more than one way when $D_M/D_{M'}=1.225$, where D represents the atomic diameter.

The structures may be described in terms of hexagonal lattices, in which the atomic arrangement leads to the assumption of axial ratios in the proportions 2:3:4 for $MgZn_2$, $MgCu_2$ and $MgNi_2$ respectively. In each case M' atoms occupy the corners of tetrahedra, joined alternately point-to-point and base-to-base in $MgZn_2$, but base-to-base in $MgCu_2$, Fig. 2(a-c) [6,7,8]. The $MgNi_2$ structure contains

both types of junction. The larger atoms, M, are accomodated in holes in the arrangement of tetrahedra, and are disposed relatively to each other. The M atoms form double layers with a hexagonal network, such that each M atom of the upper layer is directly above one in the lower layer. Thus the C15 type structure can be described as ABCABC... and the C14 and C36 types as ABAB... and ABACABAC... respectively, as shown in Fig. 2(d-f). Again the $MgNi_2$ structures contain a mixture of both types of M-atoms arrangement.

There has been little discussion of the factors which affect the choice of one structure rather than another. It is impossible to assign characteristic electron:atom ratios to phases crystallizing in the $MgZn_2$, $MgCu_2$ and $MgNi_2$ types of structure, but there is evidence that valency considerations are important in certain complex alloys for Laves phase formation. The relationship between structure and valency in ternary magnesium alloys has been studied by Laves and Witte [9], and the results are summaried in Fig. 3. The main trends noted are as follows: (1) On increasing the electron: atom ratio of $MgCu_2$ by substituting for copper a metal of higher valency, the cubic structure is replaced by the $MgNi_2$ structure at approximately 1.8 electrons per atom, and by the $MgZn_2$ structure as the electron: atom ratio approaches 2.0. (2) The reverse sequence of changes occurs on reducing the electron:atom ratio of $MgZn_2$ by substituting zinc with a metal of lower valency. The for-

mation of the $MgNi_2$ structure at electron to atom ratios between the other two types might suggest that the effective valency of nickel in these ternary phases is not zero, but between 1.0 and 2.0. It is more likely that the $MgNi_2$ structure is a structural intermediate in which periodic "faulting" facilitates the change from the $MgZn_2$ arrangement to that of $MgCu_2$. Of 233 binary Laves phases reported, 68 percent had the C15 $MgCu_2$ type structure, 30 percent the C14 $MgZn_2$ type structure and only two percent had the C36 $MgNi_2$ type structure. In addition to the binary Laves phases many Laves phases have been reported to form in pseudobinary or ternary systems.

The Laves phases of zirconium based systems have principally been studied because of the excellent hydrogen storage capacity of binary and pseudobinary compounds and also because the intermetallic precipitates which form in commercial zirconium alloys affect the properties of these alloys. Table 1 [10,11] summarizes the published data for crystal types, lattice parameters, atomic size ratios and melting points for binary zirconium Laves phases. $ZrCr_2$ has both the C15-$MgCu_2$ type and the C14-$MgZn_2$ structure. $ZrFe_2$ is reported only to form the C15 cubic structure. Fig. 4 gives the stability ranges for binary ZrM'_2 Laves phases, where M' is either V, Cr, Mn, Fe, Co or Ni. Fig. 5 shows the systematic variation of crystal structure type with the position in the periodic table of the M' element for a constant M element.

The electron:atom ratios for binary or pseudobinary zirconium Laves phases are given in Table 2. According to Zr-Cr phase diagram the $ZrCr_2$ intermediate phase exists at 53 wt%Cr in the Zr-Cr system [12,13].

As previously noted, some binary or pseudobinary Laves phase alloys have potential for use as hydrogen storage materials. The hydrogen capacities, activation temperatures and absorption pressures of some of these Laves phase compounds are given in Table 3 [14,15].

2.2 Polytypism

2.2.1 Description of polytypism

Polymorphism has been recognized as the ability of the same chemical compound to exist in more than one crystalline form. Polytypism is defined as the ability of a substance to crystallize into a number of different modifications, in all of which two dimensions of the unit cell are the same while the third is a variable integral multiple of a common unit. The different polytypic modifications can be regarded as built up of layers of structure stacked parallel to each other at constant intervals along the variable dimension. The two unit-cell dimensions parallel to these layers are the same for all the modifications. The third dimension depends on the stacking sequence, but is always an integral multiple of the layer spacing. Different manners of stacking these layers may result in structures having not only

different morphologies but even different lattice types and space groups. The polymorphic modifications of a compound normally form under different conditions of temperature and pressure. Each modification has its own range of thermodynamic stability and is regarded as a different phase. Phase transitions are governed by the condition of minimum free energy and follow the Gibbs phase rule. The velocity of transition then depends on the energy barrier opposing the transformation. However, invariably several structures can coexist in a single specimen of polytypic structure.

The phenomenon of polytypism was first discovered in SiC in 1912. Subsequently it has been reported in ZnS, CdI_2, $CdBr_2$, PbI_2, mica, Au-Mn alloys, $NbSe_2$, $TaSe_2$, Co-rich Sm-Co, β'''-alumina and other alloys and minerals. So far more than one hundred kinds of polytypes have been reported [16-26]. Some polytypism has been reported in Laves phases such as Mg-Cu-Al, Mg-Cu-Ni, Mg-Cu-Zn, Mg-Zn-Ag, Mg-Zn-Ni and other Mg based systems [27-32].

2.2.2 Notations Used to Describe the Polytypes

With the discovery of new polytypes and polytypic compounds, e.g. SiC is now known to have over 40 modifications, a suitable system of nomenclature had to be developed for describing the various polytypes and their structures. The special notations commonly employed to distinguish the polytypic modifications are the Ramsdell notation, the classical ABC notation and the Zhdanov symbol.

These notations are described below. There are some other notation used to represent polytypic structures but they are not used as extensively as the Ramsdell, ABC or Zhdanov notations.

2.2.2.1 The Ramsdell notation

The different polytypes consist of identical layers of atoms stacked over each other at constant intervals and differ only in the lattice type and in the number of layers in the unit cell. Ramsdell [33] represented the polytype by the number of layers in the unit cell and added to it the letter H or R to specify the lattice type. Thus a symbol nH represents a structure with an n-layered repeat period along c and a primitive hexagonal lattice, while mR denotes a structure with an m-layered repeat period along c and a lattice whose primitive unit cell is rhombohedral. This simple designation uniquely distinguishes each polytype except when two types have the same lattice as well as the same repeat period along c and differ only in the stacking sequence of the layers in their unit cell. Practice is to distinguish these polytypes by attaching subscripts a, b, c, etc., to the letter denoting the lattice type. The notation is simple and brief, but it does not give any information on the actual arrangement of layers in the unit cell. It is, however, the only notation suitable to designate polytype with known lattice but undetermined the stacking sequences of atomic arrangement.

2.2.2.2 The classical ABC notation

In describing the structure of different polytypes by the classical ABC notation it should be noted that A, B, and C do not necessarily represent single plane layers of atoms. The unit layer of structure may be polyatomic, and in such cases the letter A, B, or C defines the position of one kind of atoms in the unit layer, the positions of the other atoms in the layer being fixed relative to these. Thus to be exact the layers A, B, and C should be written as Aα, Bβ, and Cγ, where, for example, in SiC the Roman letter represets the Si atoms and the Greek letters represent the carbon atoms. For the sake of brevity, the Greek letters are often omitted. Although this representation gives a complete description of the structure, it does not reveal the symmetry or lattice type directly, and becomes increasingly unwieldy for polytypes with large numbers of layers in the unit cell [25].

2.2.2.3 The Zhdanov symbol

The Zhdanov [34] symbol consists of pairs of numbers in which the first denotes the number for ABC stacking sequence and the second the number for ACB stacking sequence. For example, type 15R is written as $(23)_3$, which implies that the stacking sequences are ABC'B'A'CAB'A'C'BCA'C'B', and type 21R as $(34)_3$. This notation is most convenient for representing the structure of long-period polytypes.

2.2.3 Theories of polytypism

The first relatively satisfactory explanation of the polytypism came with the advent of the screw-dislocation theory of crystal growth, where Frank [35,36] interpreted the various polytypes as originating by growth around screw dislocations in certain basic structures. Jagodzinski [37,38] regarded thermodynamics considerations as more important and proposed a layer-transposition mechanism based on the vibration entropy of the structure, for the formation of the different polytypes. Schneer [39] considered the different polytypic structures to be related by higher (or second) order transformations because of their being energetically almost identical. Peirst [40] has attempted an explanation based on influence of thermal vibrations on the growth front at the time of crystallization. A brief description of these theories is given below.

2.2.3.1 The dislocation theory of polytypism

Frank suggested that SiC crystals grow initially, at high supersaturations, into thin plates, by the surface-nucleation mechanism in accordance with the theory of growth of perfect crystals. Due to nonuniform distribution of impurities or thermal radiation these plates become self-stressed. If the stress exceeds the theoretical yield stress the plane could be sheared. This produces steps on the crystal face. If the shear is by a uniform amount, a screw dislocation will be created. Screw dislocations of different

Burgers vectors may create different polytypes. When the Burgers vector of the screw dislocation is an integral multiple of the height of the parent unit cell, then the resulting structure will be the same as the basic structure. On the other hand, a screw dislocation with a Burgers vector which is a nonintegral multiple of the height of the parent unit cell would give rise to a new polytype whose periodicity along c is determined by the height of the exposed screw-dislocation ledge.

Some experiments show that the observed and measured step height of growth spirals is directly correlated to the height of the X-ray unit cell. This is clear support for the dislocation theory of polytypism. The step heights of growth spirals have been measured [41-43] for two kinds of 6H crystals of SiC, with the step heights being 15.2 Å and 15.1 Å respectively. Multiple-beam interferometery for 6H structure of SiC gave the height of the X-ray unit cell as 15.09 Å. Data for different SiC polytypes where a direct correlation has been found between the spiral-step height and height of the X-ray unit cell are summarized in Table 4. Forty's observations [44] on the growth of CdI_2 and PbI_2 have also lent support to the dislocation theory of polytypism. Amelinckx [45,46] has also shown that the step height of growth spirals on mica is equal to the height of the X-ray unit cell.

2.2.3.2 Jagodzinski's disorder theory

Jagodzinski [37,38] expressed doubts about the screw-dislocation theory of polytypism and pointed out that the energy required for the creation of an edge dislocation with a Burgers vector $\frac{1}{3}a + \frac{2}{3}b$ or $\frac{2}{3}a + \frac{1}{3}b$, or an integral multiple of these, would be much less than that required for the creation of screw dislocations with large Burgers vectors. The arrangement of atoms in a close packed structure like that of SiC would particularly favor the creation of such edge dislocations in the (0001) plane, and these layer dislocations would completely destroy any order created by a screw dislocation.

He also pointed that the high energy required for the creation of a screw dislocation can come from the crystal structure only when the crystal has grown to a considerable volume, by which time it would have already settled down to a certain structure. Screw dislocations can, therefore, cause growth only in the later stages, thereby determining only the surface structure. No new structure would thus result and the formation of different polytypic structures cannot be due to the screw dislocations. Whether cubic or hexagonal SiC forms at different temperatures, is controlled by thermodynamic factors, according to Jagodzinski. Using SiC as an example, it can be theoretically shown that a completely one-dimensionally disordered structure is predicted, and the formation of ordered types appears to be thermody-

namically anomalous. This is because all structures of SiC, even the disordered types, have the same potential energy since the atoms have an identical environment of the first and second neighbors. The density of the different structures being the same, the free energy would be minimized by maximum entropy. The entropy of the structure would consist of two parts: (1) the configurational entropy and (2) the vibration entropy. The configurational entropy increases with increasing disorder, whilst the vibration entropy tends to decrease. The sum of the two has two maxima with the second maxima corresponding to the partly disordered polytypic structures. The vibration entropy is expected to favor ordered states.

Jagodzinski assumed that the formation of the small-period polytypes like 4H, 6H and 15R is governed by potential-energy considerations, while that the long-period structures is determined by the vibration entropy. The formation of long-period SiC structures is not thermodynamically anomalous, but is characterized by a maximum of the configuratinal and vibrational entropies of the structure. The distribution of the various structures is thus governed by thermodynamic considerations.

In order to characterize the polytypic structures a "fault-order degree" has been defined as the ratio of the number of faults to the total number of double layers in the structure. They can be calculated by thermodynamic formulas

and determined experimentally from the X-ray diffraction photographs. Calculated and determined fault-order degrees show good agreement for SiC, ZnS and CdI_2 crystals.

The limitation of the disorder theory of polytypism is that the theory is based on a large number of assumptions, many of which can be questioned. The relationship between the occurrence of a structure and the temperature is not well established. The theory also does not predict the formation of a structure series so predominantly displayed by SiC. Finally the faultless ordering of some of the long period polytypes is difficult to understand using this theory.

2.2.1.3. The higher-order transformation theory

Schneer [39] has treated polytypism as a cooperational phenomenon, and he believed polytypes to be related by phase transformations of the higher order, analogous to ferromagnetic transitions and those of order-disorder in alloys. The different polytypes represent intermediate states in a second-order transition between the cubic and hexagonal structures. The observed polytypes of a compound are characterized by maximum numbers of interaction contacts between layers in unlike state and correspond to potential minima. Schneer considers polytypic transformations as transformations of the second order with intermediate transformations of higher order. The specific volumes, entropies, and probability distributions vary continuously with temperature.

All derivatives of heat capacity, thermal expansion, resistivity, compressibility, etc. with respect to temperature may rise anomalously in the transition range of temperature. Minute differences in temperature or in the degree of approach to equilibrium may bring about major differences in periodicity.

There is little experimental evidence in favor of the theory. In ZnS there is a transformation from the cubic ZnS to the hexagonal ZnS with increase of temperature. The different ZnS polytypes have been synthesized between 870° and 905°C, a range that lies below the transition temperature of ~1024°C. The ZnS polytypes can be considered to be intermediate states between the β-ZnS and α-ZnS (2H).

Phase transformations of the second order are disordering transformations, and are characterized by a critical temperature at which the disorder attains complete randomness. However, it has not been possible to associate definite polytypes with specific temperatures, and no phase transformations between polytypes have been observed to occur. One SiC polytype does not go over into another by heating. There is thus nothing to indicate that different SiC polytypes are related by second- or higher-order transformations.

2.2.3.4 Polytypism and thermal vibrations in the structure

Peibst [40] has attempted to explain the formation of polytypes by the influence of thermal vibrations of the crystal structure during growth. According to the theory, different polytypes form under different conditions of growth, and the spectrum of thermal vibrations, which depend on the structure of the nucleus and the growth temperature, are of predominant influence. However the assumptions in this theory have not been confirmed by any experimental evidence.

2.2.3.5 Summary

A very large number of factors have been suggested as influencing the phenomenon of polytypism. The temperature and rate of crystallization, the presence of impurities, the screw and edge dislocations created during growth, the thermal vibrations of the structure, and the electron energy band gaps, all appear to effect the formation and distribution of polytypic structures to different extents. The theories advanced are all based solely on one or another of these factors, and have been unable to provide a satisfactory explanation for all the observed facts. The need is thus apparent for a single consistent theory of polytypism embracing all these factors. Based on the more recent investigations into the origin of polytypes, their formation appears to be governed by growth mechanisms and screw dislocations and thermodynamic considerations are of primary importance.

2.3 Precipitates in Zirconium Alloys

Material properties such as corrosion resistance, grain growth and mechanical behaviour of zirconium alloys are known to depend strongly upon the composition, distribution and morphology of precipitates in these alloys. Therefore numerous investigations have focused on these precipitates. With the development of electron microscopy techniques such as TEM, SEM, and more particularly EDS and STEM (scanning transmission electron microscopy), the composition and structure of the precipitates have been more closely defined since all of these electron microscopy techniques can provide information from different micro-areas of the specimen. Table 5 gives a summary of published data on precipitates in zirconium alloys.

Chapter III

EXPERIMENTAL

3.1 Materials and Heat Treatment

Three types of zircorium alloys, namely Zircaloy-4, Zr-1.15wt%Cr-0.1wt%Fe (referred to as Zr-Cr-Fe alloy hereafter) and bulk stoichiometric $Zr(CrFe)_2$ alloys, have been investigated.

3.1.1 Zircaloy-4

Two kinds of Zircaloy-4 product, tube and rod, were studied. The chemical analyses of the Zircaloy-4 specimens are given in Table 6. The tube specimens denoted as a,b,c, were cut from fuel sheathing of 15.24mm diameter and 0.4 mm wall thickness. The diameter of the rod, specimen d, was about 7 mm. The specimens of Zircaloy-4 were encapsulated in evacuated quartz capsules and solution treated at 1100°C for 5 min. for specimens a, b, c, and 15 min. for specimen d. Following solution treatment, the encapsulated specimens were cooled in circulating air.

3.1.2 The Zr-Cr-Fe alloy

For Zr-Cr-Fe alloy, 10 mm square specimens were cut from 1.3 mm thick sheet using a low speed diamond saw. The specimens were also encapsulated in evacuated quartz capsules and solution treated for 30 min at 1050°C following by water quenching. The quenched specimens were then resealed into evacuated quartz capsules, heated at 760°C for 10.5 h. then air cooled.

The chemical composition of the Zr-Cr-Fe alloy is given in Table 7.

3.1.3 $Zr(CrFe)_2$ stoichiometric alloys

Five kinds of bulk stoichiometric $Zr(Cr_xFe_{1-x})_2$ alloys, (where x=1, 0.75, 0.55, 0.2 and 0), were studied as cast alloys. The alloys was prepared by melting in ar arc furnace under a high purity argon atmosphere. High purity elements were utilized, i.e. 99.9% pure zirconium and 99.99% pure chromium. The alloys were melted four times to ensure compositional uniformity.

3.2 Preparation of Specimens for TEM

The Zircaloy-4 and Zr-Cr-Fe specimens for transmission electron microscopy were first ground on silicon carbide papers down to a thickness of about 0.07 mm. These specimens were then thinned using a twin-jet electropolishing technique in a solution of 1:4 perchloric acid : ethyl alcohol. The electropolishing temperature, voltage and current

were -30°C, 10-13 volts and 15 microamperes for Zircaloy-4 and -30 to -34°C, 20 volts, and 25 microamperes for Zr-Cr-Fe alloys respectively.

The bulk stoichiometric $ZrCr_2$ and pseudobinary Laves phase alloys were very brittle and powders of these alloys were made by light grinding using a pestle and mortar to produce the finer powders. A suspension of the powder was made with alcohol and separated in an ultrasonic bath.

To produce high resolution lattice images a support foil is required for the specimen. The drops of the suspension containing the powder were deposited onto a holey support film. Some powder particles would sit right in the holes in the support film and high resolution observation was possible without any added support foil under the powder.

The Holey supporting film is commonly used for the astigmatism correction by observing the Fresnel fringes at a small hole. To prepare the holey foil an emulsion of glycerol in 0.25% Formvar solution is used. A cold (0° C) glass microscope slide is dipped in the solution, allowed to dry and the Formvar replica floated off onto distilled water. This film contains holes arising from the droplets of glycerol. The film is scooped up onto a coarse grid which has on it several support grids, which are 200 mesh and 3-3.2 mm diameter. After drying, a carbon film about 10 nm thick is evaporated on to the Formvar film in a vacuum deposition device [62]. The carbon film is used for astigmatism correction at high resolution as described in section 3.6.

3.3 Electron Diffraction Analysis

The thin foil specimens of Zircaloy-4 and Zr-Cr-Fe and the powders of bulk stoichiometric $Zr(CrFe)_2$ alloys were examined on a JEOL 100CX TEM equipped with the double tilt specimen holder. The microscope was operated at 100 kV. Identification of the structure of the Laves phases was accomplished by electron diffraction analysis.

In TEM the incident electrons interact with the specimen giving rise to absorbtion, phase shifts and diffraction of the electron beam. Depending on operating conditions one of several types of image is formed by the objective lens and this image is then magnified by the intermediate and projector lenses.

The electron wavelength λ is given by [63]

$$\lambda = \frac{12.26}{E^{\frac{1}{2}}(1+0.9788\times10^{-6}E)^{\frac{1}{2}}} \text{ Å} \qquad (1)$$

where E is accelerating voltage. For a 100 KV accelerating voltage the wavelength of the electrons is 0.0037 nm. When the crystal is correctly oriented and the conditions of Bragg diffraction are satisfied an electron diffraction pattern will be formed at the back focal plane of the objective lens, as shown in Fig. 6. For the electron diffraction analysis of the structures of the Laves phases, 76 cm and 120 cm camera lengths were used. The camera constants of the TEM must first be calibrated. In the present study two methods

of the calibration were used. For stoichiometric $Zr(CrFe)_2$ alloys the diffraction patterns of standard Al thin foil were used to calibrate the camera constant. For Zircaloy-4 and Zr-Cr-Fe alloys the calibration of the TEM was performed using the diffraction pattern of α-zirconium matrix, as an internal standard and in-situ calibration.

The distributional curves of relative intensity of the electron diffraction patterns for the polytype structures were measured using a semiautomated device consisting of a microdensitometer and chart recorder. The integral area under curves was measured with a commercial graphic data image analyzer. Observed relative intensities were calculated using these integral areas. Calculated relative intensities based on structure factor are obtained by computer methods.

3.4 Double Tilt Stereometric Stage and Construction of Reciprocal Plane of Crystal

A modern TEM is in generally equipped with a goniometer stage. The JECL 100CX TEM has two types of goniometer stage, a double tilt and a rotation-tilt stage. The double tilt holder can tilt the specimen about two orthogonal axes, labelled the X and Y axes. One axis is normal to the incident electron beam, while the other axis is in the specimen plane. The tilt angles in the two directions can be varied by ±45°. The rotation tilt holder can tilt the specimen

about a fixed axis normal to the beam, and rotate the specimen about an axis normal to the specimen plane. Tilt angles of ±60° and a rotation of 360° are possible. In present work the double tilt holder was used.

The effective tilt angle can measured using a stereogram. The axes of crystal plane is normal to the reciprocal vector of the crystal plane. Therefore the pole of the reciprocal plane should be on a great circle of a stereogram while the axes of the crystal plane is parallel to incident beam. If the diffraction spot is invisible in a diffraction pattern the pole of the reciprocal lattice plane should be inside of the circle of the stereogram. For identification of a unknown crystal the basal plane of the crystal cell should be obtained and observed by electron diffraction. In practice the specimens were tilted with double tilt holder to get a close row of diffraction spots. The close row was assumed to be associated with a basic vector of the crystal cell, i.e. reciprocal vector a* or b* or c*. By continuing to tilt the specimen the diffraction patterns which included the close row were obtained. The tilting procedures are illustrated in as Fig. 7 on a stereogram. Here P_0 is the pole of a reciprocal lattice plane whose diffraction pattern is invisible in a diffraction pattern. After tilting the crystal x degrees, in Fig. 7 $x=x_0+x_1$, and y degrees, the diffraction pattern and the pole of the reciprocal plane was labelled as p in the stereogram. According to geometry the effective tilting angle α is given by

$$\tan \alpha = (\tan^2 x+\tan^2 y+\tan^2 x \cdot \tan^2 y) \qquad (2)$$

For the rotation-tilt holder the effective angle α is given by [64-66]

$$\tan\alpha = \tan x \cdot \cos\omega \qquad (3)$$

where ω is the rotation angle.

From diffraction patterns the interplanar distances , d, can be calculated. According to the diffraction geometry, $Rd=\lambda L$, and the relation of $\vec{g}=1/d$, where $\vec{g}$ is reciprocal lattice vector, series $\vec{g}$, which are normal to the a*, could be obtained. Using data on tilt angles and the corresponding reciprocal vector $\vec{g}$, a reciprocal lattice plane which is normal to the a* can be constructed.

For identification of the Laves phases a double tilt stage was used and the corresponding reciprocal lattice planes were obtained.

3.5 Bright and Dark Field Images

Bright field (BF) and dark field (DF) imaging are the most commonly used imaging modes for TEM of crystalline materials. The ray paths for the two modes are shown in Fig. 8 [63]. A 20 μm aperture is inserted in the back focal plane of the objective lens to intercept the diffracted beam and only allow the transmitted beam to form an image, and this image is known as the BF image. Two methods are used to form DF images. When the objective aperture is displaced from the optic axis so as to intercept the transmitted beam,

only the diffracted beam is used to form to the dark field image. This method is easy and fast to use and was the method used to determine the crystal plane from which the incident beam was reflected. However a poor quality image is produced by this method because of the additional spherical aberration and astigmatism present when the electron path is not close to the optic axis. The DF images shown in present work were made using the centred dark field imaging (CDF) mode, as illustrated in Fig. 8(b). When this method is used the transmitted beam is tilted by using an electromagnetic beam tilt device and the diffracted electron beam travels along the optic axis.

3.6 High Resolution Lattice Imaging

The aim of high resolution electron microscopy is to directly image and identify the position of an atom or group of atoms in solid. Unfortunately there is usually no simple one to one correspondence between contrast on a micrograph and atomic positions in the specimen for high resolution experimental conditions. Many computer methods have been developed for the calculation of image contrast. To obtain high resolution images, the microscope must be kept in excellent condition. For the JEOL 100CX, the stability of accelerating voltage was better than 2×10^{-6}/min., and the spherical aberration constant is 4.5 mm. So far, for best high resolution TEM the spherical aberration constant is 0.7 mm.

The procedures for obtaining high resolution lattice images are as followings:

(1) Fill the anti-contamination trap with liquid nitrogen.

(2) Align the electron microscope as described in the instruction manual. This involves checking the illuminating system so as to obtain the maximum possible source brightness when using a small illuminating aperture. The voltage center and current center should also be checked.

(3) Select a region of the thin foil specimen which lies above the hole in the holey supporting film at low magnification. The area gives rise to a high resolution image, since there is no part of the support foil to interfere with the resolution in the electron microscope image.

(4) Tilt the crystal to obtain the required orientation of the crystal.

(5) In order to prevent contamination of the crystal from prolonged exposure to the electron beam, the operating conditions of the electron microscope are kept constant but the specimen is moved so that a neighbouring area of the crystal is illuminated. This usually requires a correction for astigmatism.

The setting of the objective stigmator is critical when operating at high resolution. The astigmatism has been corrected for by adjusting the stigmator so that a Fresnel fringe is symmetrical at low magnification. A more accurate

correction is needed at high resolution. This can be done by observing the structure of the thin amorphous support carbon film at the higher magnification where the high resolution image is to be taken. The procedure is to first focus the binocular, then adjust both the focus controls and the stigmator to obtain an image of the grainy carbon structure such that there is no preferential direction evident.

(6) For taking the high resolution lattice images the specimen was first tilted so that the [010] direction in the Laves phases was parallel to the incident beam. To obtain the detailed lattice images an objective aperture of 120 μm was used. This large aperture can provide many diffracted beams to contribute to the contrast of the image. The lattice image is then focused and a through-focus series of images are produced. The high contrast images are found in the under-focus conditions [67].

3.7 Energy X-ray dispersive spectrography (EDS) qualitative analysis

In order to identify the composition of the Laves phase precipitates, EDS qualitative analysis technique was used. The thin foil was glued to a mounting stub for the SEM with conductive paint. Secondary electron imaging was used to observe the topography and then the distribution of alloying elements was analyzed with the Kevex X-ray energy dispersive system which was fitted to the Nanolab 7 SEM. The following guidelines were used when performing the EDS analysis:

(1) The EDS spectrometer was first calibrated so that the peak position was within 10 eV of the tabulated value.

(2) When optimizing the analysis for a single X-ray line, an accelerating voltage approximately 1.5 to 3 times the critical excitation voltage for that line was used. The emission energies of the relative elements are given in Table 8 [63,64,68,69]. In general, to provide an adequate overvoltage in the range 1-10 kV, a 30 kV beam energy (accelerating voltage) was used.

3.8 Computer methods

In the present study computer methods were used to: index diffraction patterns; to construct the model illustrating the relationships between the Laves phase precipitates and the α-Zr matrix; to calculate the diffracted intensities using structure factors; and to plot the distribution curves of relative intensities. The computer methods are described below briefly, and the calculation of relative diffraction intensities is discussed in Section 5.2.

3.8.1 Indexing of electron diffraction patterns

The correct indexing of a diffraction pattern should match both the appropriate lattice plane spacings, and the interplanar angles. Since some diffraction patterns can be indexed as either the cubic or the hexagonal structures, the interplanar angles between two zone axes of the diffraction pattern, as measured experimentally, should be matched the calculated values for the cubic or the hexagonal lattice.

In present work since the $Zr(CrFe)_2$ Laves phases can have either the C14 or C15 structures, and the α-Zr matrix has hexagonal lattice, programs have been written tc index cubic and hexagonal structures. For the cubic lattice one inputs the lattice parameter a, and calculates d and α using the crystallographic formula

$$d=\frac{a}{(h^2+k^2+\ell^2)^{\frac{1}{2}}} \tag{4}$$

and

$$\cos\alpha=\frac{h_1h_2+k_1k_2+\ell_1\ell_2}{((h_1^2+k_1^2+\ell_1^2)(h_2^2+k_2^2+\ell_2^2))^{\frac{1}{2}}} \tag{5}$$

for hexagonal structure one inputs the lattice parameters a and c, and calculats d and α using the fcrmula

$$d=\frac{1}{(\frac{4}{3}\frac{h^2+hk+k^2}{a^2}+(\frac{\ell}{c})^2)^{\frac{1}{2}}} \tag{6}$$

and

$$\cos=\frac{h_1h_2+k_1k_2+(h_1k_2+h_2k_1)+3a^2\ell_1\ell_2/4c^2}{(h_1^2+k_1^2+h_1k_1+3a^2\ell_1^2/4c^2)(h_2^2+k_2^2+h_2k_2+3a^2\ell_2^2/4c^2))^{\frac{1}{2}}} \tag{7}$$

Thus every crystal plane spacing and interplanar angle for both cubic and hexagonal structures was obtained.

3.8.2 Construction of the model of orientation relationship

Based on relationships between the diffraction patterns for the precipitates and the matrix, orientation relationship were found. To illustrate these orientation relation-

ships, the coordinates of atoms and the bond lengths for both cubic and hexagonal structures were the input data to a plot package.

3.8.3 SAS packages

SAS, Statistical Analysis System, is an integrated system for data management and statistical analysis. SAS has a wide variety of statistical procedures. Simple ones include mean, frequence and correlation. More complex procedures include discriminant analysis, categorical analysis, regression analysis, analysis of variance and so on.

SAS has a graphics system to produce histograms, pie charts, star charts, block charts, line graphs, contour plots, plot of three-dimensional data and variety of maps and projection.

In present study the SAS/GRAPH system was called by the Job Control Language. The "relative Intensity %" and crystal plane indices "HKL" are entered as data names. The data, e.g. HKL is 012 and the relative intensity is 100%, are then entered in data cards. Symbols such as "STAR", "DIAMOND", etc. are then entered as symbols for the plots. The SAS program will then plot the curves giving the relative intensity distribution.

Chapter IV

RESULTS

4.1 $Zr(CrFe)_2$ Laves phases precipitates in Zircaloy-4

Many precipitates were present and they were distributed heterogeneously at the boundaries of the Widmanstätten - zirconium plates. Figure 9 shows the morphologies of these precipitates.

Typical EDS spectra of the precipitates are given in Figure 10. According to the spectra the precipitates are composed of Zr, Cr and Fe. A nickel peak in the EDS spectrum has been found for some precipitates, e.g. Figure 10(c).

The selected area electron diffraction patterns (SAD) for the precipitates and α-Zr are shown in Fig. 9(b). Analysis of precipitates by SAD and EDS, Fig. 10, shows them to be the $Zr(CrFe)_2$ Laves phase with a C15-type cubic structure.

For the detailed identification of the structure of the $Zr(CrFe)_2$ Laves phase, the specimen was tilted around the $(111)^*$ reciprocal vector to get nine diffraction patterns, all of them involving the $(111)^*$ reflection. This was done for all of specimens identified as a, b and d in Table 6. These diffraction patterns are shown in Fig. 11. Table 9

summarises the interplanar angles between two reciprocal planes both as measured by electron diffraction and as calculated using crystallographic formulas. The agreement between experimental and calculated values is excellent, thus giving confidence to the identification of the precipitates as the C15 type $Zr(CrFe)_2$ Laves phase structure.

The C15 $Zr(CrFe)_2$ Laves phase precipitates have also been found within the grains in sample d; see Fig. 12. Dark field images were used to check the diffraction pattern of the precipitates, e.g. Fig. 12(b), and confirm the structure of the precipitates.

Hexagonal $Zr(CrFe)_2$ precipitates were also found in specimen b and c of Zircaloy-4. Fig. 13 shows a dark field image and a SAD of this type of precipitate in specimen c. The diffraction pattern for the matrix is the [0001] zone axis of the α-zirconium. The precipitate SAD is for the $[1\bar{1}00]$ zone axis of the $Zr(CrFe)_2$ precipitate. The SAD for $(01\bar{1}0)^*$ was used as a standard to calculate the camera constant of the TEM. The lattice parameters of the hexagonal $Zr(CrFe)_2$ were found to be a=0.4914 nm, and c=0.8210 nm.

Fig. 14 is a set of diffraction patterns for the hexagonal $Zr(CrFe)_2$ precipitates in sample b. The zone axis of SADs from the precipitates is $[01\bar{1}0]$. The zone axis for matrix SAD is $[2\bar{2}01]$ in Figs. 14(a,b) and $[3\bar{2}\bar{1}1]$ in Figs. 14(c,d). Using the matrix SAD as a standard, the lattice parameters of the precipitates were found to be a=0.5034-0.5075 nm and c=0.8209-0.8275 nm.

The SADs indicate that long period stacking variants of the $Zr(CrFe)_2$ Laves phase exist in Zircaloy-4. For example the diffraction spots of the type 10L and 20L show 2H, 6H and 10H stacking to be present in Figs. 14(a-c). The SAD in Fig. 14(d) shows a heavy stacking fault. The morphology of the precipitates when viewed at high magnification in TEM also indicated stacking faults to be present. Mostly the stacking direction of [0001] was parallel to the boundary of the α-Zr as is shown in Fig. 15.

4.2 $Zr(CrFe)_2$ Laves phases precipitates in Zr-1.15wt%Cr-0.1wt%Fe alloy

Although both the C14 and C15 type $Zr(CrFe)_2$ Laves phases were found in Zircaloy-4, only the C15 type cubic $Zr(CrFe)_2$ Laves phases precipitates have been found in Zr-1.15wt%Cr-0.1wt%Fe alloy. The $Zr(CrFe)_2$ precipitates were found at both the grain boundaries and within the α-Zr grains, Fig. 16. As was the case for Zircaloy-4 many of the larger precipitates were distributed at grain and sub-grain boundaries, e.g. Fig. 16(c,d). X-ray energy dispersive analysis indicated that Zr, Cr and Fe were always present in the precipitates. The precipitates were identified as C15 type Laves phase. The diffraction patterns of $[5\bar{3}2]$, $[1\bar{1}\bar{2}]$, $[0\bar{1}\bar{1}]$, $[\bar{3}25]$, $[\bar{2}13]$ and $[1\bar{1}0]$, $[4\bar{3}1]$, $[3\bar{2}1]$, $[\bar{5}\bar{3}2]$, $[\bar{4}31]$, $[\bar{3}21]$ and $[\bar{5}32]$ zone axes, which are obtained by tilting the sample around {111} reciprocal lattice vectors, have been

recorded successively. A partial of a set of these diffraction patterns is shown in Figs. 17 and 18. The angles between zone axes show excellent agreement between experimental and calculated values, as is can be seen in the (110) stereographic projection for the cubic structure in Fig. 19.

The $Zr(CrFe)_2$ Laves phase precipitates in the Zr-Cr-Fe alloy appear to be twinned; see diffraction patterns such as those in Figs. 17 and 20. (111) and [111] are the twin plane and twin axes respectively in the fcc system. To differentiate between the α-Zr matrix and twinning matrix of $Zr(CrFe)_2$ Laves phase, the term untwinned is used to describe the twinning matrix. By a rotation of 180 degrees about the <111> twin axes of the $Zr(CrFe)_2$ Laves phase precipitates, mirror images of the untwinned diffraction patterns are obtained. Indexed diffraction patterns due to twinning for the $[1\bar{1}\bar{2}]$, $[0\bar{1}\bar{1}]$, $[\bar{3}2\bar{5}]$ and $[\bar{2}1\bar{3}]$ orientations are given in Fig. 18. The twinning diffraction spots are clearly observed except for the diffraction pattern $[1\bar{1}\bar{2}]$, where the diffraction spots of twinned and untwinned parts of the precipitates overlap. All of the diffraction spots of <532> and <431> show extra spots due to twinning, e.g., see Fig. 17 and Fig. 21.

Figs. 20(a) and (b)* are similar diffraction patterns to Fig. 17(b). However, they not only show the (111) and (11$\bar{1}$) twin axes clearly but also show multiple twinning reflections. The twinning of $(\bar{1}11)T_1$ and $(1\bar{1}\bar{1})T_1$ form a new twin

axis, which is labelled T_3, and the indexes of the diffraction patterns for the multiple twinning is given in Fig. 20(c), using the T_1, T_2 and T_3 twin axes representation. There are other extra spots in the diffraction pattern due to double diffraction from twinning. Fig. 22 is a micrograph of the multiple twin structure.

4.3 Structure of the matrix in zirconium alloys

According to phase diagrams for the Zr-Cr and Zr-Fe binary systems, Fig. 1, the matrix in both Zircaloy-4 and Zr-Cr-Fe alloy is expected to be α-Zr. α-Zr has a hexagonal lattice with a=0.3232 nm and c=0.5147 nm. Since diffraction patterns of the matrix are generated together with the diffracion patterns for the $Zr(CrFe)_2$ precipitates they can be used to calculate the camera constant of the TEM and thus assist in indexing the diffraction patterns of the precipitates.

The precipitates of C14 hexagonal $Zr(CrFe)_2$ type can be as coherent particles since they have the same structure as the hexagonal α-Zr matrix. The precipitates of C15 cubic Laves phase however are only partially coherent. Elastic distortion of α-Zr matrix is observed because of the different lattice parameters and or structures of the precipitates and the matrix, and the different atom sizes of chromium and zirconium. As shown is shown in Figs. 9, 23 and 24 dislocations are produced in α-Zr matrix at or near the precipi-

tates due to the distortion of the matrix. Since many more precipitates are formed at the grain boundaries, dislocations are produced at, and emitted from these boundaries. For small $Zr(CrFe)_2$ Laves phase precipitates where there is a stress concentration, prismatic dislocation loops are nucleated, e.g. Fig. 24(b). Dislocations are also produced at the corners of the precipitates, e.g. Fig. 22, because of stress concentrations. The contrast halos which are found around some of the precipitates, e.g. Fig. 22, are considered to be due to elastic distortion of matrix.

Due to this distortion, satellites and extra diffraction spots appear for the matrix reflections. All of the diffraction patterns for the α-Zr showed the satellite spots, and the $[1\bar{1}\bar{2}]$, $[\bar{3}25]$, $[\bar{2}13]$ and [110] patterns showed the extra reflection as indicated in Figs. 17-18, 20-21. According to the lattice parameters of $Zr(CrFe)_2$ and α-Zr, the diffraction spots of the type (0002), (0004),..., should be inside the diffraction spots of the (220), (440),... But the opposite was found, e.g., Fig. 17,18. This also represents local elastic distortion of the matrix.

4.4 Orientation relationships between the $Zr(CrFe)_2$ precipitates and α-Zr matrix

The orientation relationships between the C15 $Zr(CrFe)_2$ Laves phase precipitates and the hexagonal α-Zr matrix are $(001)_L // (11\bar{2}0)_\alpha$, $[110]_L // [0001]_\alpha$ (the subscripts L and α rep-

resent the $Zr(CrFe)_2$ Laves phase and α-Zr, respectively) for Zircaloy-4 and $(111)_L // (1\bar{2}10)_\alpha$, $[110]_L // [0001]_\alpha$ for Zr-Cr-Fe alloy obtained by diffraction patterns, Fig. 11 and 17-21. A model representing the orientation relationship has been constructed and is given in Fig. 25. The model is the same as for the C15 type $Zr(CrFe)_2$ Laves phase formed in both Zircaloy-4 and Zr-Cr-Fe alloy. In the Zr-Cr-Fe alloy, a eutectoid of $Zr(CrFe)_2$ and α-Zr is formed from the cubic α-Zr, thus the model is considered to show the orientation relationship. However, in Zircaloy-4 due to the C15 $Zr(CrFe)_2$ Laves phase transform from α-Zr the model is considered to illustrate the transformation of the hexagonal α-Zr to the cubic $Zr(CrFe)_2$ Laves phase.

In the C15 Laves phase structure the eight zirconium atoms are arranged on a diamond cubic lattice with atoms located at positions,

000, 1/2 1/2 0, 1/2 0 1/2, 0 1/2 1/2

1/4 1/4 1/4,, 3/4 3/4 1/4, 3/4 1/4 3/4, 1/4 3/4 3/4.

The sixteen iron and chromium atoms, the M' atoms of the MM'_2 phase, are located a n/8 where n=1,3,5,7 [1], i.e., at position,

5/8 5/8 5/8, 5/8 7/8 7/8, 7/8 5/8 7/8, 7/8 7/8 5/8

5/8 1/8 1/8, 5/8 3/8 3/8, 7/8 1/8 3/8, 7/8 3/8 1/8

1/8 5/8 1/8, 1/8 7/8 3/8, 3/8 5/8 3/8, 3/8 7/8 1/8

1/8 1/8 5/8, 1/8 3/8 7/8, 3/8 1/8 7/8, 3/8 3/8 5/8.

The diffraction spots of reciprocal lattice planes for the iron and chromium atoms in the Laves phase, for example (1/8 1/8 5/8), should overlap with the diffraction spot of the (115) reciprocal plane which is formed from the Zr atoms. Thus it is difficult to identify the reflections due to chromium and iron, and therefore the model focusses on the position of the Zr atoms only. The possible positions for both M and M' atoms in the Laves phases is given in section 5.2 based on the diffraction intensities. In Fig. 25, U, V, W and H represent the zirconium atoms in the diamond cubic lattice of the Laves phase. H and some atoms of face center position are considered to be generated by movement of Zr atoms from close-packed hexagonal α-Zr matrix atoms, labelled M or G.

In this model, for Zircalcy-4, the pairs of planes (200) and (0002) , (660) and (2200) are parallel and have approximately the same interplanar spacings such that the reflections would almost overlap on the diffraction pattern, which was in fact found in the experimentally determined diffraction patterns. The displacement of zirconium atoms on going from α-Zr to the C15 Laves phase was calculated to be 0.007-0.052 nm for the eight corner atoms, 0-0.081 nm for the six face center atoms, and 0-0.093 nm for the other zirconium atoms on the diamond cubic structure. Because the small displacements that are required of the zirconium atoms, the transformaion from α-Zr to the C15 type

$Zr(CrFe)_2$ Laves phase can occur fairly easily. This would be particularly true for transformations at grain boundaries, (i.e., where in fact the precipitates did form) since there is a "loose" atomic arrangement.

For Zr-Cr-Fe alloy, two types of diffraction patterns, shown in Figs. 17(b) and 20, gave the same orientation relationship, both of them agree with the model. According to the stereogram, if the cubic (110) is parallel to hcp (0001), then the crystal plane (113) should be parallel to $(10\bar{1}0)$. This agrees with the diffraction pattern shown in Fig. 17(b), and the model.

Based on the model for both Zircaloy-4 and Zr-Cr-Fe alloy the orientation relationships between the $Zr(CrFe)_2$ precipitates and the α-Zr matrix are $(001)_L$ // $(11\bar{2}0)_\alpha$, $(\bar{1}1\bar{1})_L$ // $(\bar{2}110)_\alpha$, $[110]_L$//$[0001]_\alpha$.

According to the diffraction pattern in Fig. 13 the orientation relationship between the C14 hexagonal $Zr(CrFe)_2$ Laves phase precipitates and α-Zr matrix was close to $(11\bar{2}5)_L$ // $(0\bar{1}10)_\alpha$, $(11\bar{2}0)_L$ // $(01\bar{1}0)_\alpha$, $[1\bar{1}00]_L$//$[0001]_\alpha$.

4.5 Polytype structures in $ZrCr_2$ and $Zr(CrFe)_2$ Laves phases

Fig. 26(a) shows the general shape of the $ZrCr_2$ particles (powder). Many of the particles are hexagonal in shape. An electron diffraction pattern of hexagonal shape particle was taken down the [0001] zone axis. The particles themselves

contain a number of dislocations, Fig. 26(c), which appear to be distributed along the $(10\bar{1}0)$ type directions. The general angles included between two dislocations are 60°.

To identify the structures of stoichiometric $ZrCr_2$, $Zr(CrFe)_2$ and $ZrFe_2$ Laves phases the samples were tilted around both $g_{11\bar{2}0}$ and $g_{000\bar{1}}$ for $ZrCr_2$ and $g_{000\bar{1}}$ for $Zr(CrFe)_2$ and $ZeFe_2$. Systematic electron diffraction patterns were taken. Representative electron diffraction patterns are given in Figs. 27 and 28. The indexing of the diffraction patterns will be discussed in section 5.1. Based on this indexing, the $ZrCr_2$ and $Zr(CrFe)_2$ bulk stoichiometric cast alloys appear to have a hexagonal lattice, and the $ZrFe_2$ a cubic lattice.

Polytype structures have been found in the bulk $ZrCr_2$ stoichiometric alloy, and the $Zr(CrFe)_2$ Laves phase precipitates in Zircaloy-4 and Zr-Cr-Fe. For the close packed hexagonal (C14) structure 2H, 4H, 8H, 12H, 14H and 20H polytype structures have been found in the bulk stoichiometric $ZrCr_2$ alloy, the 2H, 6H and 10H polytype structures in the precipitates in Zircaloy-4. Using a rhombohedral lattice to represent the C15 type cubic structure of the $Zr(CrFe)_2$ Laves phase, 3R structures have been found in Zircaloy-4 and 3R twinned structures have been found in Zr-Cr-Fe . Stacking faults have also been found for the rhombohedral structure in both Zircaloy-4 and Zr-Cr-Fe. The diffraction patterns for the 2H, 3R, 3R twinned, 4H, 6H, 8H, 10H, 12H, 14H and 20H structures are given in Fig. 29.

By using lattice images the one dimensional stacking structures could be confirmed. Fig. 30 gives the lattice images for the 2H structure, and the 4H and 8H, 8H and 12H and 12H and 14H mixed structures. The lattice images also show that dislocations exist in the Laves phases. Figs. 32-34 are micrographs for the 3R and 3R twinned structures.

Using the microdensitometer, the intensities of the electron diffraction patterns were measured. A comparison of the calculated and measured relative intensities for the 8H, 12H, 14H and 3R twinned structures is given in Table 10 and 11. The data for the 3R and 8H structures were entered into SAS on the data cards. The SAS package plotted the relative intensity distributions along 01L and these are shown in Fig. 35.

Chapter V

DISCUSSION

5.1 Identification of the C15 and C14 $Zr(CrFe)_2$ Laves phase

5.1.1 Use of high order Laue zones

The electron diffraction pattern given in Fig. 9(b) is formed from the precipitate shown in Fig. 9(a). Based on the diffraction pattern the precipitates can be indexed using either body-centered cubic, face-centered cubic, or hexagonal close-packed lattices because the reflections for the $(310)^*$ reciprocal plane for the bcc lattice, $(112)^*$ for the fcc lattice and $(1\bar{1}00)^*$ for the hcp lattice give the same pattern. For identification of the structure of the precipitates and indexing the pattern, high order Laue zones can be used.

The SAD pattern is a composite of two sets of diffraction patterns; one from the matrix phase and one from the precipitates. The matrix phase is α-Zr with a $[2\bar{1}\bar{1}0]$ zone axis. The interplanar spacing for the (0002) crystal planes of α-Zr, $d_{0002}=0.2578$ nm, is then used as a standard to calculate the camera constant of the TEM and then to index the SAD of the precipitate. The SAD pattern of the precipitate is determined as the [112] zone axis of C15 structure.

Since the $Zr(CrFe)_2$ Laves phases can also have the C15 diamond cubic or C14 hexagonal lattice, then indexing as the (310)* reciprocal plane for bcc cubic lattice can be disregarded and only the indexing using a C15 cubic or C14 hexagonal structures need be considered. The electron diffraction pattern in Fig. 9(b) was indexed as either the C15 or the C14 structure and the results are shown in Figs. 9(d) and 9(e). Four sets of patterns were indexed for the two kinds of structures. The solid circles represent the zero order Laue reflection for both precipitate and matrix. For the C14 cubic $Zr(CrFe)_2$ Laves phase the large and small open circles represent +1 and -1 orders reflection respectively. For the C15 $Zr(CrFe)_2$ Laves phase precipitates the positive and negative first order Laue zones corresponding to $N=\pm 2$, and $N=\pm 1$ were extinct. The large and small open circles represent the N=-2 and +2 order reflections. Comparison of the electron diffraction pattern which was taken with TEM Fig. 9(b) and the calculated patterns, Fig. 9(d) and (e) indicate that the $Zr(CrFe)_2$ precipitates should be indexed using the C15 lattice.

Two methods were used to calculate and index the positions of the diffraction spots for high order Laue zones.

(a) According to diffraction geometry the projected position of diffraction spots for high order Laue zone at zero layer can be calculated from the following formulas:

$$h_1H+h_2K+h_nI=h$$

$$k_1H+k_2K+k_nL=k$$

$$l_1H+l_2K+l_nL=l$$

where hkl is reciprocal lattice in high order Laue zone; $h_1k_1l_1$, $h_2k_2l_2$ are reciprocal lattice spots in zero order Laue zone; H, K, L are the coordinates of diffraction spots hkl in zero order reciprocal lattice. Thus, H, K are coordinates of hkl in reciprocal lattice plane of zero order Laue zone; h_n k_n l_n is reciprocal lattice spot perpendicular to $h_1k_1l_1$ and $h_2k_2l_2$ [64]. The projected position of (111) for $(112)_2$ Laue zone are $H_{111}:g_{111}=1:3$, $K_{111}:g_{220}=1:2$. The projected position of (020) for $(112)_2$ are $H_{020}:g_{111}=2:3$, $K_{020}:g_{220}=1:2$ in fcc $(112)_0$ reciprocal plane. In the hcp lattice the projected position of $(1100)_1$ higher layer Laue zone at zero order $(1100)_0$ reciprocal lattice plane are $H_{100}:g_{002}=0:1$, $K_{100}:g_{110}=1:2$, as shown in Fig. 9(d,e).

(b) The second method used to index the diffraction pattern included non-zero order Laue reflection, for example the index of hcp $(1100)_1$, is given as follows [63].

According to crystal zone law

$$hu+kv+lw = N \qquad (9)$$

where (uvw) is reciprocal lattice plane of parallel set or crystal (hkl) is any point lying in the reciprocal lattice plane, N is always an integer. For the [1100] crystal zone axis of hexagonal lattice uvw = 110, if N=1 hkl can be (101). In order to obtained the position of reciprocal lattice point in the N plane projected into zero Laue zone, according to projective geometry, an additional vector

$$c = N/(u^2+v^2+w^2) \qquad (10)$$

has to be used. When c=0.5, the position of [101] was obtained by h-cu, k-cv, l-cw. Therefore the coordinate of the position of the high order Laue diffraction spot in the zero Laue plane is (0.5, 0.5). The spot pattern in high order Laue zone is the same arrangement as that in the zero Laue zone since the two patterns are parallel. Thus the diffraction of the high order Laue zone can be indexed immediately after indexing one spot which lies in the high order Laue zone. The experimentally determined pattern for [112], Fig. 9(b) which includs the diffraction spots of the higher order Laue zone, is the same as that given in Fig. 9(d). In this diffraction pattern is the evidence from which the precipitate is determined to be the cubic C15 type $Zr(CrFe)_2$ phase and not the hexagonal structure.

5.1.2 Indexing of diffraction patterns for bulk stoichiometric alloys

Although a diffraction pattern comprising the zero and non-zero order Laue zones can be used to index the structure of the crystal correctly, a diffraction pattern which includes bright high order Laue diffraction spots is difficult to obtain unless the specimen is thin enough or the crystal has a large lattice parameter. For the precise identification of the $Zr(CrFe)_2$ Laves phase, the specimen is tilted around basic reciprocal vectors. Thus systematic electron diffraction patterns and interplanar angles could

be obtained, as given in Fig. 11 and Table 9 for the $Zr(CrFe)_2$ Laves phase precipitates in Zircaloy-4, and in Fig. 17 for the Zr-Cr-Fe alloy.

To identify the structure of bulk stoichiometric $Zr(CrFe)_2$ alloys the samples of $Zr(Cr_xFe_{1-x})_2$ alloys, where x=1, 0.75, 0.55, 0.2 and 0, were tilted around $\vec{g}_{100}$ and $\vec{g}_{001}$. Systematic electron diffraction patterns for $ZrCr_2$ tilted around (100)* were taken for [001], $[11\bar{4}]$, $[11\bar{3}]$, $[11\bar{2}]$, $[22\bar{3}]$ $[22\bar{1}]$, [114], [113], [112], [223], and [332] zone axes using the double tilt holder. Six of the diffraction patterns are shown in Fig. 27. The double tilt holder gives the tilting angles at both x and y directions. Using formula (2), in section 3.4, the effective tilting angles can be obtained. The projection of the reciprocal lattice down [110]* was constructed using the systematic $\vec{g}$ and the tilt angles, and is shown in Fig. 36. The figure shows that the c axis of the crystal is perpendicular to [100]. Using the information contained in the diffraction patterns in Figs. 27(a,g) and 36, $ZrCr_2$ is deduced to have the C14 hexagonal structure.

To index the structure of stoichiometric $ZrFe_2$ alloys the sample was tilted around (001)*. According to systematic electron diffraction patterns and their interplanar angles, the $ZrFe_2$ alloy has C15-type cubic structure. Using the cubic lattice to represented the diffraction pattern, 28(a), the (001)* should be the $(11\bar{1})$* reciprocal lattice plane.

Fig. 28 gives [$1\bar{1}0$], [$4\bar{3}1$], [$3\bar{1}2$], [$2\bar{1}1$] and [$3\bar{2}1$] diffraction patterns of $ZrFe_2$ with the cubic structure.

5.2 Structure determination of polytypes

The f.c.c. and h.c.p. structure are assembled from the close-packed atomic layers which have the same triangular net. The sequence of the atomic layers is ABC for the fcc lattice and AB for h.c.p. lattice. According to the distribution of the large atoms M the Laves phases are cubic or hexagonal. The structure of the Laves phase when discussed as the distribution of both M and M' atoms is composed of two kinds of sheets; one is a denser layer forming a net of triangles and hexagons, the O layers are shown in Fig. 37. The other is found between these denser layers and consists of three triangular nets of M or M' atoms stacked together in a close-packed manner [27,70,71]. If the shortest distance from the denser layer to a second layer of the same type is taken as a unit, then distance from a denser layer to each triangular net can be expressed as fractions of the distance between two denser layers. There are two kinds of stacking possible, called the A and A' layers respectively, by M and M' atoms of the Laves phase. If the A layers are shifted 1/3 or 2/3 in the [110] direction of the hexagonal cell, i.e. along the ca direction in Fig. 37, the B and C layers are obtained respectively, and A' stands in the same relationship to B' and C'. The structure of the different

polytypes of the Laves phases are formed with different stacking sequences of these layers.

The structure factors of the HKL reflections for these layer types, F(hkl), can be calculated from the atomic scattering amplitudes of the M and M' atoms and the phase shift due to each layer and is given by

$$F(hkl) = \sum_{m=0}^{n-1} V_m \exp(imp) \qquad (11)$$

where V_m represents the layer form factor of the m-th layer, and ψ the phase shift due to one layer. If the structure has n layers in a unit cell then

$$\psi = 2\pi\ell/n \qquad (12)$$

Referring to Fig. 37 the layer form factor of A, A', B, B', C and C' are given by

$$V_A = 2f_a \cos(3\psi/8) + f_b \left((-1)^h + (-1)^k + (-1)^{h-k}\right) + f_b\varepsilon \exp(i\psi/2) \qquad (13)$$

$$V_{A'} = 2f_a \cos(3\psi/8) + f_b \left((-1)^h + (-1)^k + (-1)^{h-k}\right) + f_b\varepsilon^* \exp(i\psi/2) \qquad (14)$$

where f_a is the atomic scattering amplitude for electrons for M atoms and f_b for M' atoms, and

$$\varepsilon = \exp(2\pi i(h-k)/3) \qquad (15)$$

Since if A (or A') layer is shifted 1/3 the arrangement will be B (or B') layer, therefore

$$V_B = V_A\varepsilon^*, \quad V_C = V_A\varepsilon \quad \text{and} \quad V_{B'} = V_{A'}\varepsilon^*, \quad V_{C'} = V_{A'}\varepsilon \qquad (16)$$

The diffraction intensity is in proportion to square of the structure factor. Since any one layer can be put over the other in two different ways, the possible number of arranged ways is 2^{n-1}, where n is the layer number of the polytype structure.

Using the computer and inputting different stacking sequences of A, B, C, A', B' and C', the relative intensities of diffraction can be obtained. Comparing the diffraction intensities as measured with these calculated, the various polytype structures can be identifed. A summary of the various polytype structures observed in the zirconium alloys in the present study is given in Table 12. Based on the comparison of the calculated and observed relative intensities, as given in Table 10 and 11, good agreement was obtained between the calculated and observed intensities for the 9H structure. Although the agreement was not so good for the 12H and 14H structures, this was considered to be due to the dense pattern of diffraction spots which gave rise to some degree of overlapping such that the intensities of neighbouring diffraction spots gave high background intensities for the measured diffraction spot. Double diffraction of electrons can also play an important role in altering the observed relative diffraction intensities.

In Zr-Cr-Fe alloy the 3R twinned structure was found. This 3R twinned structure can be considered to be composed of ABC and A'C'B' respectively. In Figure 37 it is demon-

strated that the stacking A'C'B' is equivalent to the twinning of ABC, where the twinning axis is along the bc direction. The relative intensities of the 3R twinned structure also show good agreement between calculated and observed values. The possible structures for the 6H, 8H, 12H and 14H Laves phases are given in Figure 38 (a-d).

5.3 Images of polytypies and defect structures

Fig. 30 gives the lattice images for the different stacking structures. The 2H structure lattice images in Figure 30(a) correspond with the diffraction pattern in Figure 29(a). As indicated in Table 12 the stacking sequence for 2H structure is AB. The structure of A or B layers are given in Figure 37. One period of the fringe is 0.82 nm. This is are period of AB stacking. The 2H structures for both $ZrCr_2$ and $Zr(CrFe)_2$ Laves phases alloys show only one type of fringe image. Stacking faults have not been found in 2H structures.

The diffraction patterns in Figures 29(g-l) show 8H, 12H, 14H and 20H stacking structures. The lattice images are given in Figures 30(b,c,e). In Figure 30(b) the 4H and 8H structures are labelled. The long period areas show 40 layer stacking which is an integral times the 4H and 8H structures. The lattice images of 8H and 12H structures, 12H and 14H structures are shown in Figures 30 (c,e). The long period structures are produced which are an integral number times the 4H, 8H, 12H or 14H structures. The period of con-

trast variation in all of the lattice fringe images shows the same behaviour as indicated in the diffraction patterns.

The formation of polytype structures in $ZrCr_2$ Laves phases is considered to be based on the 4H structure. Comparing the diffraction patterns for the 8H, 12H, 20H structures it can be seen that there are four stronger diffraction spots in (100) to (108), (100) to (10.12) or (100) to (10.20). As mentioned previously the 4H stacking is a mixed structure of the 2H and 3R polytypes.

The images of 3R and 3R twinned structures are given in Figure 32-34. The precipitate of $Zr(CrFe)_2$ Laves phase in Zircaloy-4 appears to be formed by the stacking of (111) crystal planes. Between the sheets of (111) crystal planes, parallel or twist subboundaries appear. It is considered that these are an array of parallel edge dislocations or a mix of more then one direction edge dislocations. Figure 34 gives a partial lattice fringe image of partial (111) twinned planes in an orientation giving a sharp projected fringe image of the (111) planes in the Zr-Cr-Fe alloy.

Dislocations were also found in 3R twinned and $ZrCr_2$ stoichiometric bulk Laves phase alloys, and examples are shown in Figures 24(b) and 26(b), 31(a) and 34.

5.4 Factors effecting the formation of polytypism in zirconium alloys

Five different kinds of bulk stoichiometric Zr-Cr-Fe cast alloys were studed with TEM. According to the electron diffraction patterns, the $ZrFe_2$ alloy showed only the 3R cubic structure, whereas all of the $ZrCr_2$ and $Zr(CrFe)_2$ bulk stoichiometric alloys had hexagonal structures. These are in agreement with the work [10]. Elliott has shown that the $ZrCr_2$ has $MgZn_2$ type hexagonal structure when electron:atom ratio is 1.8-2.3; the $ZrFe_2$ has $MgCu_2$ type cubic structure and electron:atom ratio is 1.5-1.8. In present study only $ZrCr_2$ exhibited the polytypism phenomenon, having the 2H, 4H, 8H, 12H, 14H and 20H structures. All of the $Zr(CrFe)_2$ cast alloys showed the 2H structure only. Therefore the composition of the alloys is an important factor affecting the polytypism.

However in Zircaloy-4 and the Zr-Cr-Fe alloy, the main structure of the $Zr(CrFe)_2$ -type Laves phase precipitaties was the 3R rhombohedral structure, i.e. the cubic structure. A twinned structure was found in the Zr-Cr-Fe alloy which had been heat treated at 1050 °C for 30 min, water quenched, and then anneaded at 760 °C for 10.5 hours. In the Zircaloy-4 some $Zr(CrFe)_2$-type Laves precipitates have the simple 3R cubic structure, whereas other polytypes had the 6H or a higher period structure. Therefore the conditions during formation of the $Zr(CrFe)_2$ Laves phase precipitates e.g. heat treatment also affects the polytypism.

As mentioned in section 2.2.3 several different explanations for formation of polytypism have been advanced. From the present work the hexagonal-type polytype structures of the Laves phases in zirconium alloys show one dimensional periodic stacking faults. For the cubic-type structure the stacking faults or twinned structures formed in both (111)* and (111)* orientations. The formation of the different polytypes is effected both by the composition of the alloys and the heat treatment schedules to which they had been exposed.

Chapter VI

CONCLUSIONS

Electron diffraction, high resolution electron microscopy and energy dispersive X-ray analysis have been used to identify $Zr(CrFe)_2$ Laves phases in Zircaloy-4 and Zr-1.15 wt%Cr-0.1 wt%Fe alloys. Polytypic structures have been shown to exist in the Laves phases in zirconium alloys. The main features of the structures of these Laves phases are as follows:

1. According to energy dispersive X-ray spectra the alloying elements zirconium, iron and chromium are mainly concentrated in the $Zr(CrFe)_2$ Laves phase precipitates in both Zircaloy-4 and Zr-1.15 wt%Cr-0.1 wt%Fe. The precipitates exist both within grains and at grain boundaries.

2. Two kinds of $Zr(CrFe)_2$-type Laves phase precipitates have been found in Zircaloy-4 alloys: a cubic Laves phase with 3R structure and a hexagonal Laves phase precipitate with 2H, 6H and 10H polytype structures. Longer period H-type stacking structures were also found.

3. 3R type $Zr(CrFe)_2$ Laves phase precipitates were found in the Zr-1.15wt%Cr-0.1wt%Fe alloy. Also found was a 3R twinned and multiple twinned structure, with the two parts of the twin being formed by ABC and A'C'B' stacking respectively.

4. The orientation relationship between the $Zr(CrFe)_2$ Laves phase and the α-Zr matrix is $(001)_L$ //$(11\bar{2}0)_\alpha$, $[110]_L$ //$[0001]_\alpha$. Using data from the electron diffraction patterns, a model of orientation relationship between $Zr(CrFe)_2$ Laves phase and α-Zr is developed for Zircalcy-4 and the Zr-Cr-Fe alloy. For Zircaloy-4 the model represents the transformation from α-Zr to $Zr(CrFe)_2$.

5. In a cast bulk stoichiometric $ZrFe_2$ alloy the 3R type cubic structure is the only polytype found. However bulk $Zr(Cr_xFe_{1-x})_2$ alloys, where x=1, 0.75, 0.55 and 0.20, have the 2H type hexagonal structures.

6. The 2H, 4H, 8H, 12H, 14H and 20H polytypism structures have been found in the cast bulk $ZrCr_2$ stoichiometric Laves phase alloy. All of the polytype structures are based on the 4H structure.

7. The chemical composition and heat treatment schedules are considered to be important factors affecting the formation of the different polytype structures.

BIBLIOGRAPHY

1. Metals Handbook, Vol. 8, Metallography, Structure and Phase Diagrams, 8th ed., American Society for Metals, Metals park, Ohio, (1973) p.239.

2. D.O. Northwood and L.E. Bahen, Atomic Energy of Canada Limited Report AECL-5019, August (1975).

3. D.O. Northwood and K. Dosen, The Metallurgical Society of AIME, TMS Paper Selection F80-9, (1980) p.9.

4. C.E. Coleman, Unpublished paper quoted in ref. of D.O. Northwood and R.W. Gilbert, J. Aust. Inst. Met. 18 (1973) 158.

5. H. Baumhauer, Z. Krist. 50 (1912) 33.

6. C.S. Barrett, T.B. Massalski, Structure of Metals, Third Revised Edition, Pergamon, Oxford, (1980) 256.

7. B.L. Berry and G.V. Raynor, Acta Cryst., 6 (1953) 178.

8. G.V. Raynor, Progress in Metal Physics, 1 (1949) 32.

9. F. Laves and H. Witte, Ibid 15 (1936) 840.

10. R.P. Elliott and W. Rostoker, Transactions of the ASM, 50 (1958) 617.

11. A.R. Edwards, Metallur. Trans. 3 (1972) 1365.

12. E.T. Hoyes, A.H. Roberson, and M.H. Davies, J. Met., March (1952) 304.

13. E.P. Domagala, D.J. Mcpherson and M. Hansen, Mat., Feb. (1953) 279.

14. D. Shaltiel, J. Less-Common Metals, 62 (1978) 407.

15. D.G. Ivey, Hydrogen Storage Characteristics of Zr$(Fe_xCr_{1-x})_2$ Ph.D thesis, University of Windsor, 1985.

16. W.L. Bragg, Phil. Mag. 39 (1920) 647.

17. R.M. Bozorth, J. Amer. Chem. Soc. 44 (1922) 2232.

18. J.M. Bijvoet and W. Nieuwenkamp, Z. Krist., 86 (1933) 466.

19. P.S. Mitchell, Z. Krist., 111 (1959) 372.

20. M. Ross, E. Takeda and D.R. Wones, Science (Washington), 151 (1966) 191.

21. H.Sato, R.S. Toth and G. Honjo, J. Phys. Chem. Solids, 28 (1967) 137.

22. B.E. Brown and D.J. Beerntsen, Acta Cryst., 18 (1965) 31.

23. Y. Komura, S. Takeda and Y. Kitano, Sci. Rep. Hitu A29, Suppl. 1 (1981) 13.

24. C.B. Carter, Phil. Mag. A, 50, 1 (1984) 133.

25. A.R. Verma and P. Krishna, Polymorphism and Polytypism in Crystals, Wiley, New York, (1966) p.61.

26. G.C. Trigunayat and G.K. Chadha, Phys. Stat. Sol., (a) 4 (1971) 9.

27. Y. Komura, Acta Cryst., 15 (1962) 770.

28. Y. Komura, A.Nakaue and M. Mitarai, Acta Cryst., B28 (1972) 727.

29. Y. Komura and Y. Kitaro, Acta Cryst. B33 (1977) 2496.

30. Y. Kitano, Y. Komura and H. Kajiwara, Japan Inst. Met., 18 (1977) 39.

31. Y. Kitano, Y. Komura and H. Kajiwara, Acta Cryst. A36 (1980) 16.

32. Y. Komura, K. Tokunaga, Acta Cryst., B36 (1980) 1548.

33. L.S. Ramsdell, Am. Mineralogist 32 (1947) 64.

34. G.S. Zhdanov, Compt. Rend. Acad. Sci. URSS 48 (1945) 43.

35. A.R. Verma, Phil. Mag., 42 (1951) 1005.

36. F.C. Frank, Phil. Mag., 42 (1951) 1014.

37. B. Jagodzinski, Neues Jahrb. Mineral., 3 (1954) 49.

38. B. Jagodzinski, Acta Cryst., 2 (1949) 298.

39. C.J. Schneer, Acta Cryst., 9 (1955) 279.

40. H. Peibst, Z. Phys. Chem., 223 (1963) 193.

41. A.R. Verma, Nature 167 (1951) 939.

42. S. Amelincks, J. Chim. Phys. 48 (1951) 475.

43. S. Amelincks, Nature, 168 (1951) 431.

44. A.J. Forty, Phil. Mag., 42 (1951) 670.

45. S. Amelinckx, Compt. Rend., 234 (1952) 971.

46. S. Amelinckx and W. Dekeyser, Compt. Rend. 19 , Algiers 1952, 18 (1953) 9.

47. E. Vitikainen and P. Nenonen, J. Nucl. Mater., 78 (1978) 362.

48. R. Kuwae, K. Sato, E. Higashinakagawa, J. Kawashima and S. Nakamura, J. Nucl. Mater., 119 (1983) 229.

49. P. Chemelle, D.B. Knorr, J.B. Van Der Sande and R.M. Fellcux, J. Nucl. Mater., 113 (1983) 58.

50. T. Kubo, Y. Wakashima, H. Imahashi and E. Nagai, J. Nucl. Mater., 132 (1985) 126.

51. R.A. Versaci and M. Ipohorski, J. Nucl. Mater., 116 (1983) 321.

52. V. Krasevec, J. Nucl. Mater., 98 (1981) 235.

53. X. Meng and D.O. Northwood, J. Nucl. Mater., 126 (1984) 317.

54. W.J.S. Yang, R.P. Tucker, E. Cheng and R.B. Adamson, Precipitates in Zircaloy: Identification and the effects of irradiation and thermal treatment, Nuclear Energy Business Operation. General Electric Company, Nov. (1985).

55. I.M. Grange, D. Charquet and L. Moulin, New Intermetallic Compouds in Zircaloy-4, in: Zirconium in the Nuclear Industry, Fifth Conference, ASTM STP 754, D.G. Franklin, Ed., American Society for Testing and Materials, (1982) p. 96.

56. B.Vander Sande and A.L. Bement, J. Nucl. Mater., 52 (1974) 115.

57. M. Griffiths, R.W. Gilbert and B.A. Cheadle, Formation, Growth and Decomposition of precipitates in Zircaloy-2 and 4, Chalk River Nuclear Laboratories, AECL-5019, Sep. (1985).

58. N.V. Bangaru, J. Nucl. Mater., 131 (1985) 280.

59. K.Y. Huang, J. Nucl. Mater., 136 (1985) 16.

60. X. Meng and D.O. Northwood, Precipitates in High Phosphorus Zircaloy-4, To be presented at 13th Annual Meeting of Microscopical Society of Canada, Hamilton, June 13-15, (1986).

61. P. Mukhopadhyay, V. Raman, S. Banerjee and R. Krishnan, J. Mater. Scien., 14 (1979) 1398.

62. J.W. Edington, 1, Micrograph One, The Operation and Calibration of the Electron Microscope, in: Practical Electron Microscopy in Materials Science, J.W. Edington, Macmillan, Philips Technical Library, (1974) p. 34.

63. P.B. Hirsch, A. Howie, R.B. Nicholson, D.W. Pashley, M.J. Whelan, Electron Microscopy of Thin Crystals, Butterworths, London, (1965) p. 2.

64. K.H. Kuo, Y.H. Qiarg and W.Y. Kun, Application of Electron Diffraction Patterns in Crystallography, Science Publishing House, Beijing, (1983) p. 489.

65. J.A. Gard, Interpreation of Electron Diffraction Patterns, in Electron Microscopy in Mineralogy, H.-R. Wenk, P.E. Champness, J.M. Cowley, A.H. Heuer, G. Thomas, N.J. Tighe, Springer-Verlag, Berlin, (1976) p. 52.

66. G.A. Gard, Interpretation of electron micrographs and diffraction patterns. In: The Electron Optical Investigation of Clays, J.A. Gard ed, Mineralogical Society, London, (1971) p. 45.

67. J.C.H. Spence, Experimental High-Resoluion Electron Microscopy, Clarendon Press, Oxford, (1981) p. 121.

68. J.I. Goldstein, D.E. Nuwbury, P. Echlin, D.C. Joy, C. Fiori, E. Lifshin, Scanning Electron Microscopy and X-ray Microanalysis, Plenum Press, New York, (1981) p. 275.

69. N.C. Barbi, Electron Probe Microanalysis Using Energy Dispersive X-Ray Spectroscopy, Princeton, New Jersey, P. 32

70. F.C. Frank and J.S. Kasper, Acta Cryst., 11 (1958) 184.

71. F.C. Frank and J.S. Kasper, Acta Cryst., 12 (1959) 483.

VITA AUCTORIS

The author was born in Liaoning, China, on April 15, 1940.

EDUCATION: Secondary School Diploma, Level A, obtained at Attached Middle school of Beijing Normal University, Beijing, China, 1958.

B.A.Sc. in Material Science obtained at Beijing University of Iron and Steel Technology, Beijing, China, 1963.

SOCIETIES: China Society for Metals.

China Society for Electron Microscopy.

Member of Council of Beijing Society for Electron Microscopy.

PUBLICATIONS

1. Zirconium phosphide precipitates in Zircaloy-4, Meng Xian Ying (Xianying Meng) and Derek C. Northwood, J. Nucl. Mater. 126 (1984) 317-320.

2. A TEM study of long-period stacking in a $ZrCr_2$ Laves phase, Xian Ying Meng and D.O. Northwood, Metallography 18(1985) 183-192.

3. Intermetallic precipitates in Zircaloy-4, Xian Ying Meng and D.C. Northwood, J. Nucl. Mater. 132(1985) 80-87.

4. A TEM study of the C15 type $Zr(CrFe)_2$ Laves phase in Zircaloy-4, Xian Ying Meng and D.O. Northwood, J. Nucl. Mater. 136(1985) 83-90.

5. A study of the structure of $Zr(CrFe)_2$ Laves phase precipitates in a Zr-Cr-Fe alloy, Xian Ying Meng and D.O. Northwood, J. Nucl. Mater. 137(1986), 217-226.

6. Microstructures developed during steady-state creep of Al-Mg alloys, Xian Ying Meng and D.O. Northwood, Accepted by Metallography, (1986).

7. Polytype structure in Zr-Cr-Fe Laves phase, Xianying Meng and Derek C. Northwood, Accepted by J. Less-Common Metals (1986).

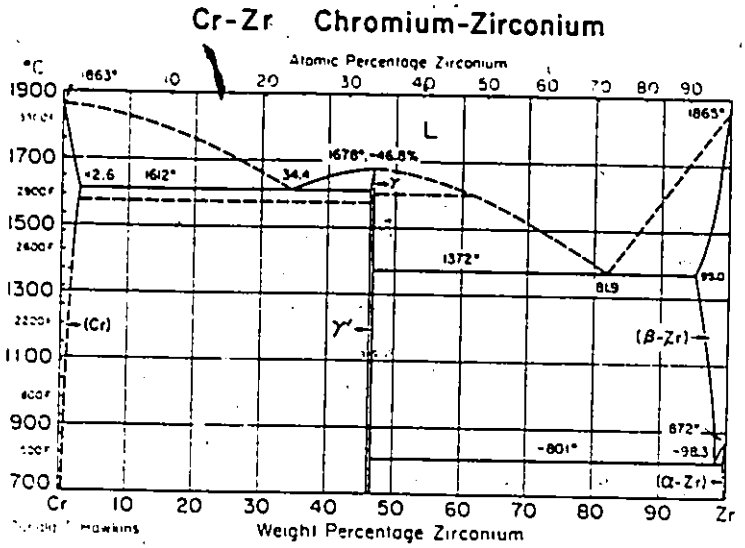

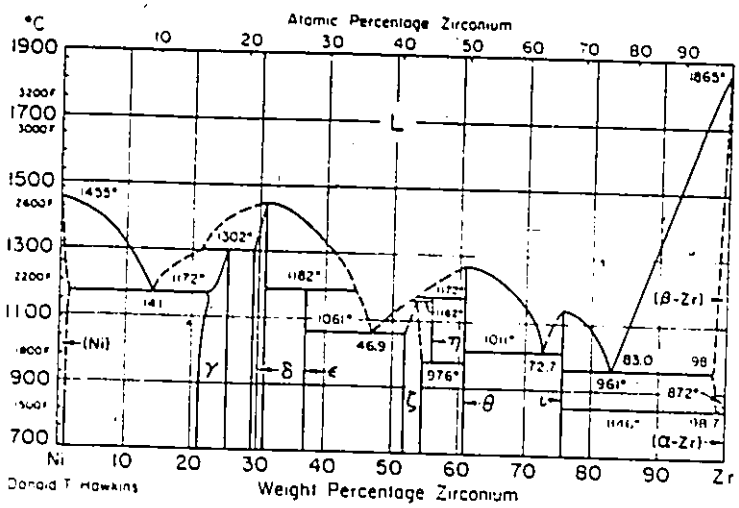

Figure 1: Phase diagrams for the Zr-Cr, Zr-Ni, Zr-Fe and Zr-Sn binary systems.

Fe-Zr Iron-Zirconium

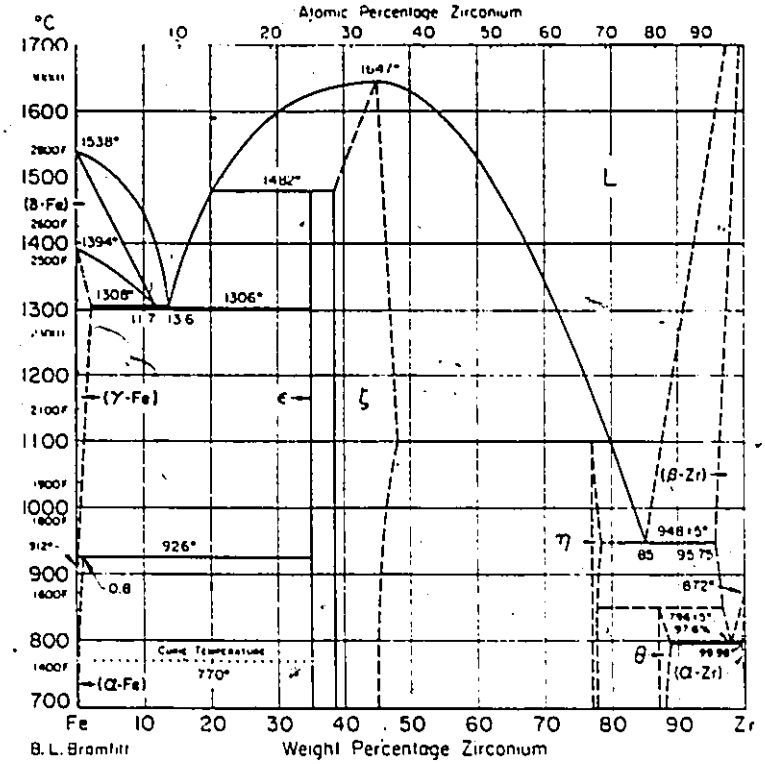

Sn-Zr Tin-Zirconium

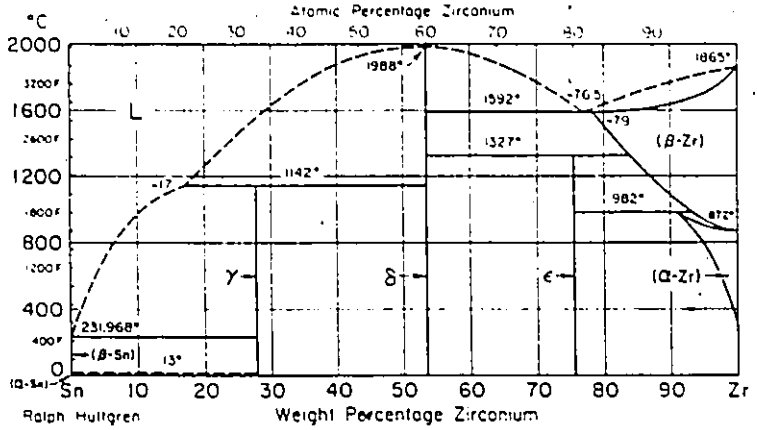

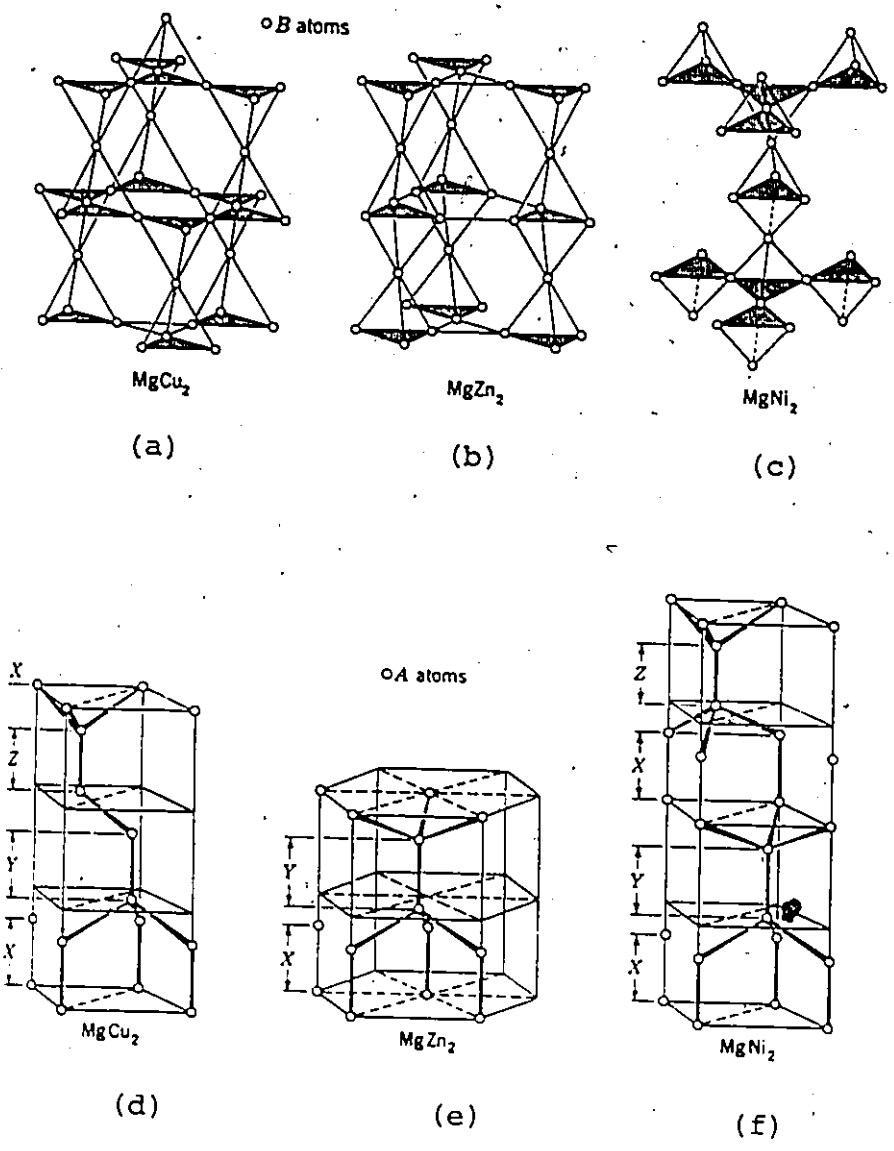

Figure 2: Distribution of M and M' atoms in Laves phases. (a-c) Distribution of M' atoms and stacking of tetrahedra in Laves phases. (d-f) Distribution of M atoms and stacking of double layer in Laves phases.

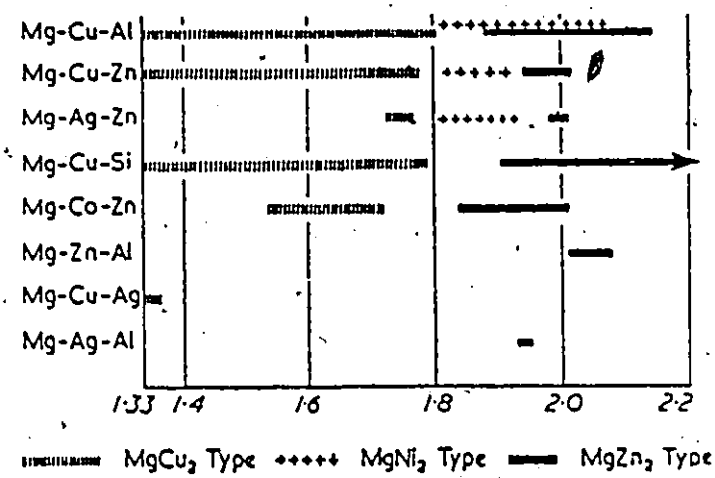

Figure 3: The dependence of the structure of Laves phases upon the electron/atom ratio. Schematic diagram showing the dependence of the range of existence of the $MgCu_2$, $MgNi_2$, and $MgZn_2$ structures upon the electron/atom ratio for several ternary magnesium alloys

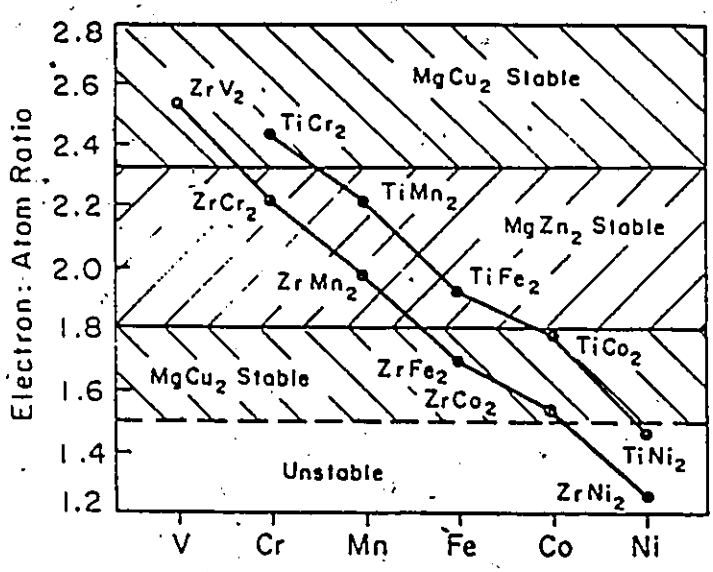

Figure 4: Stability ranges of binary Laves phases.

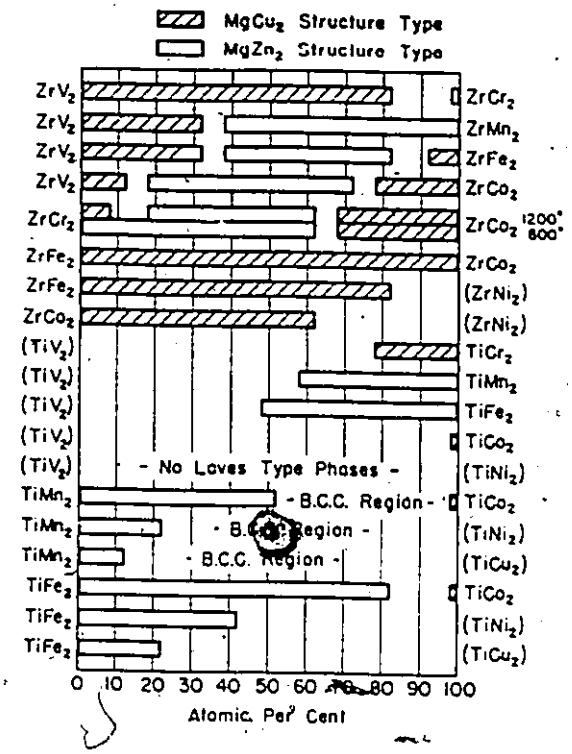

Figure 5: Miscibility ranges of Laves phases in quasi-binary sections.

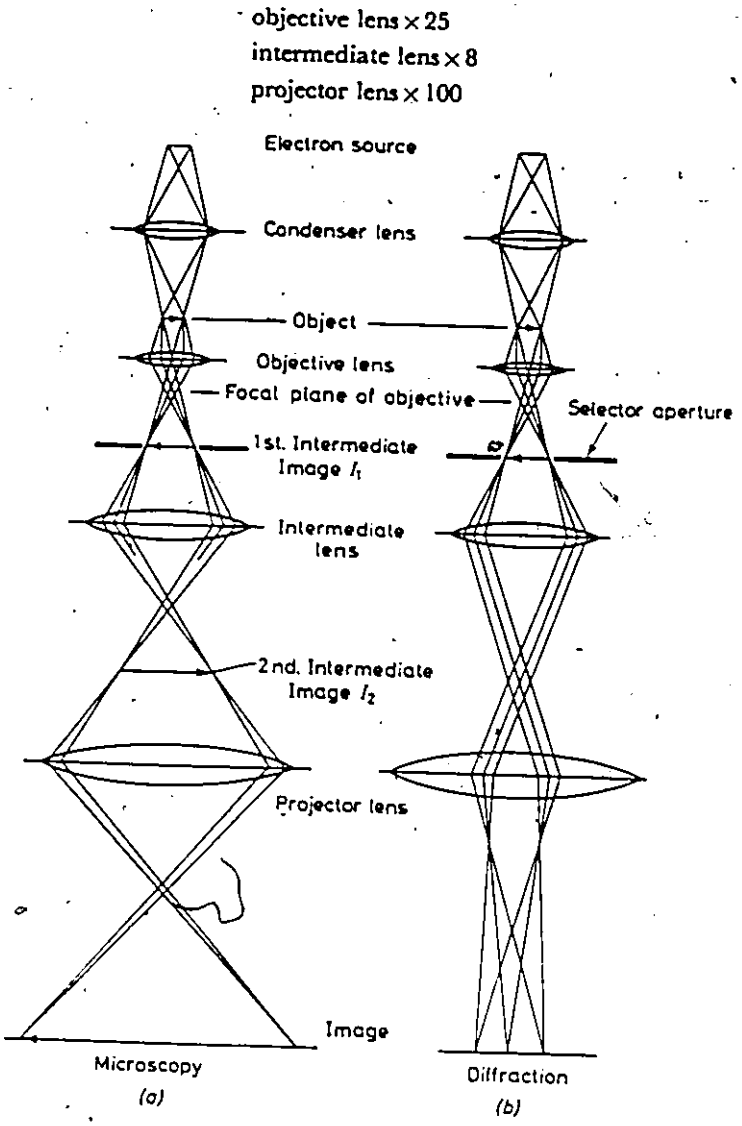

Figure 6. Ray paths in the electron microscope. For (a) imaging conditions and (b) diffraction conditions.

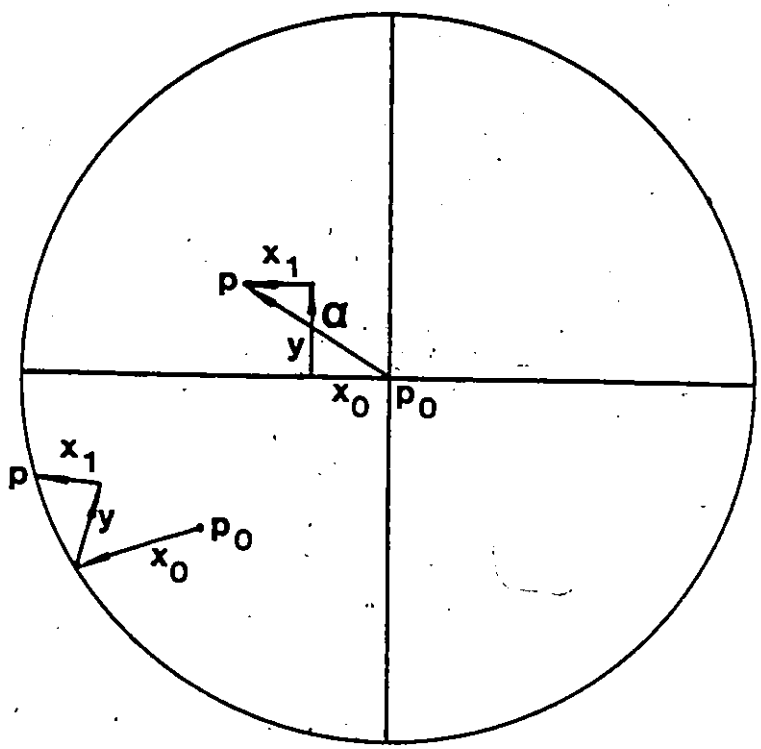

Figure 7: Operation of microscope for different imaging conditions. (a) Objective apertures are used to stop off the diffraction beams to form a bright field image. (b) Center dark field images are obtained by gun-tilting or beam deflection. (c) Dark field images are obtained with an off-axis aperture.

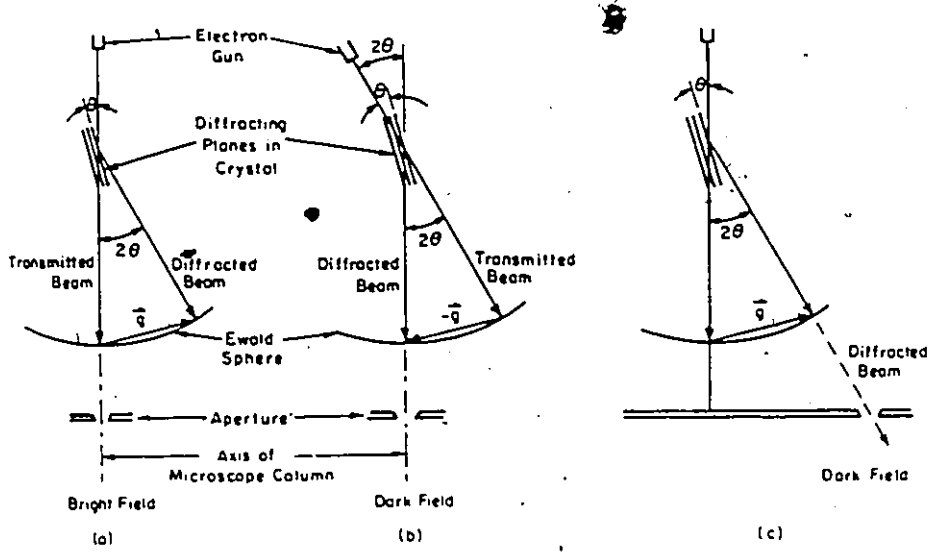

Figure 8: The tilt operation of double tilt holder illustrated with respect to a stereogram.

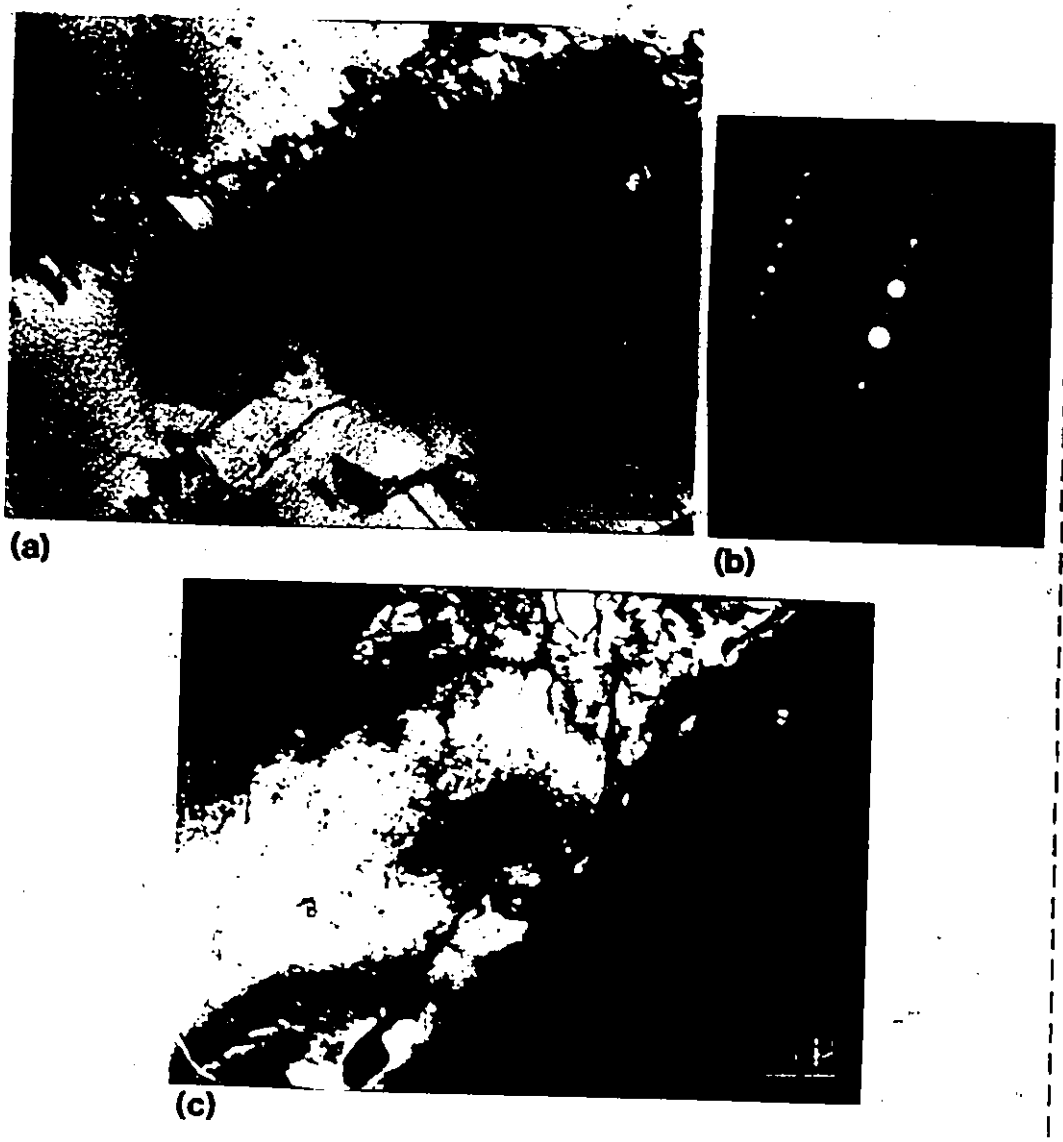

Figure 9: Cubic $Zr(CrFe)_2$ precipitates as found in Zircaloy-4. (a) A morphology; (b) the electron diffraction patterns of the $Zr(CrFe)_2$ Laves phase and the α-Zr matrix; (c) a morphology; (d) the key to the indexing of (b) based on a cubic structure; (e) diffraction pattern that would have been produced if the precipitates had the hexagonal structure.

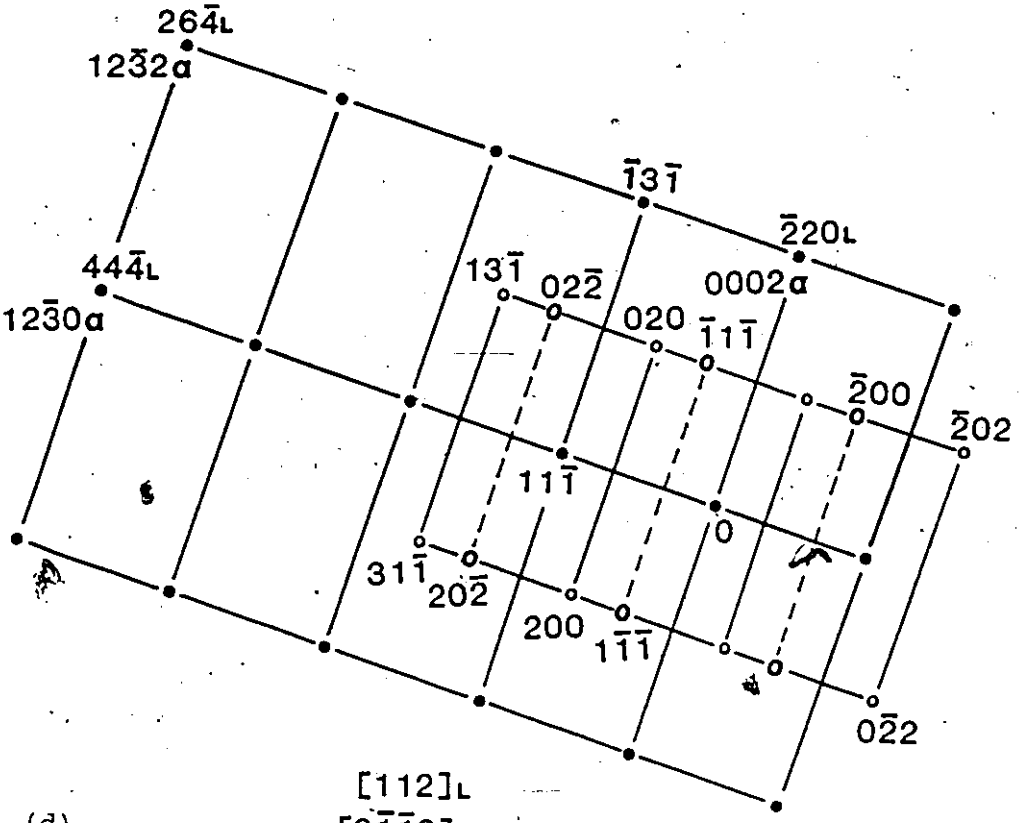
$26\bar{4}_L$
$12\bar{3}2_\alpha$
$\bar{1}3\bar{1}$
$\bar{2}20_L$
$44\bar{4}_L$
$12\bar{3}0_\alpha$
$13\bar{1}$
$02\bar{2}$
020
$\bar{1}1\bar{1}$
0002_α
$\bar{2}00$
$\bar{2}02$
$11\bar{1}$
0
$31\bar{1}$
$20\bar{2}$
200
$1\bar{1}\bar{1}$
$0\bar{2}2$
$[112]_L$
$[2\bar{1}\bar{1}0]_\alpha$

(d)

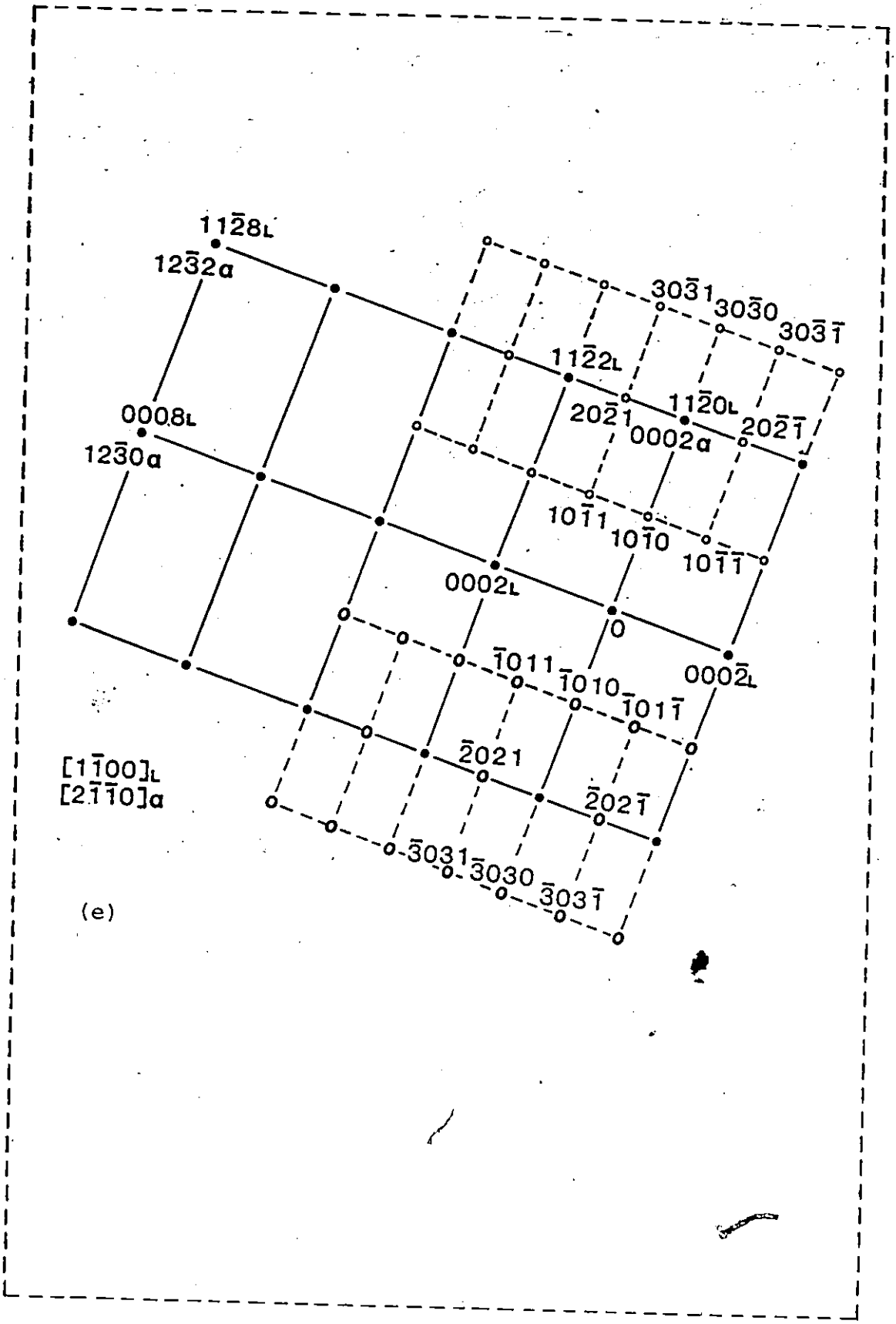
$11\bar{2}8_L$
$12\bar{3}2_a$
$30\bar{3}1$
$30\bar{3}0$
$30\bar{3}\bar{1}$
$11\bar{2}2_L$
$11\bar{2}0_L$
$20\bar{2}1$
0008_L
0002_a
$20\bar{2}\bar{1}$
$12\bar{3}0_a$
$10\bar{1}1$
$10\bar{1}0$
$10\bar{1}\bar{1}$
0002_L
0
$\bar{1}011$
$\bar{1}010$
$000\bar{2}_L$
$\bar{1}01\bar{1}$
$\bar{2}021$
$\bar{2}02\bar{1}$
$[1\bar{1}00]_L$
$[2\bar{1}\bar{1}0]_a$
$\bar{3}031$
$\bar{3}030$
$\bar{3}03\bar{1}$
(e)

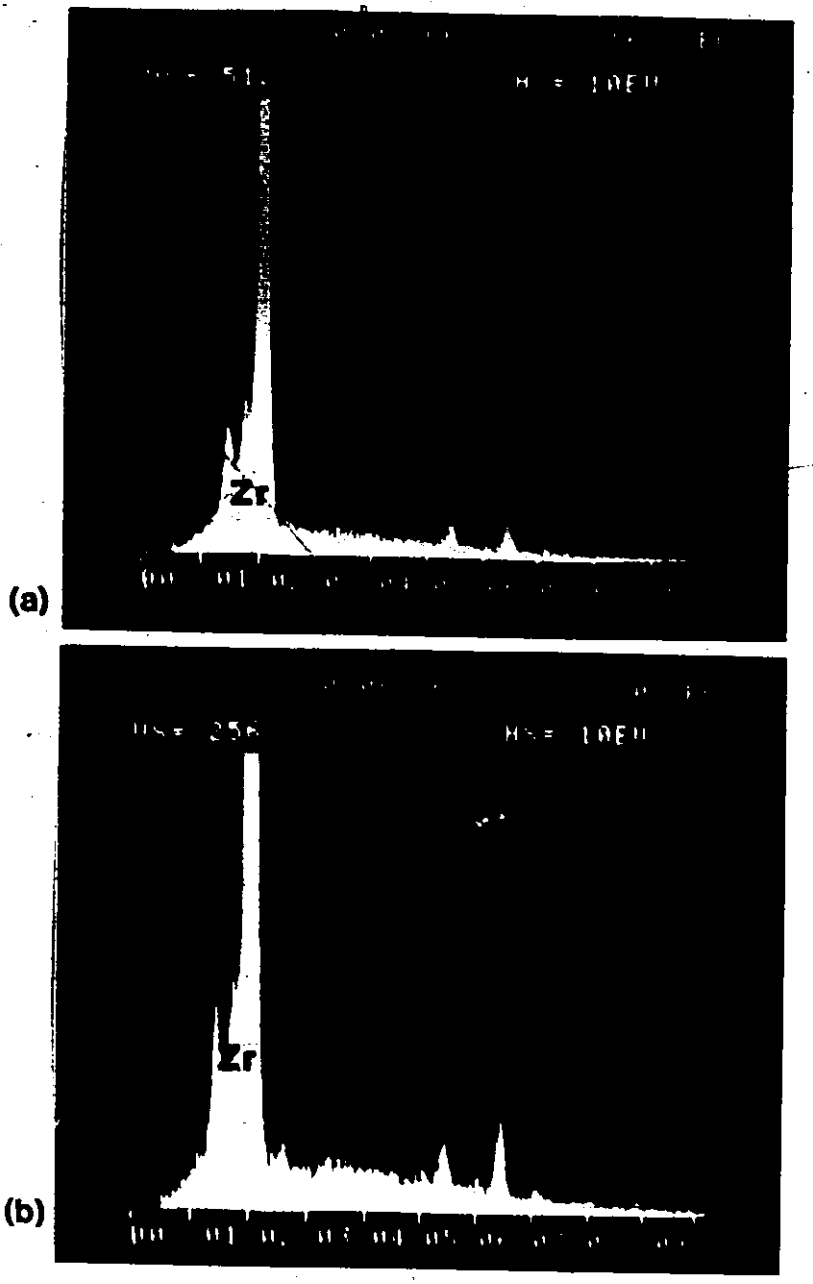

Figure 10: EDS analysis of compounds. (a,b) EDS of the $Zr(CrFe)_2$ precipitates; showing Cr, Fe, Zr. (c) A spectrum for precipitates in Zircaloy-4 which is composed of Zr, Sn and Ni.

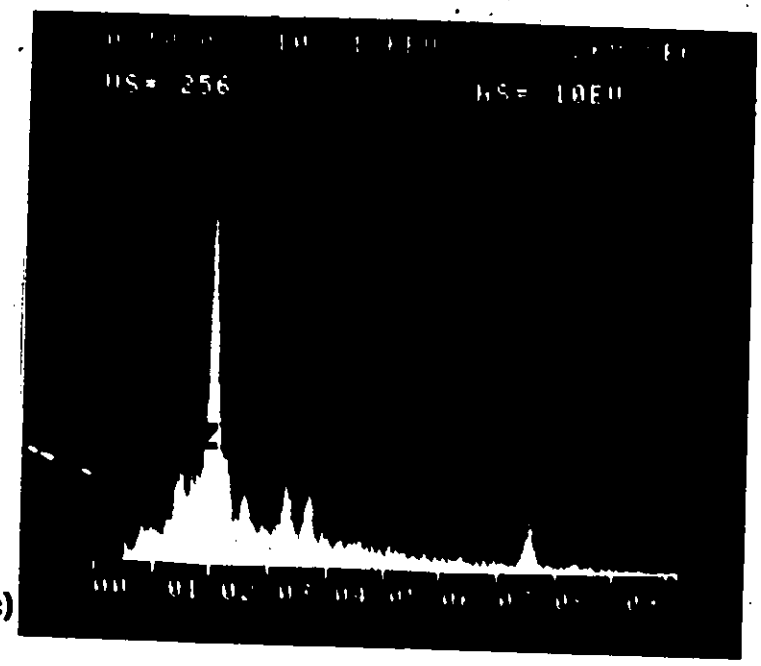

(c)

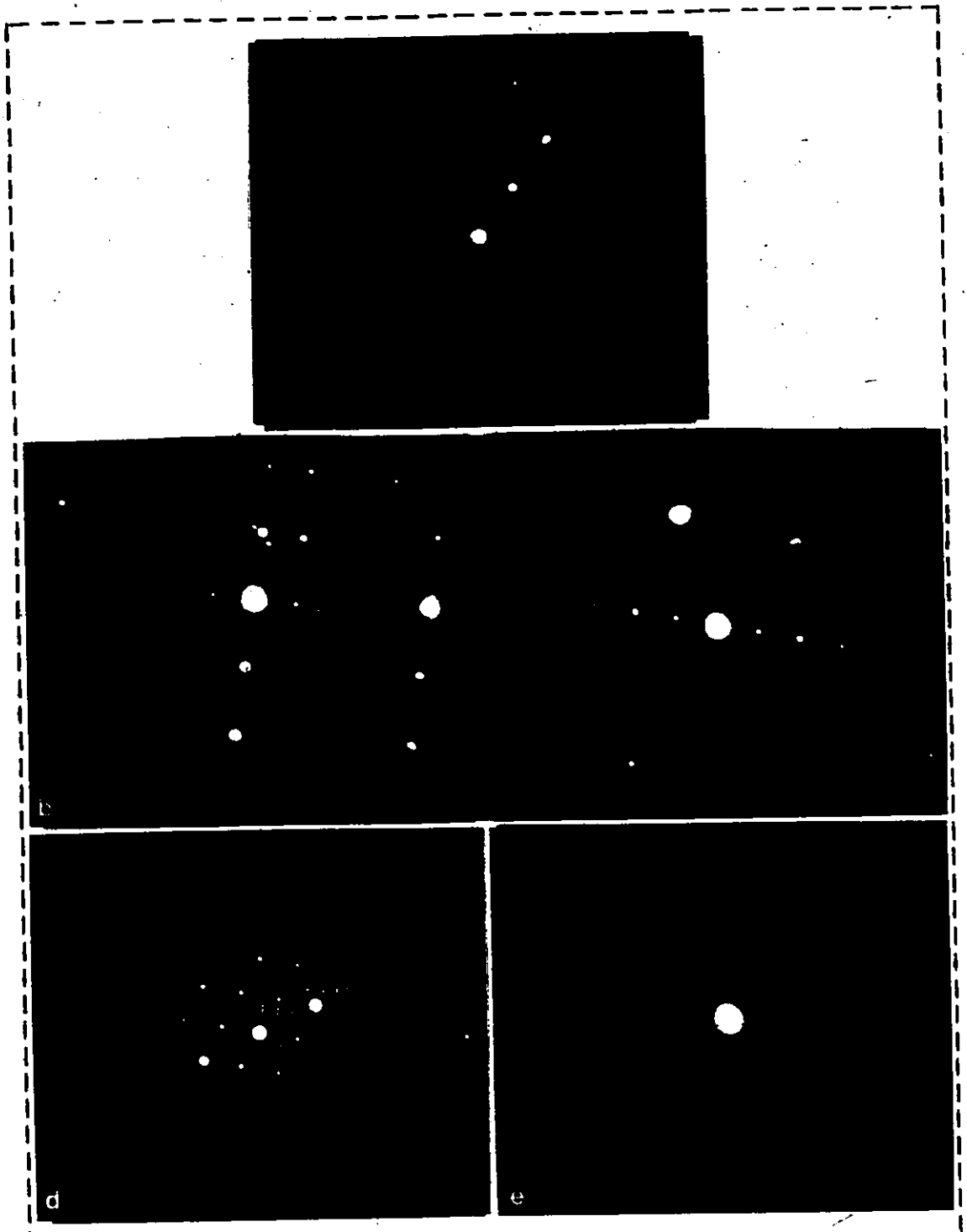

Figure 11: A series of SAD patterns for the $Zr(CrFe)_2$ Laves phase. (a) $[3\bar{2}1]$, (b) $[2\bar{1}1]$, (c) $[3\bar{1}2]$, (d) $[1\bar{1}0]$ and (e) $[3\bar{4}\bar{1}]$ zone axes respectively.

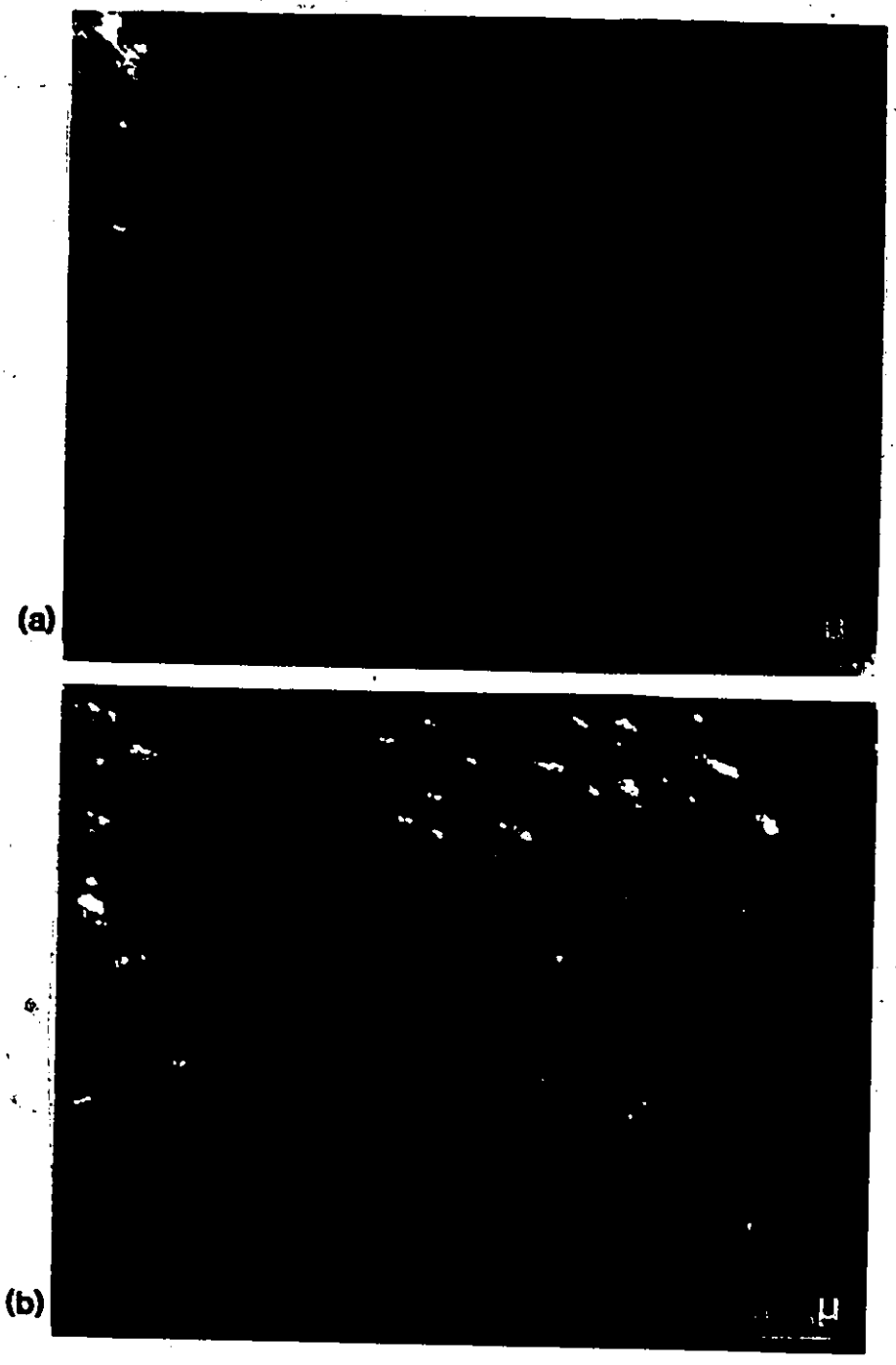

Figure 12: Cubic $Zr(CrFe)_2$ precipitates found within the grains in Zircaloy-4. Micrographs show (a) bright field image; (b) dark field image.

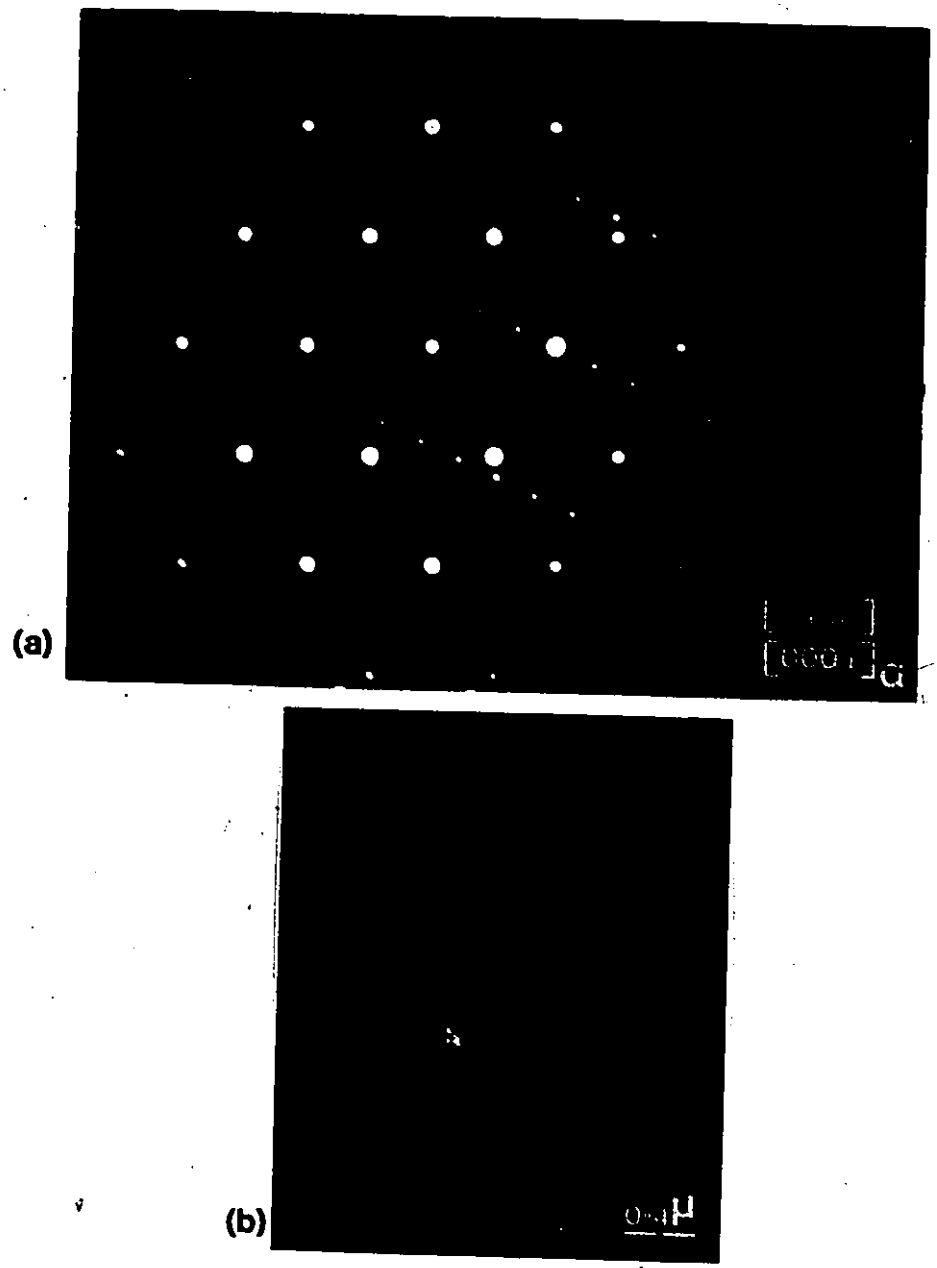

Figure 13: Hexagonal $Zr(CrFe)_2$ Laves phase found in Zircaloy-4. (a) SAD pattern of the C14 type $Zr(CrFe)_2$ precipitate showing the indexing of the diffraction pattern and the orientation relationship between the $Zr(CrFe)_2$ Laves phase and α-Zr; (b) Dark field image of the $Zr(CrFe)_2$ phase.

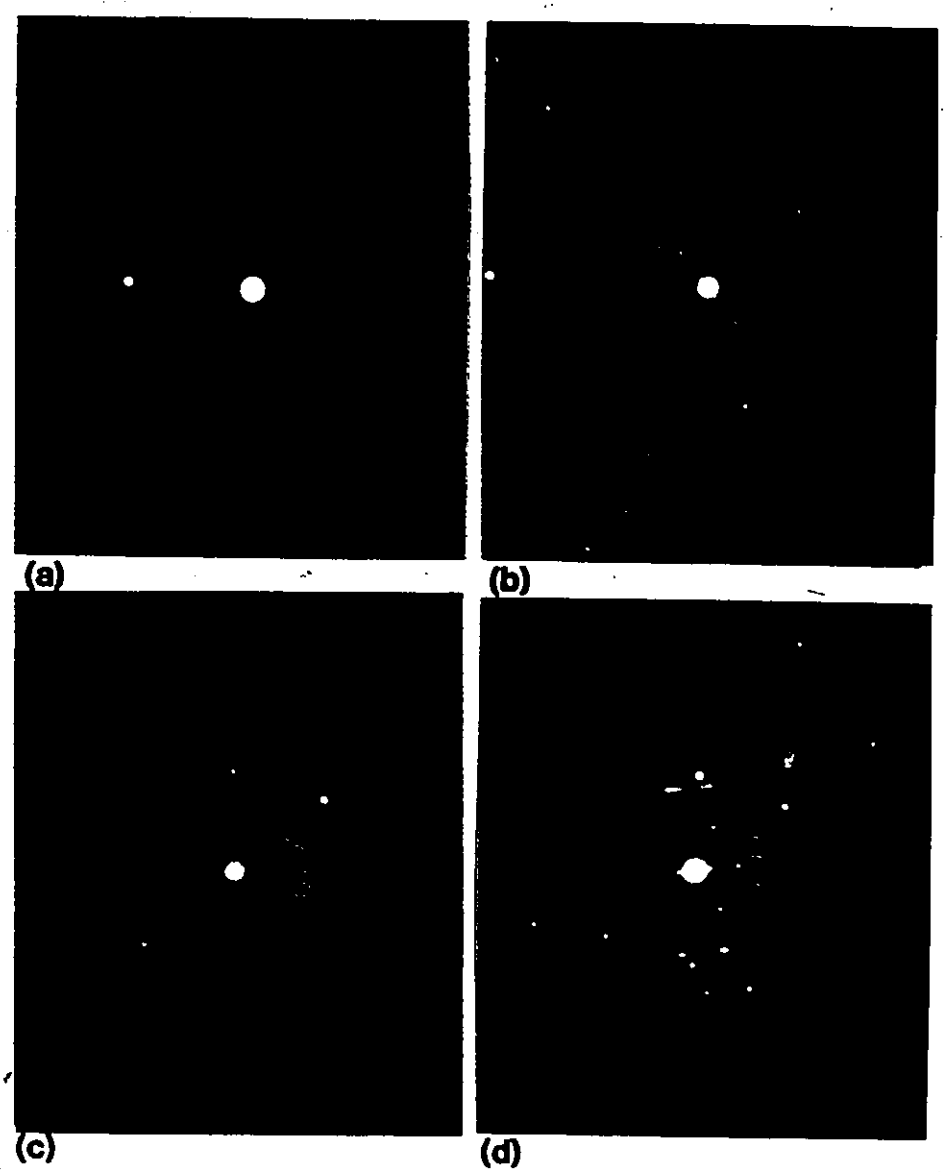

Figure 14: Long period structures of hexagomal $Zr(CrFe)_2$ Laves phases. Long period structures of hexagomal $Zr(CrFe)_2$ Laves phases found in specimen b of Zircaloy-4. (a) $[01\bar{1}0]$ zone axis SAD pattern of $Zr(CrFe)_2$ Laves phase with 2H stacking structure; (b) $[01\bar{1}0]$ zone axis SAD with 6H structure; (c) with 10H structure; (d) $[01\bar{1}0]$ zone axis SAD pattern of heavily faulted precipitates.

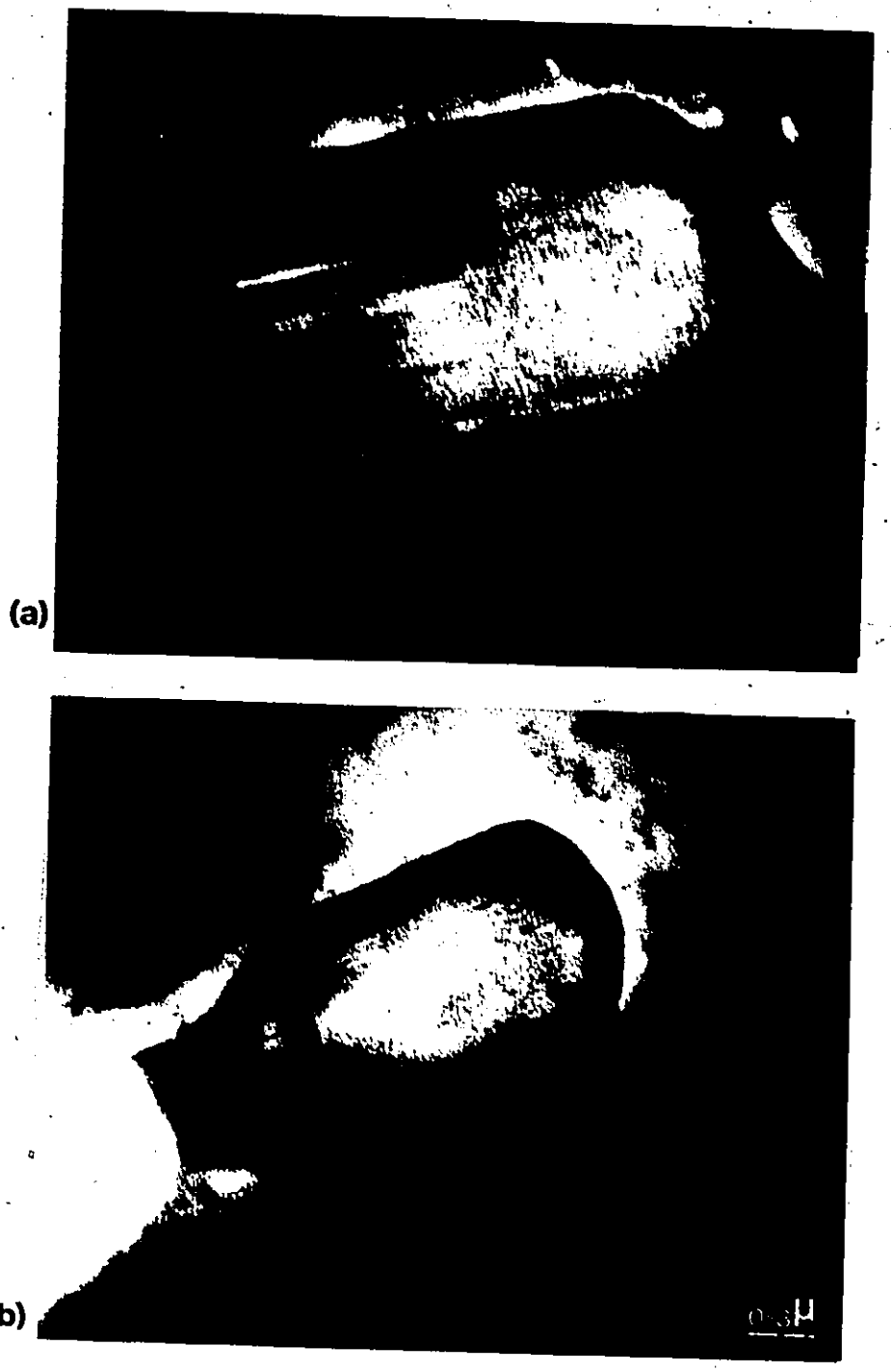

Figure 15: High magnification images of the $Zr(CrFe)_2$ Laves phase. Which show stacking faults in the precipitates of Zircaloy-4.

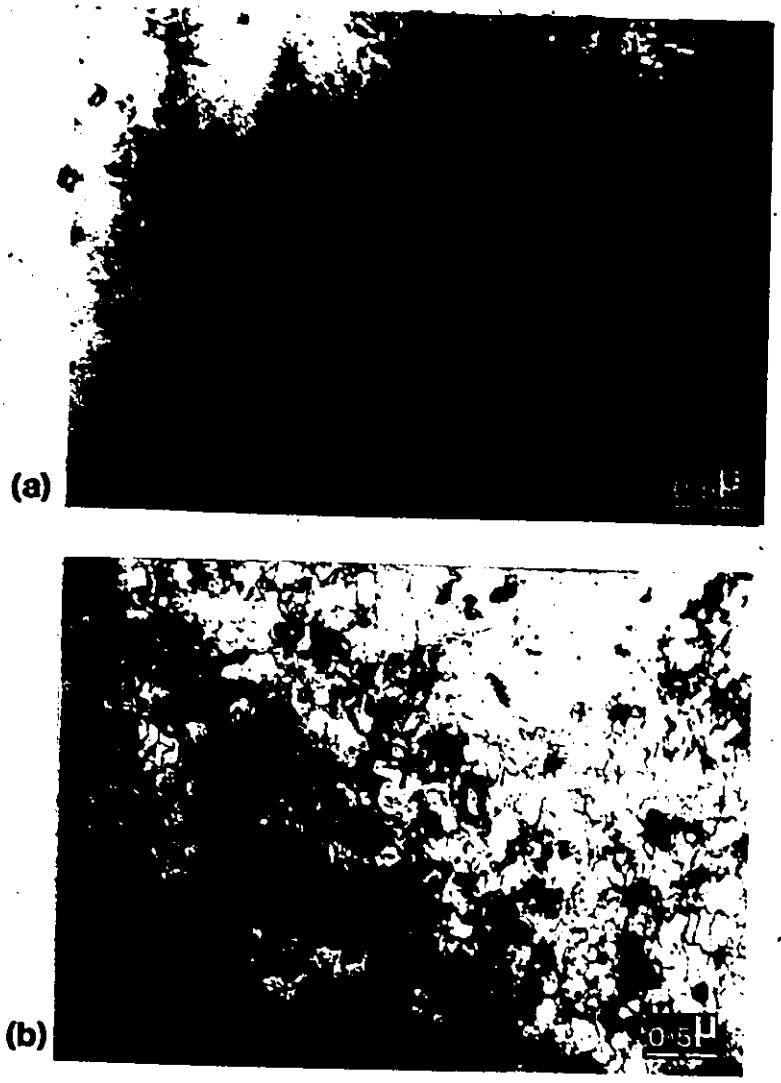

Figure 16: Micrographs for C15 type $Zr(CrFe)_2$ Laves phases in the Zr-Cr-Fe alloy. (a,b) Uniform distribution of the precipitates; (c,d) are bright and dark field images show the distribution of the precipitates along grain boundaries.

(c)

(d)

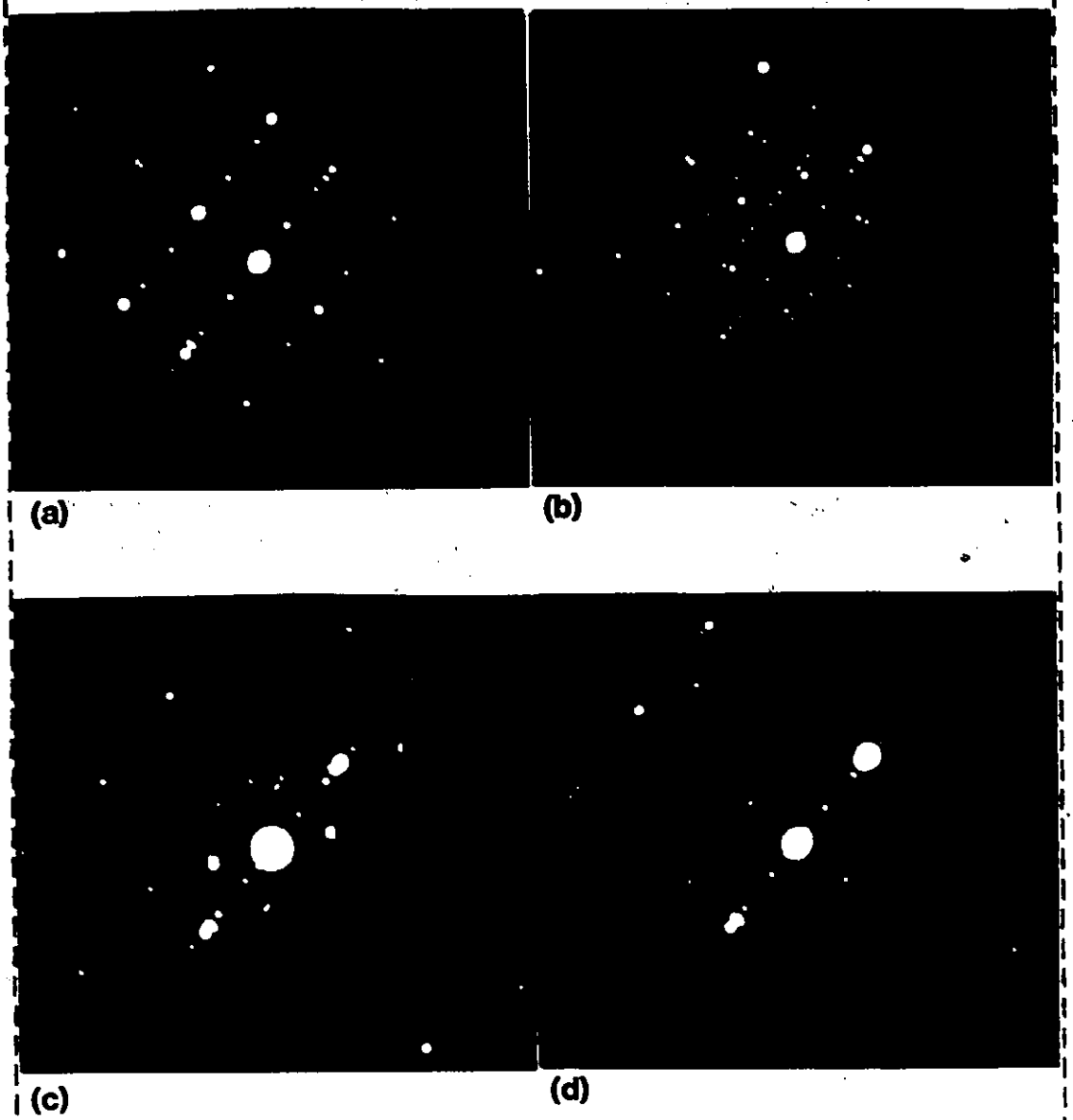

Figure 17: Electron diffraction patterns for the C15 type $Zr(CrFe)_2$ Laves phase and α-Zr matrix. Indexing of these patterns are give in Fig. 18.

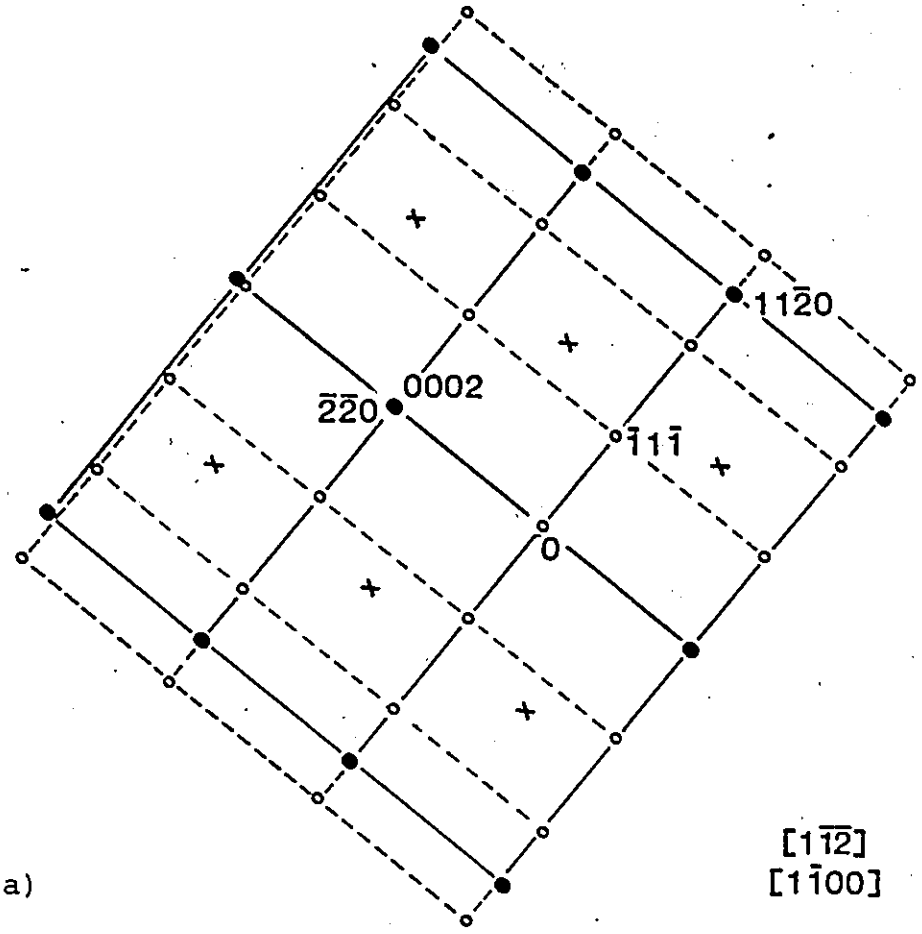

Figure 18: The indexes of SAD in Fig. 17. ●-- α-Zr, X-- extra diffracion spots due to elastic distortion in α-Zr, o— $Zr(CrFe)_2$ precipitates, O-- twinning of $Zr(CrFe)_2$, x-- extra spots due to twinning double diffraction cf $Zr(CrFe)_2$ Laves phase. (a) Orientation is $[1\bar{1}\bar{2}]$ for $Zr(CrFe)_2$ and $[1\bar{1}00]$ for α-Zr. The SAD shows twin diffraction pattern with $(\bar{1}1\bar{1})$ twin axis. (b) $[0\bar{1}\bar{1}]$ for $Zr(CrFe)_2$ and [0001] for α-Zr. (c) $[\bar{3}25]$ for $Zr(CrFe)_2$ shows twin reflection of $[\bar{1}1\bar{1}]$ twin axis and extra spots for both α-Zr and the precipitates. (d) Diffraction pattern shows extra spots due to twinning reflection and elastic distortion.

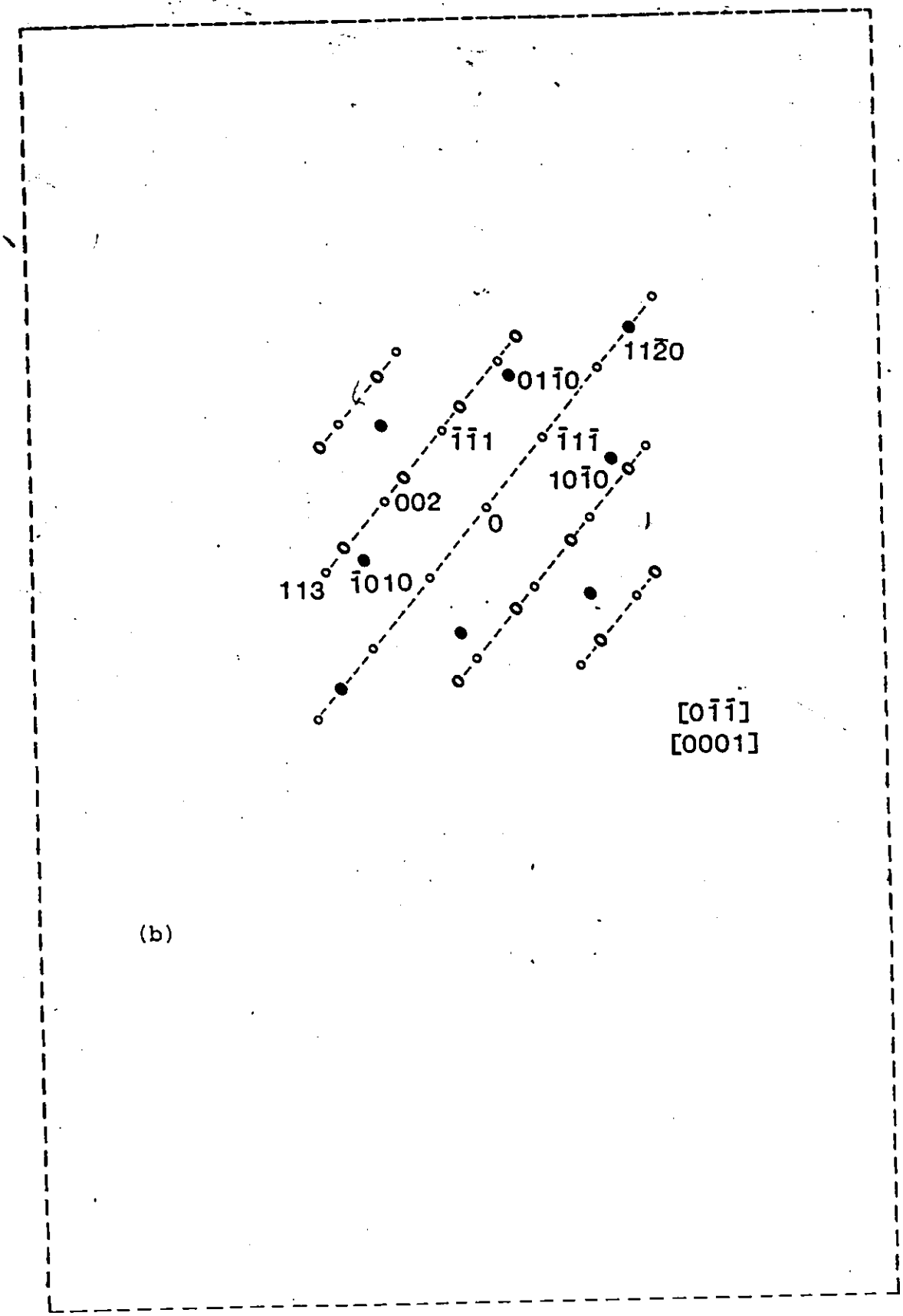
$11\bar{2}0$
$01\bar{1}0$
$\bar{1}\bar{1}1$
$\bar{1}1\bar{1}$
$10\bar{1}0$
002
0
113
$\bar{1}010$
$[0\bar{1}\bar{1}]$
[0001]

(b)

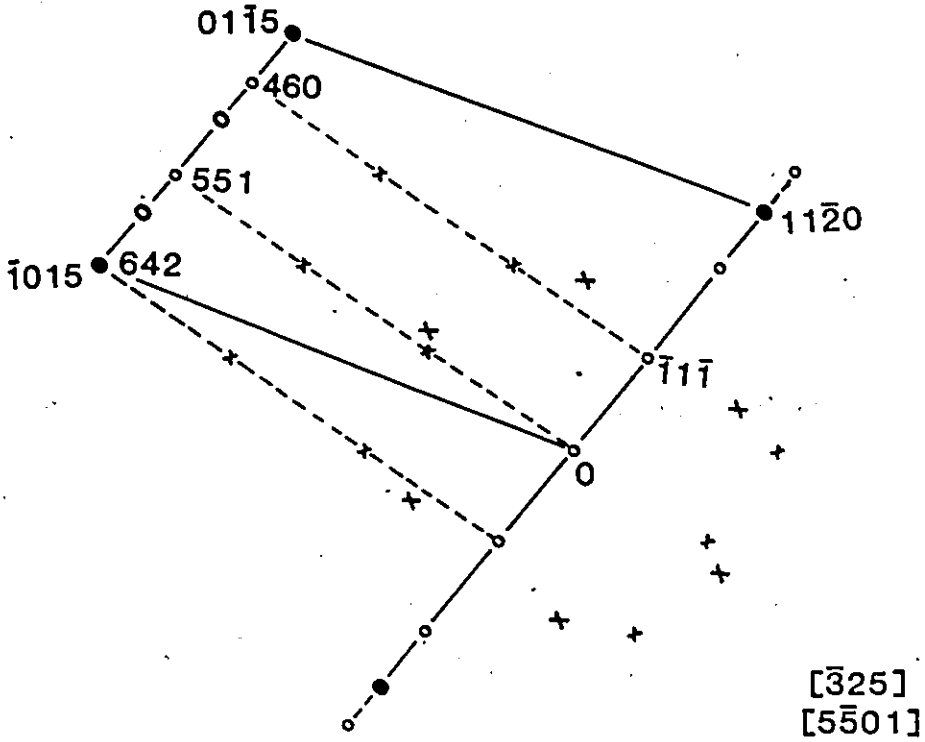
01$\bar{1}$5
460
551
$\bar{1}$015
642
11$\bar{2}$0
$\bar{1}$1$\bar{1}$
0
[$\bar{3}$25]
[5$\bar{5}$01]

(c)

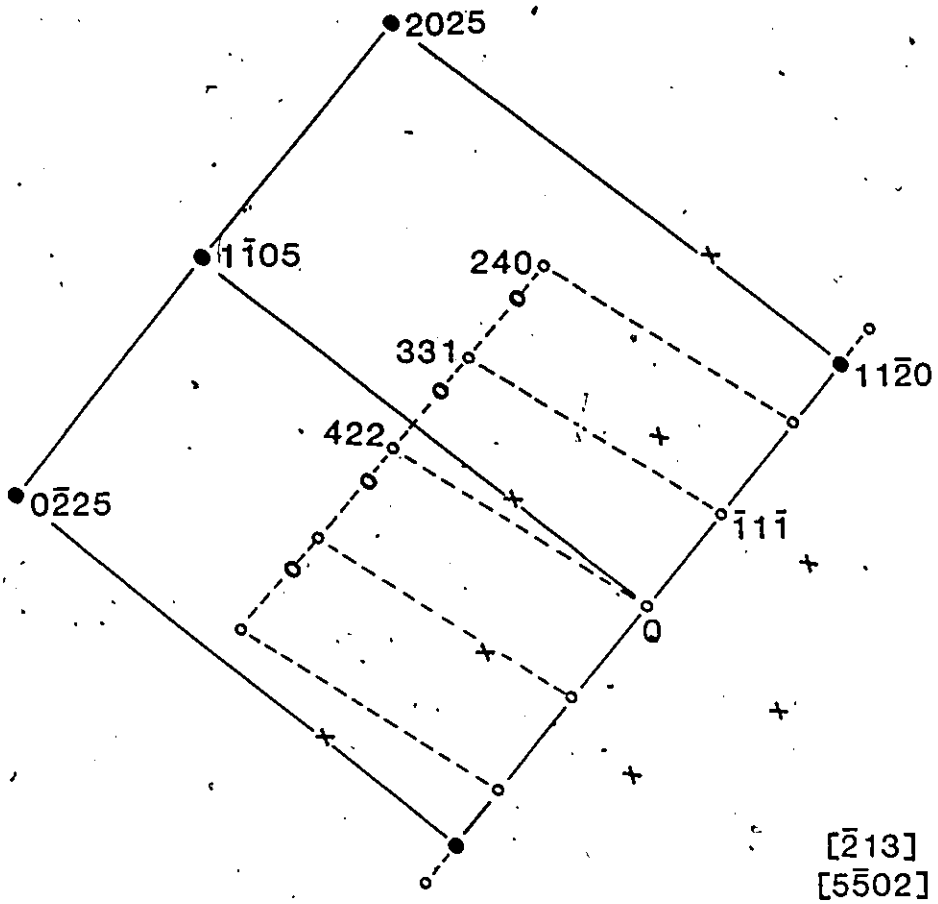
2025
1$\bar{1}$05
240
331
11$\bar{2}$0
422
0$\bar{2}$25
$\bar{1}$1$\bar{1}$
0
[$\bar{2}$13]
[5$\bar{5}$02]

(d)

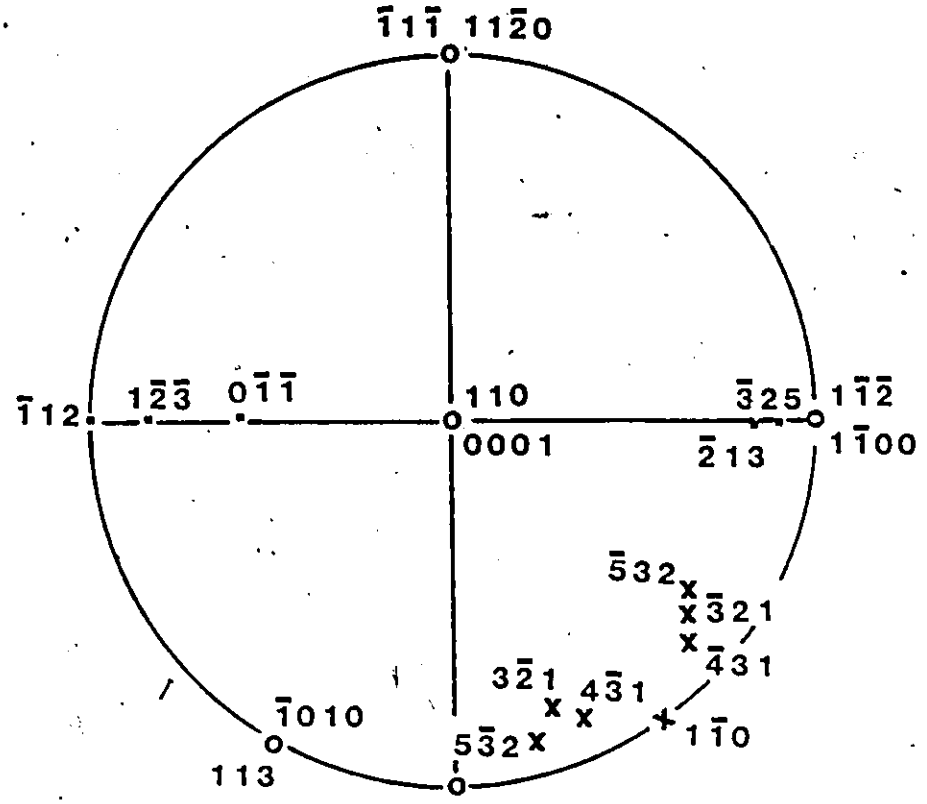

Figure 19: A stereogram of cubic [110] and hcp [0001]. The stereogram showing mutual positions of diffraction patterns, which were taken by electron diffraction, and the orientation relationship between $Zr(CrFe)_2$ and α-Zr.

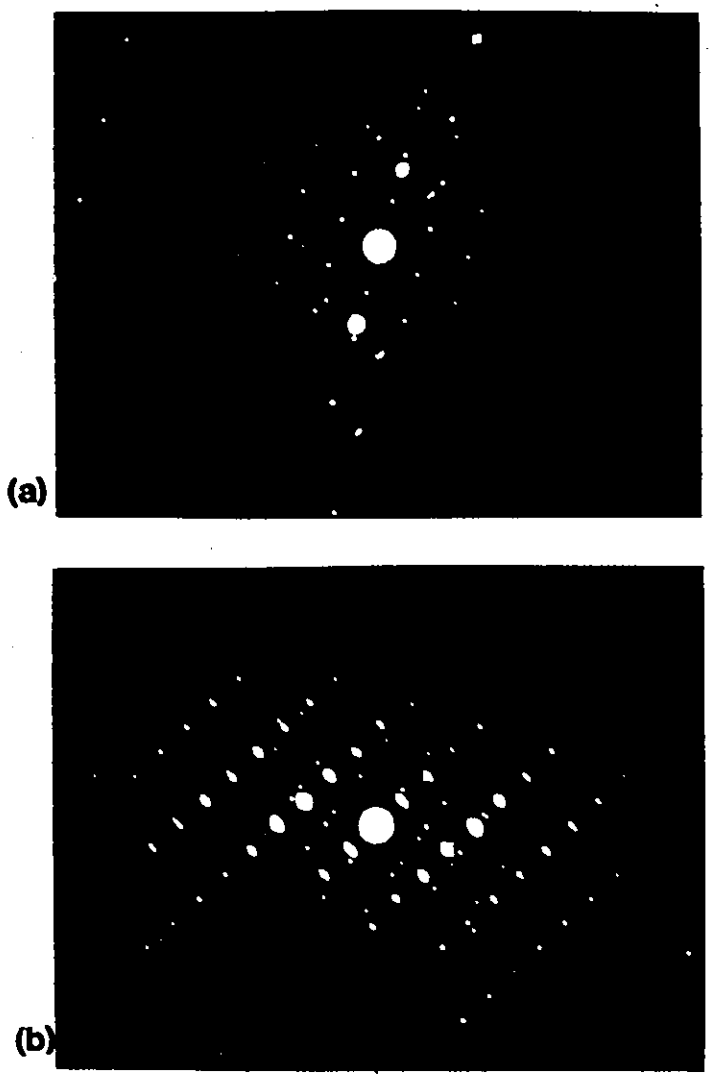

Figure 20: Diffraction patterns for the precipitates with multiple twinned. (a,b) Diffraction patterns of [110] orientation for the $Zr(CrFe)_2$ precipitates with multiple twinning. (c) The indexing of diffraction patterns shown in (a,b).

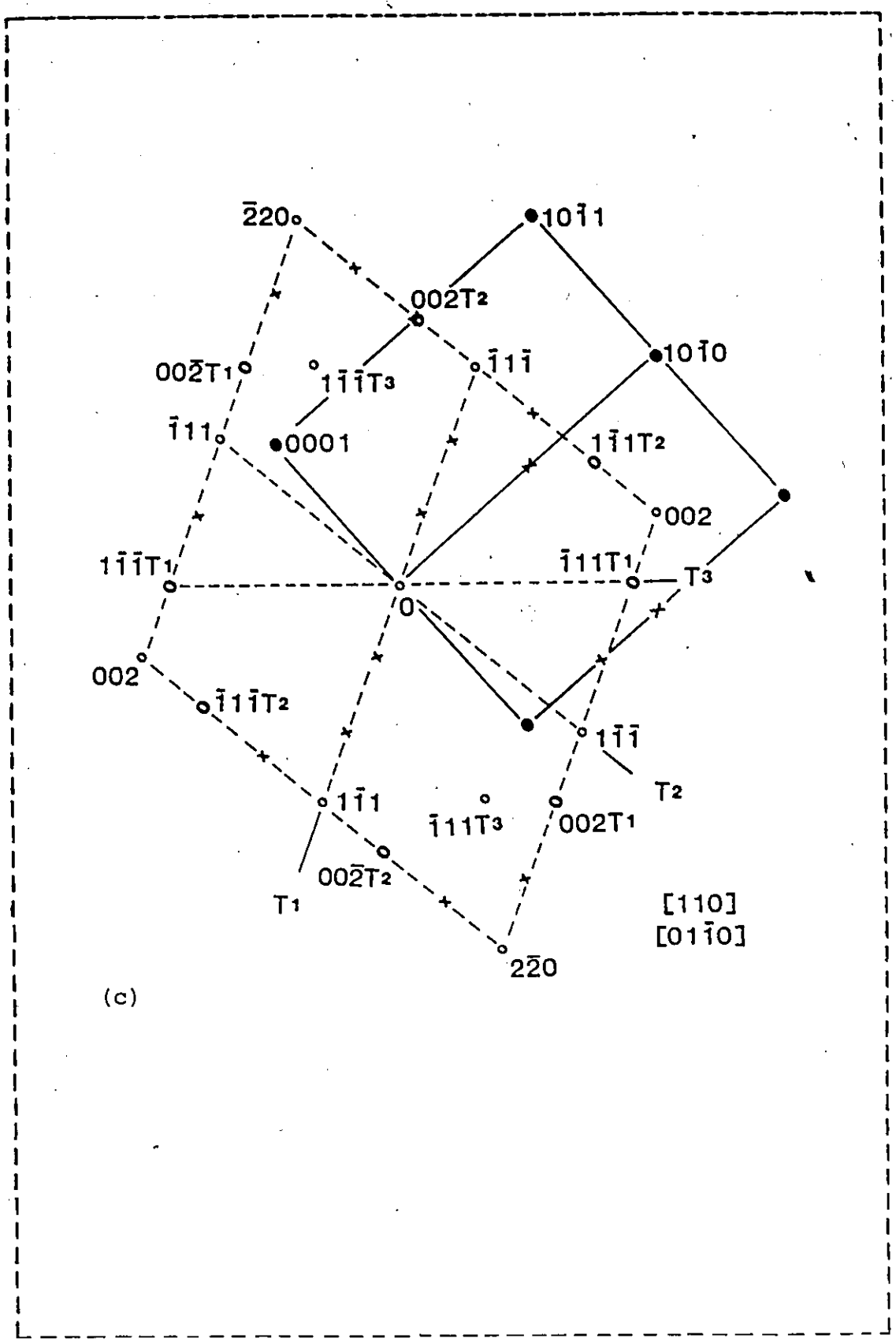
$\bar{2}20$
$10\bar{1}1$
$002T_2$
$002\bar{T}_1$
$1\bar{1}\bar{1}T_3$
$\bar{1}1\bar{1}$
$10\bar{1}0$
$\bar{1}11$
0001
$1\bar{1}1T_2$
002
$1\bar{1}\bar{1}T_1$
$\bar{1}11T_1$
T_3
0
002
$\bar{1}1\bar{1}T_2$
$1\bar{1}\bar{1}$
T_2
$1\bar{1}1$
$\bar{1}11T_3$
$002T_1$
T_1
$002\bar{T}_2$
[110]
$[01\bar{1}0]$
$2\bar{2}0$
(c)

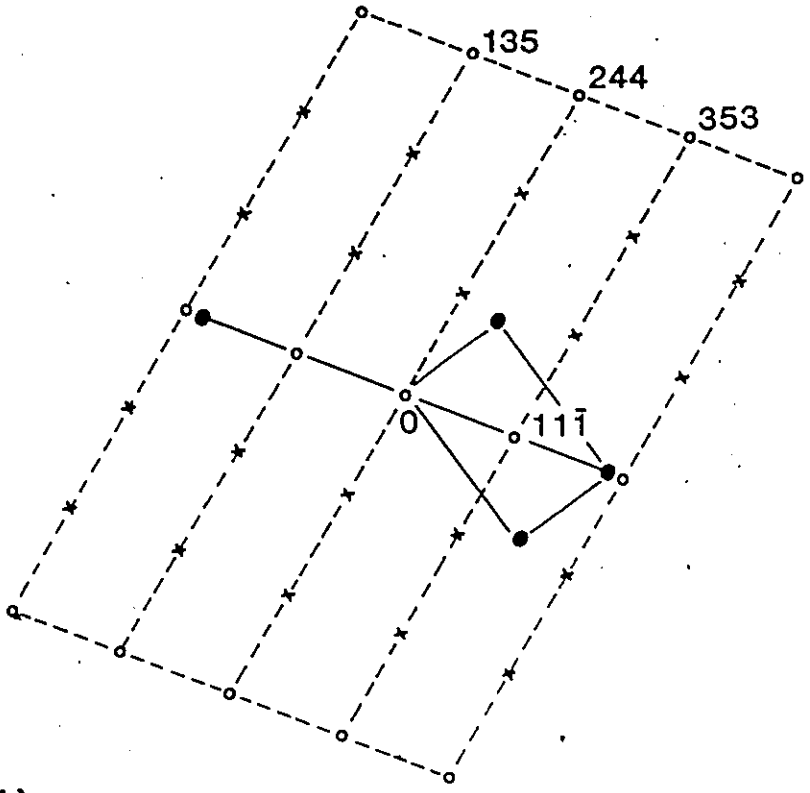

Figure 21: The diffraction pattern of [4$\bar{3}$1] involved extra spots. The diffraction pattern (a) and the index (b) of [4$\bar{3}$1] for the $Zr(CrFe)_2$ involved extra reflection spots with twinning.

Figure 22: Micrographs of the $Zr(CrFe)_2$ precipitates having multiple twinning.

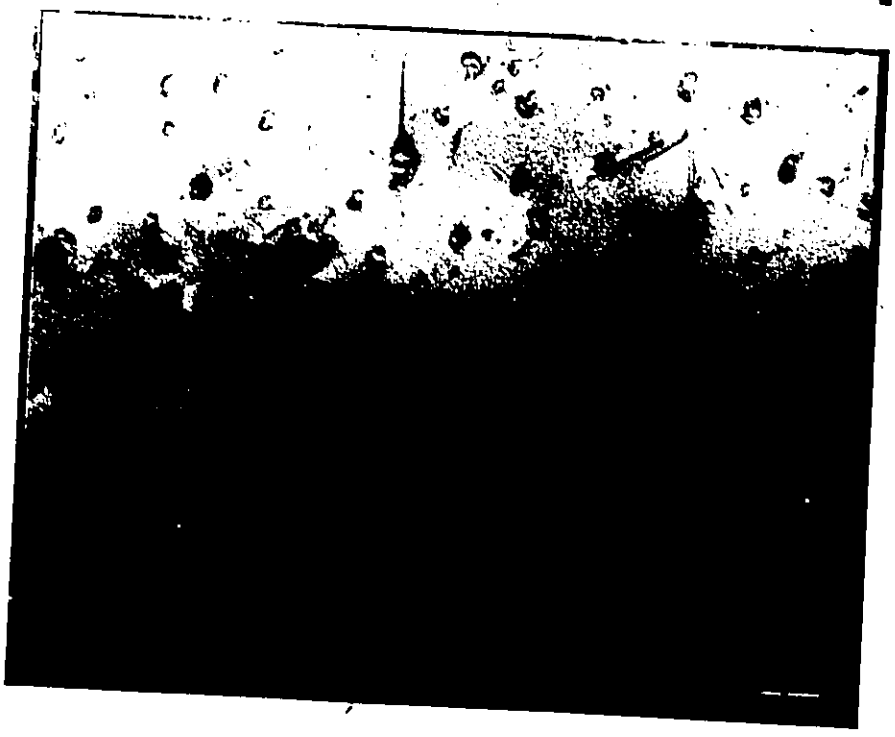

Figure 23: Micrograph of dislocations formed in Zircaloy-4. Micrograph showing that the dislocations formed in the α-Zr matrix are associated with precipitates.

(c)

(d)

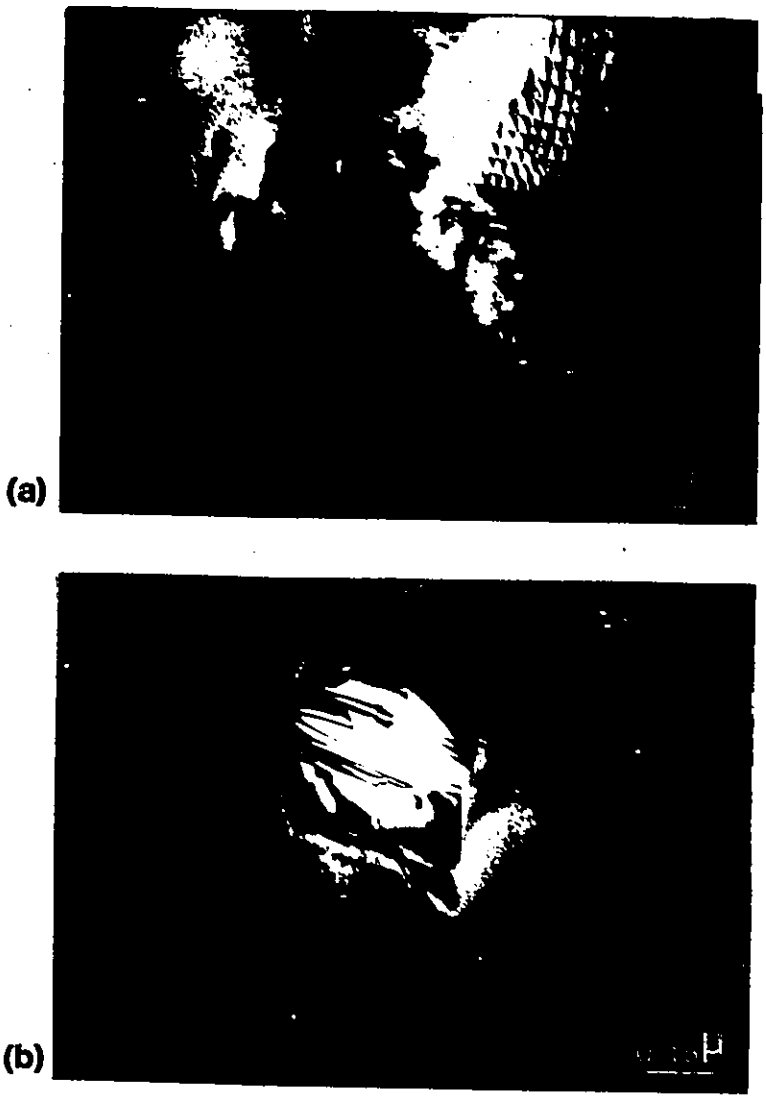

Figure 24: Micrographs of dislocations produced in the Zr-Cr-Fe alloy. Micrographs showing the dislocations produced in (a) the α-Zr matrix and (b) the precipitates in the Zr-Cr-Fe alloy.

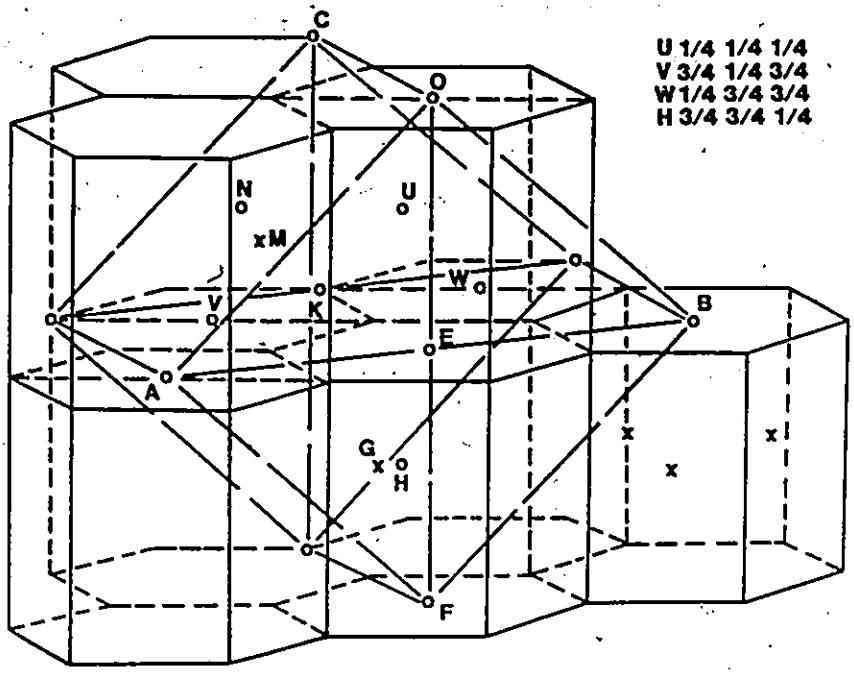

(a)

Figure 25: The model for the transformation and orientation relationship of α-Zr matrix to cubic $Zr(CrFe)_2$ Laves phase. (a) The model, (b) the plot of computer confirms the possibility of the model.

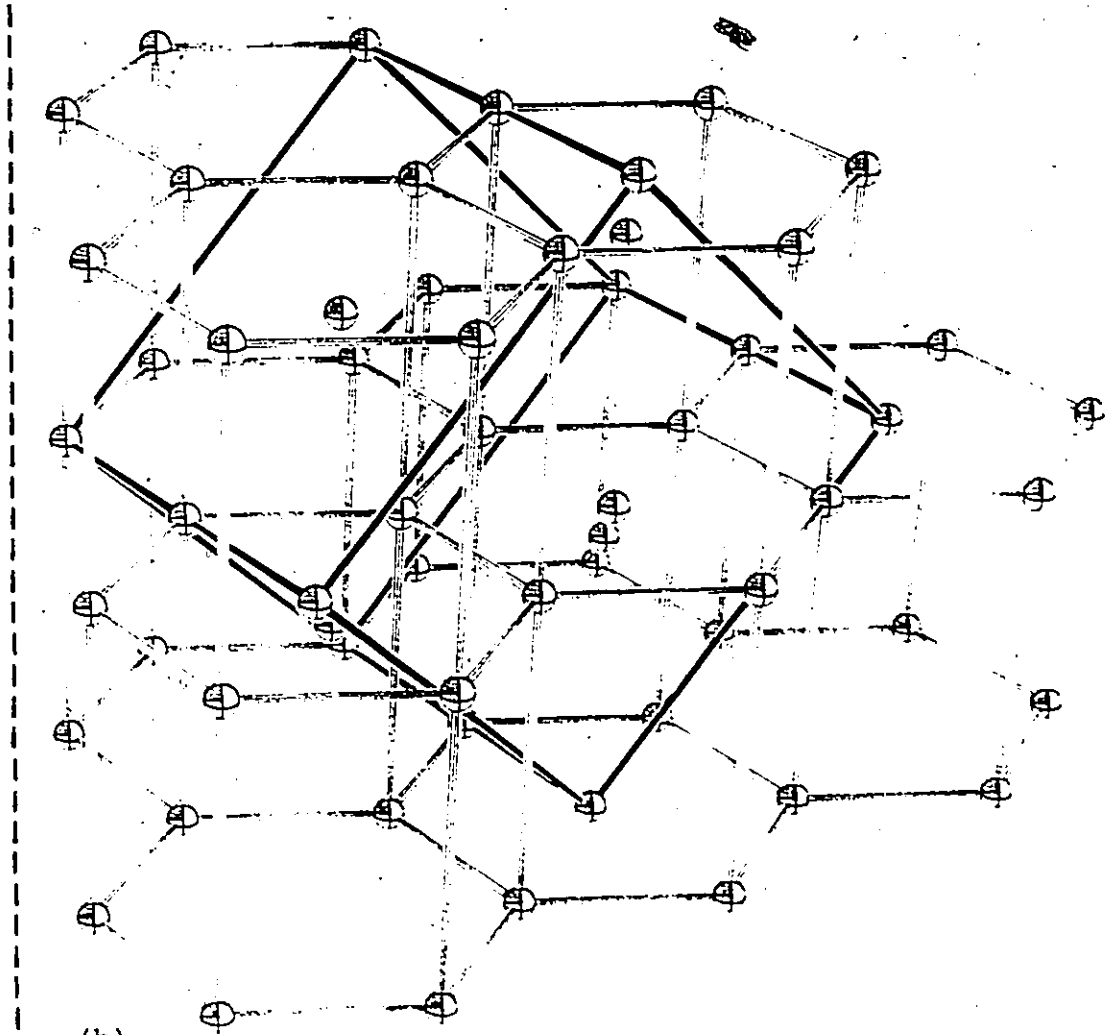

(b)

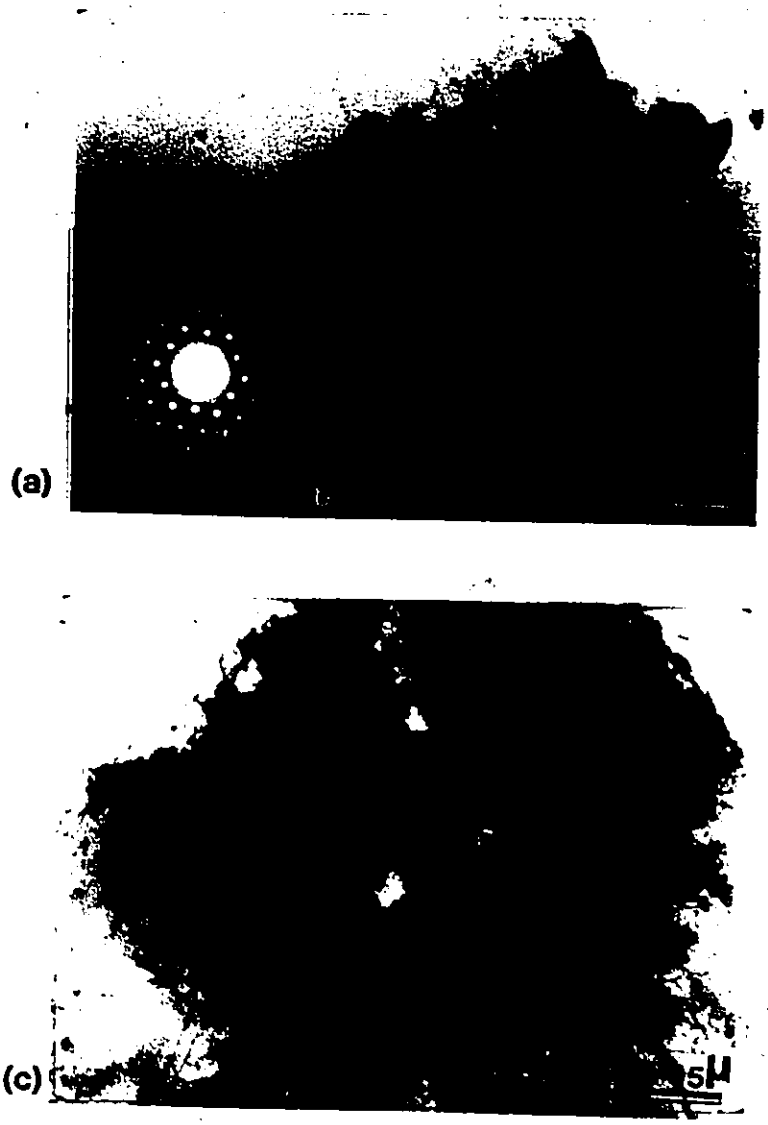

Figure 26: Micrographs of $ZrCr_2$ of bulk stoichiometric alloy. (a) Bright field image showing shape of $ZrCr_2$ powders; (b) corresponding diffraction pattern of [0001] zone axis; (c) dislocation distribution along the {100} type directions in a $ZrCr_2$ particle.

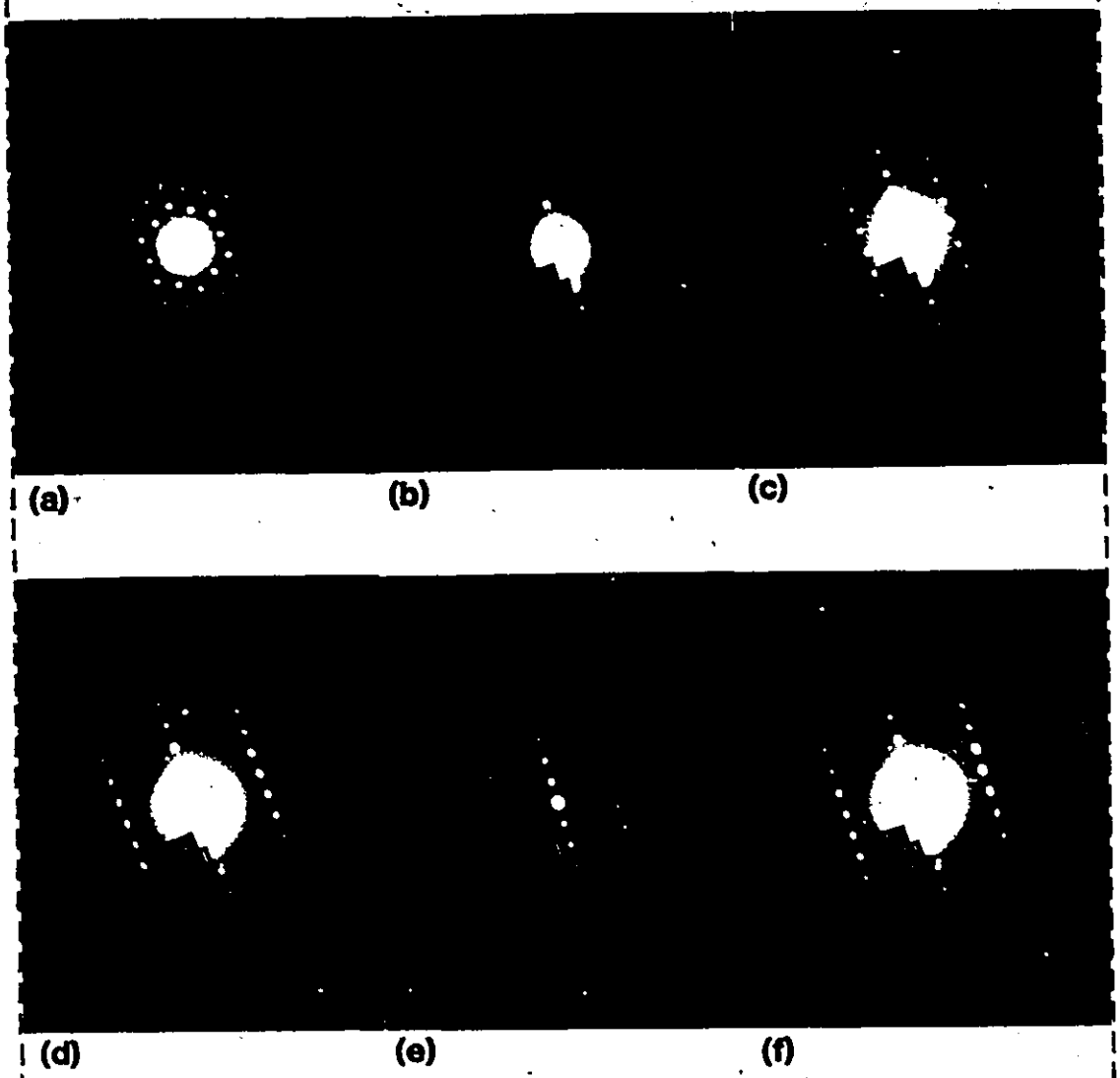

Figure 27: Electron diffraction patterns of C14 $ZrCr_2$ crystal. Electron diffraction patterns including $(h\bar{h}0)^*$ (a-f) or $(001)^*$ (g,h) diffraction spots array from a C14 prototype $ZrCr_2$ crystal. (a) $[001]$, (b) $[11\bar{3}]$, (c) $[11\bar{2}]$, (d) $[22\bar{3}]$, (e) $[22\bar{1}]$ and (f) $[223]$ zone axis; (g) $[010]$ and (h) $[\bar{1}30]$ zone asix.

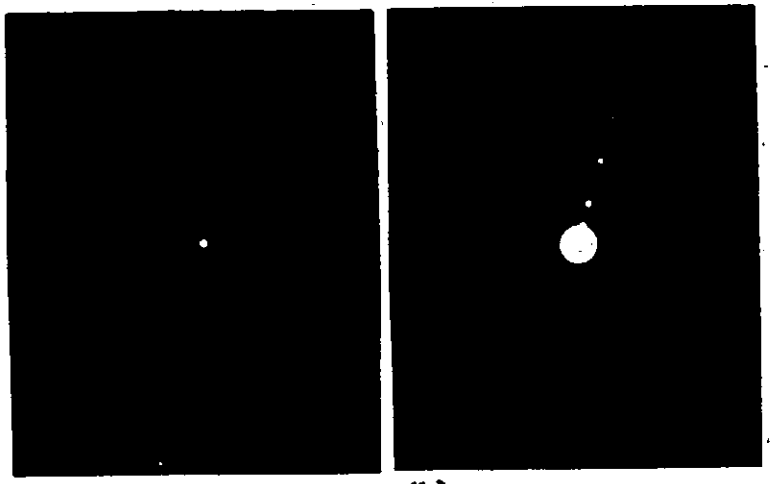

(g) (h)

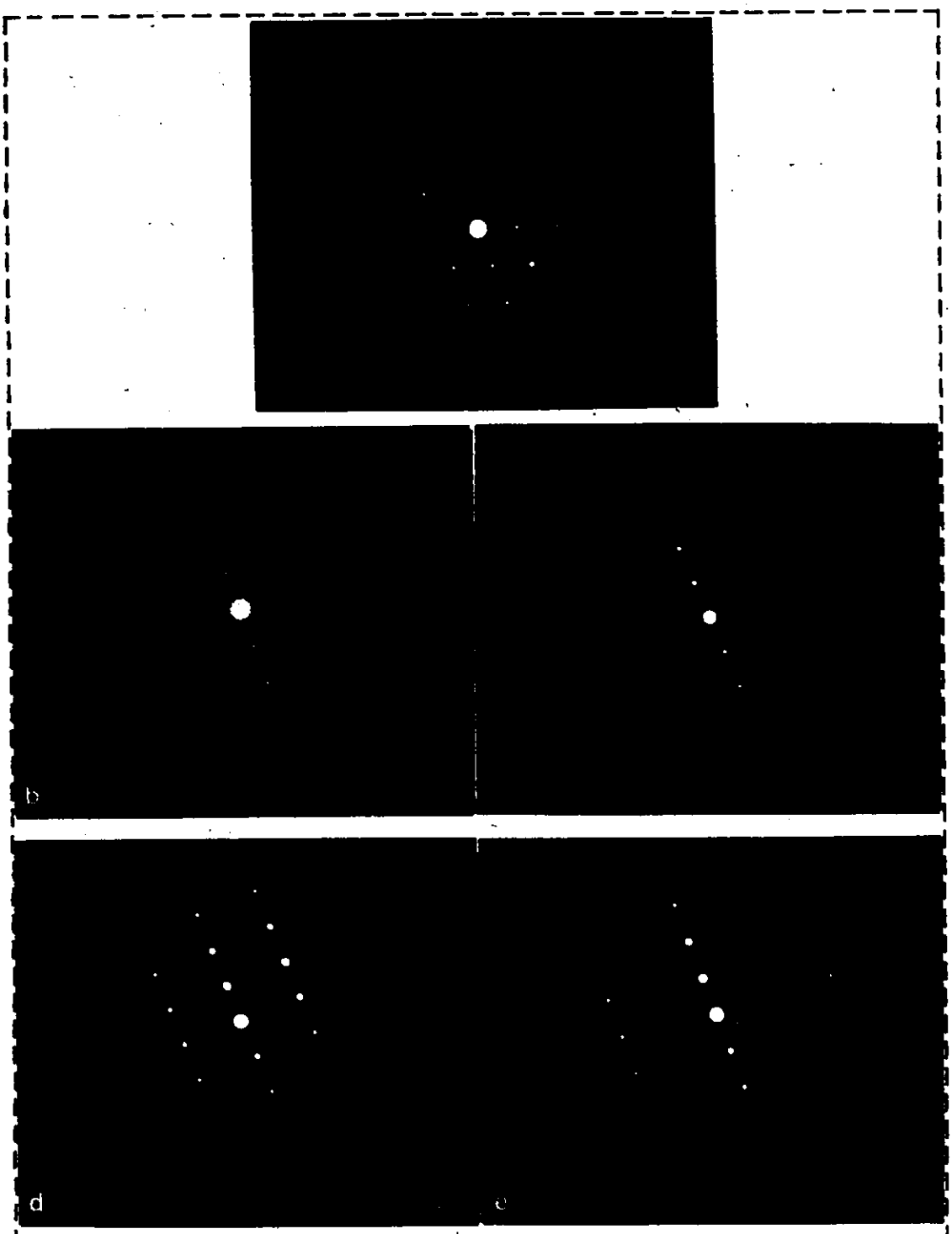

Figure 28: A series SAD patterns of $ZrFe_2$ bulk stoichiometric alloy. A series SAD patterns of C15 type $ZrFe_2$. (a) $[1\bar{1}0]$, (b) $[4\bar{3}1]$, (c) $[3\bar{1}2]$, (d) $[2\bar{1}1]$ and (e) $[3\bar{2}1]$ zone axis.

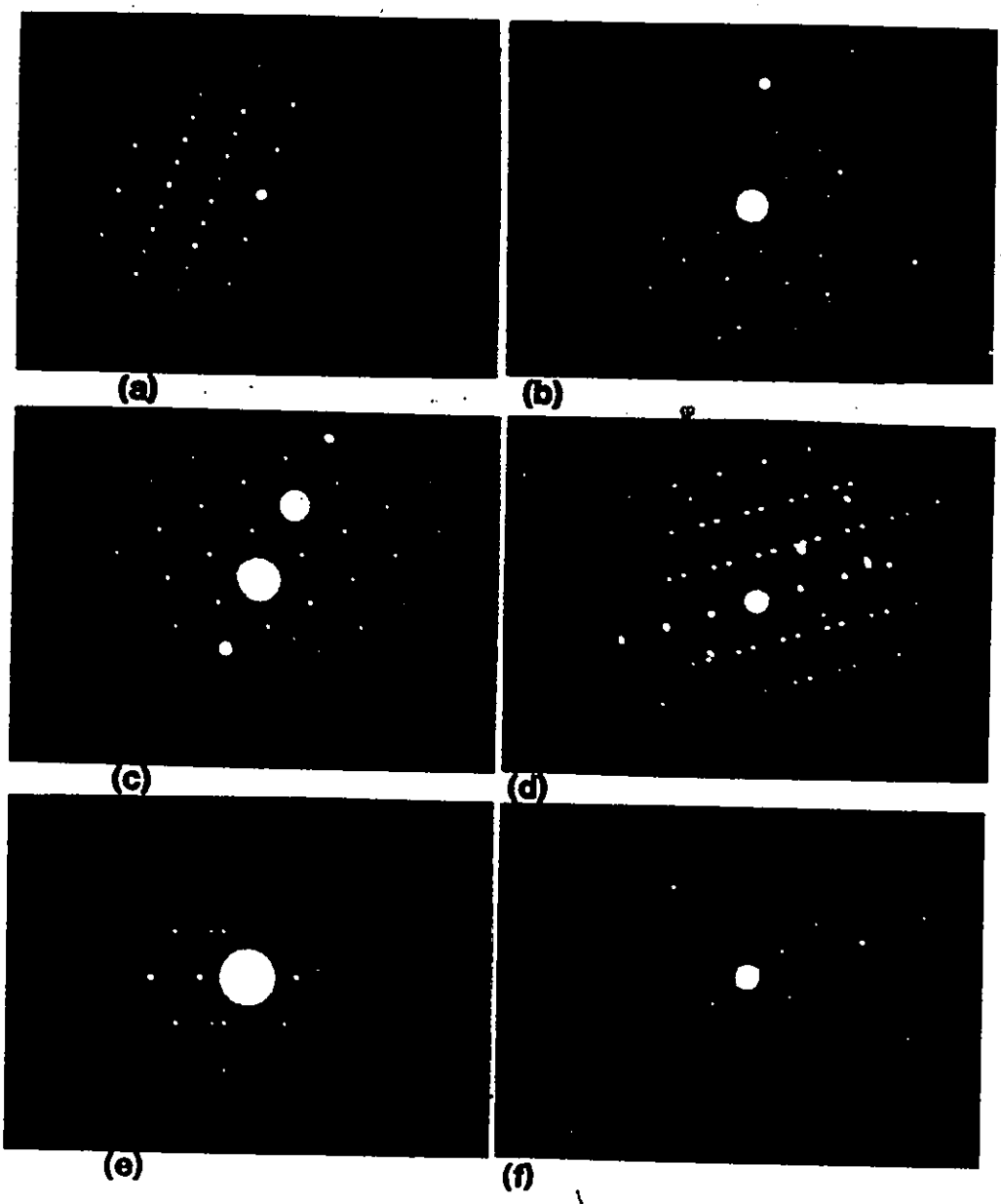

Figure 29: The diffraction patterns of polytype structures. The diffraction patterns of polytype structures for $ZrCr_2$ and $Zr(CrFe)_2$ Laves phases. (a) 2H, (b) 2H, in Zircaloy-4, (c) 3R, in Zircaloy-4, (d) 3R twin, Zr-Cr-Fe alloy, (e) 4H, (f) 6H, Zircaloy-4, (g-i) 8H, (j) 10H, in Zircaloy-4, (k) 12H and 14H, (l) 20H.

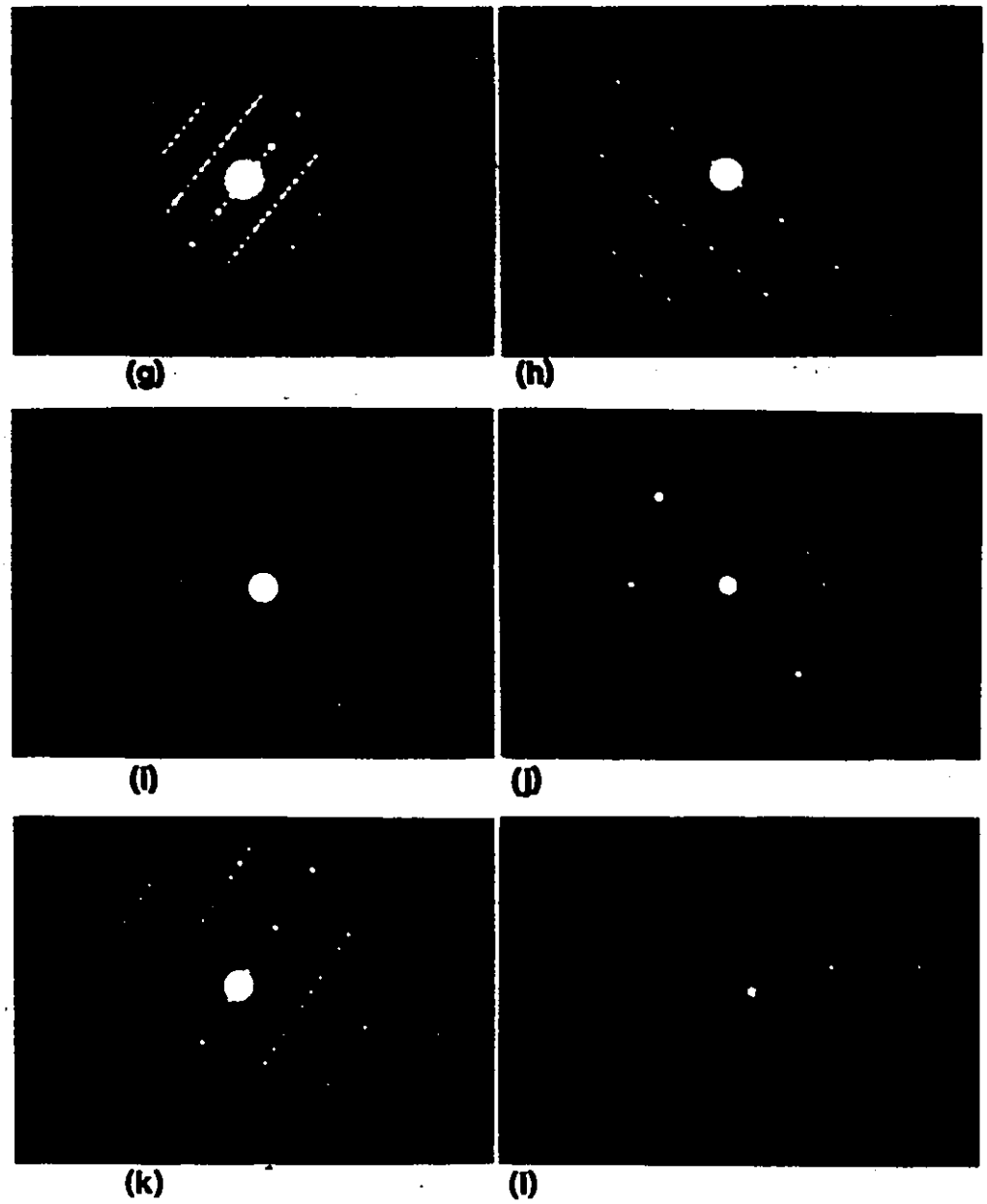
(g)
(h)
(i)
(j)
(k)
(l)

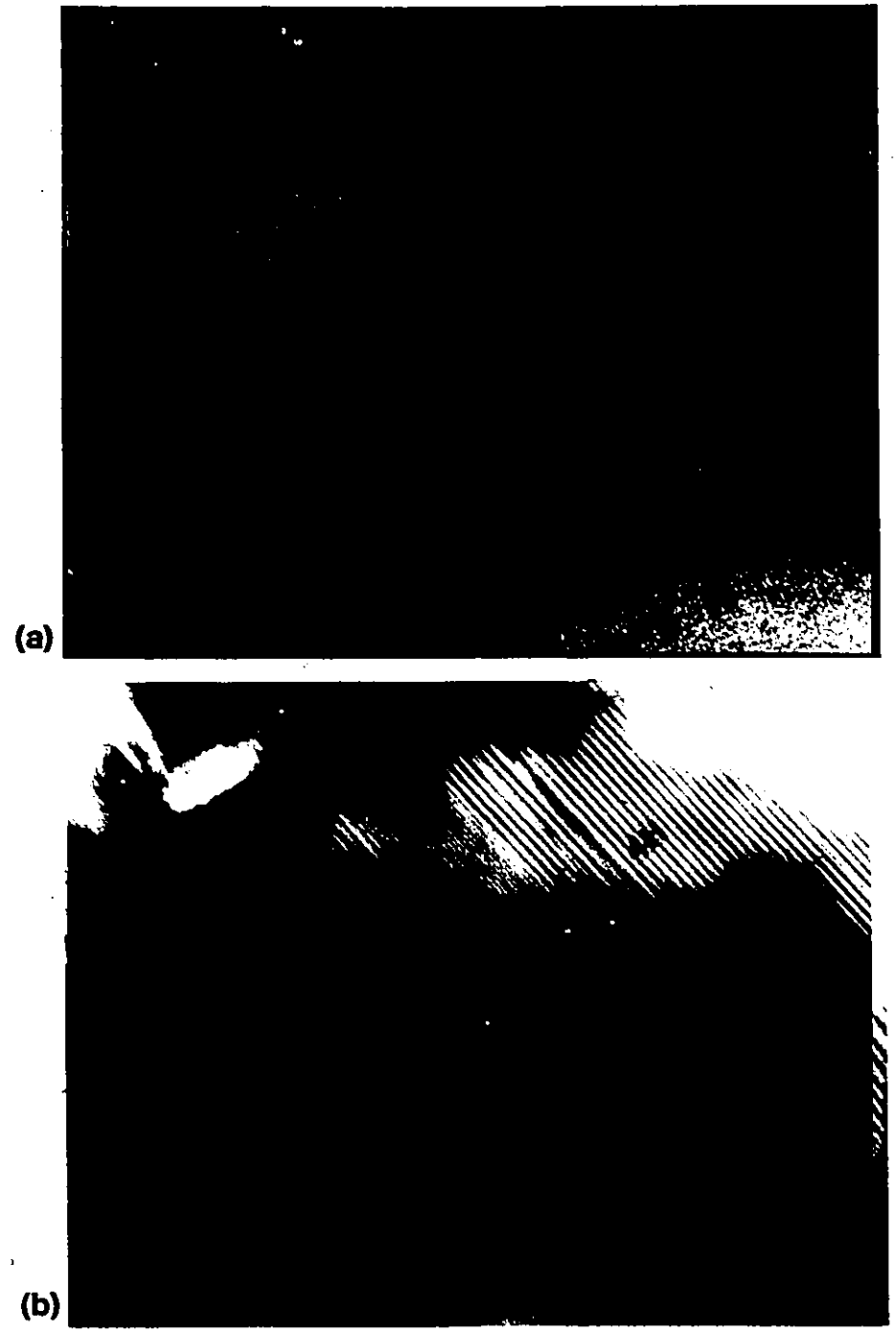

Figure 30: Lattice images of polytype structures for $ZrCr_2$ Laves phases. (a) 2H, $ZrCr_2$ and $Zr(CrFe)_2$, (b) 4H and 8H, (c) 8R and 12H, (d) Diffraction pattern of (c), (e) 12H and 14H, (f) Diffraction pattern of (e).

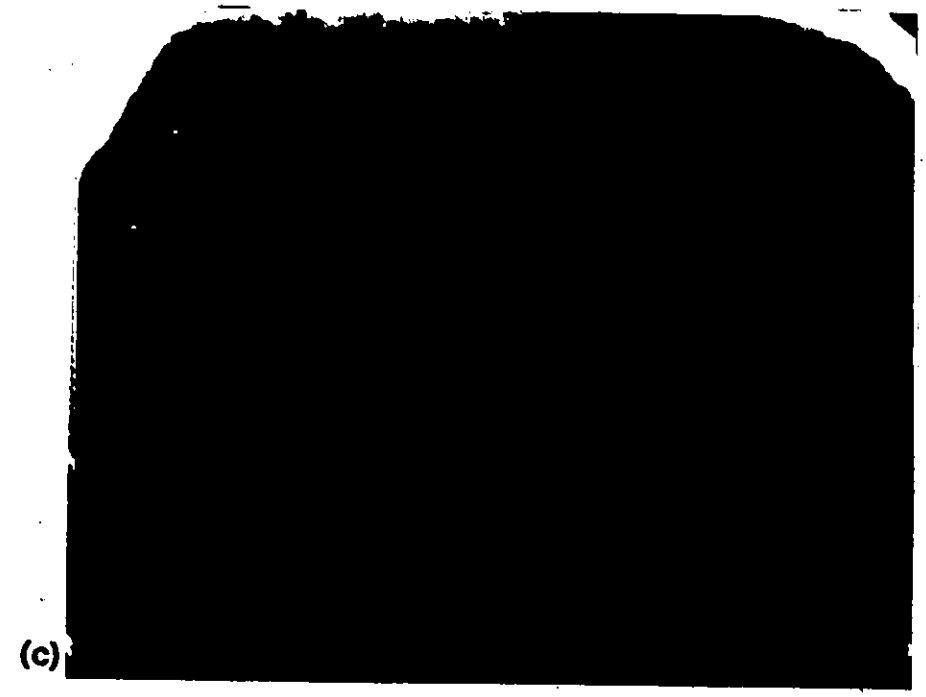

(c)

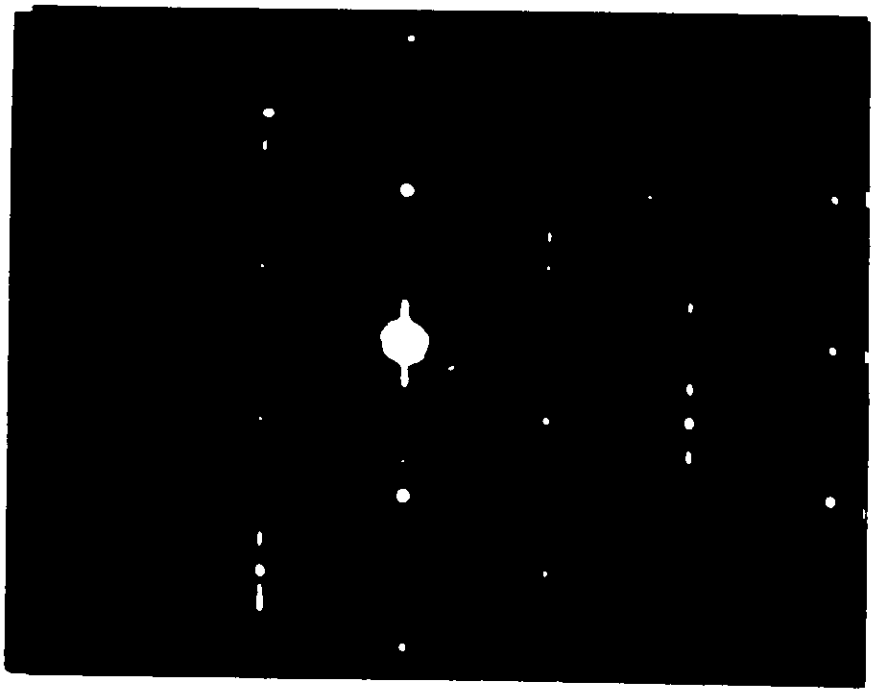

(d)

(e)

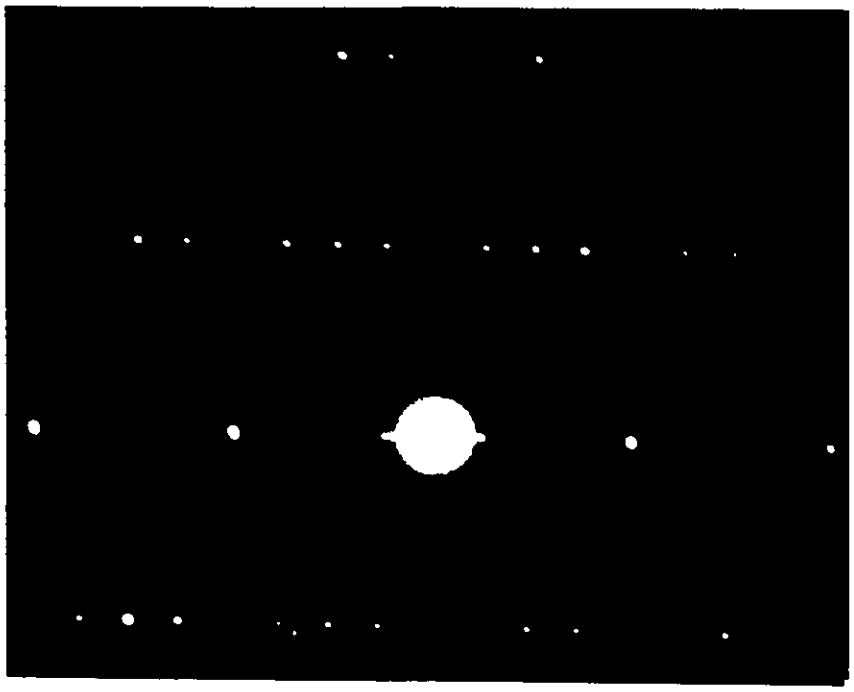

(f)

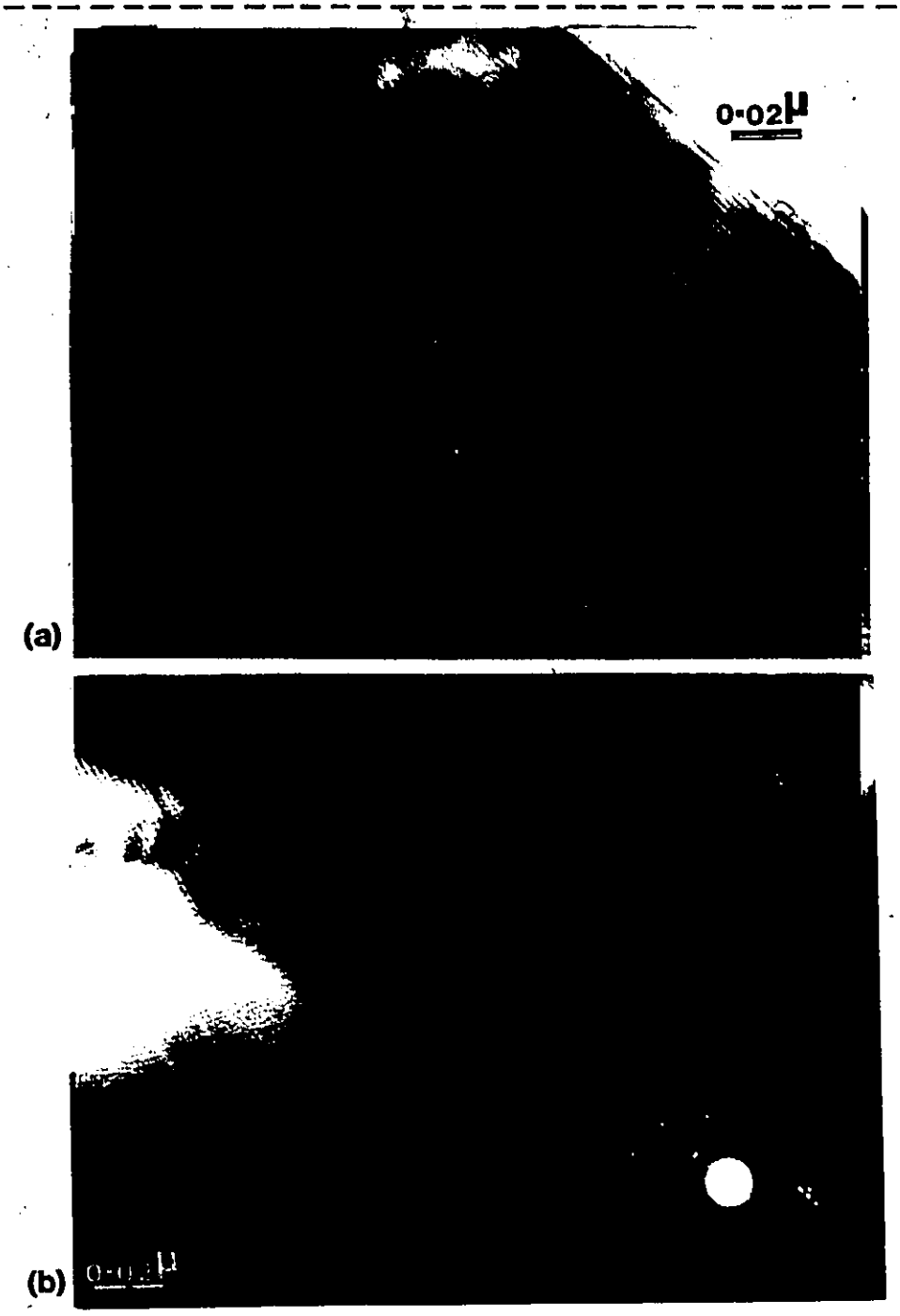

Figure 31: Lattice images of defect structures for $ZrCr_2$ alloy. (a) Defect structures and (b) moire pattern from two 8H structures.

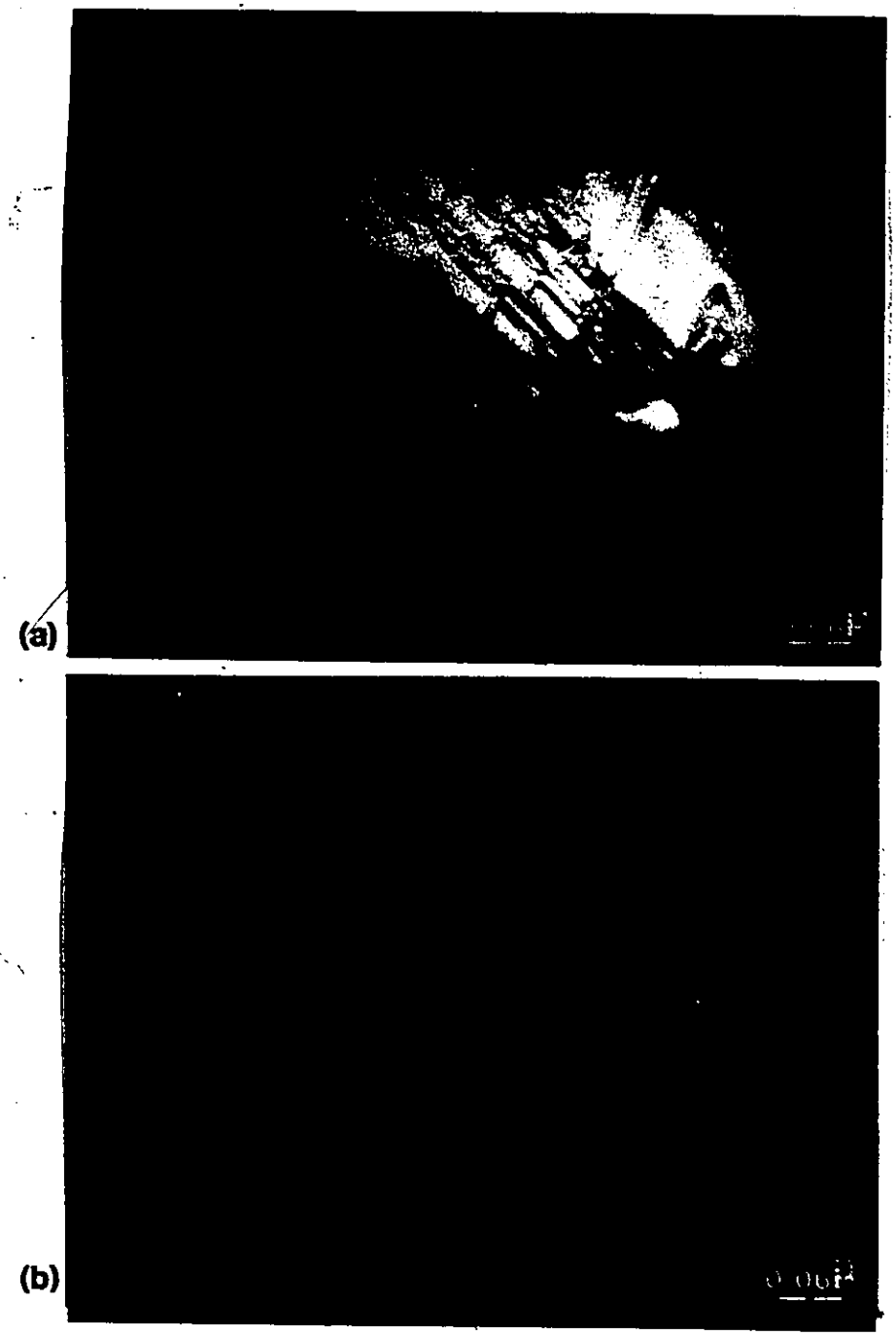

Figure 32: The micrographs for 3R structure in Zircaloy-4. The micrograph is taken when a (111)* approximately parallel to incident electron beam.

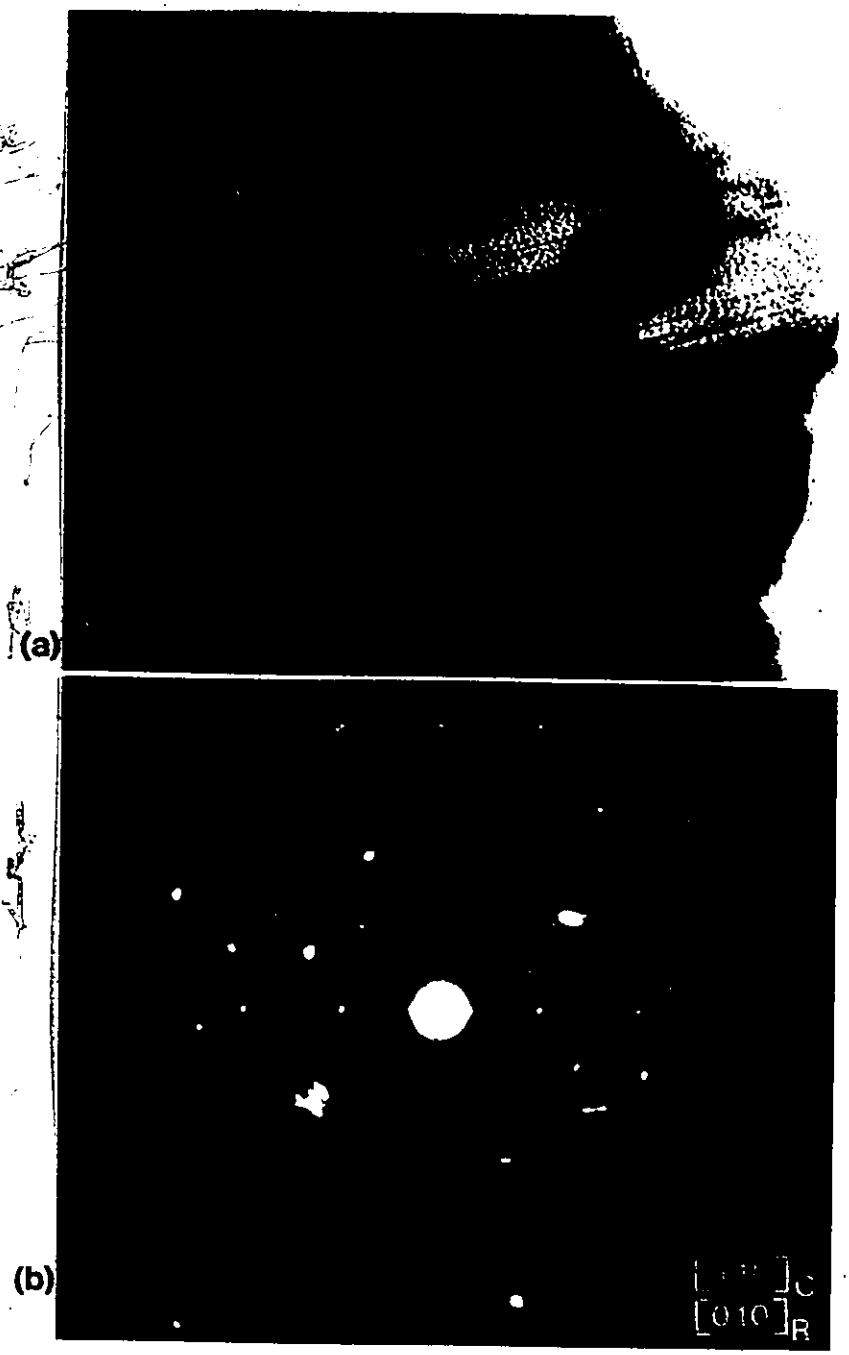

Figure 33: Lattice plane image and diffraction pattern in Zircaloy-4. (a) Lattice plane image of defect structure in $Zr(CrFe)_2$ Laves phase show stacking faults; (b) The indexing based on cubic and rhombohedral systems.

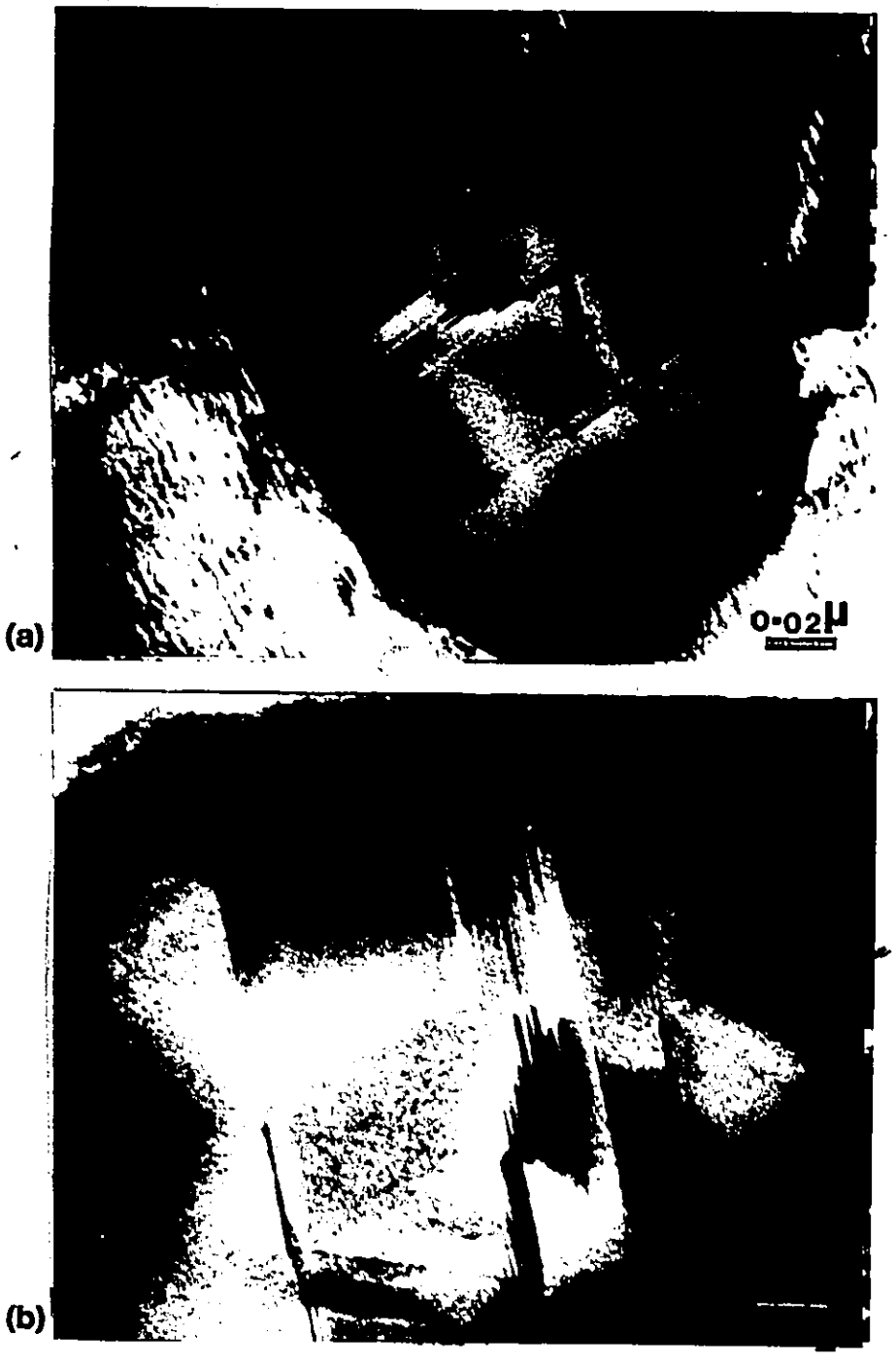

Figure 34: Lattice images for 3R twinning in the Zr-Cr-Fe alloy. The arrows indicate dislocations.

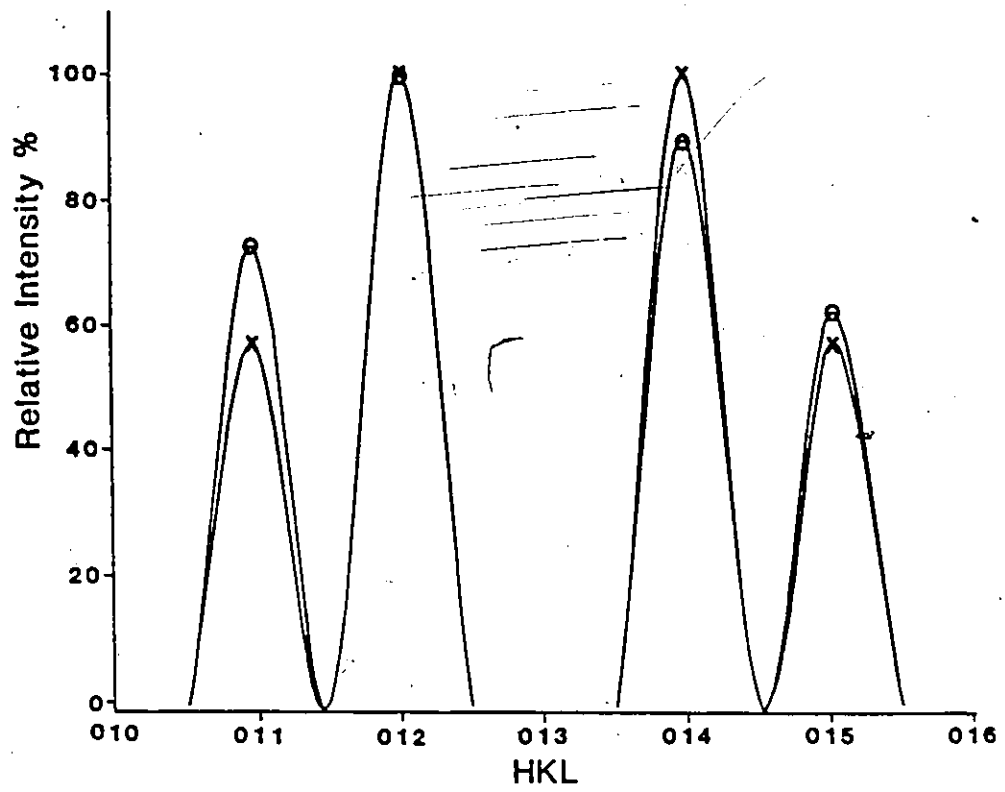

(a)

Figure 35: The distribution of relative intensities for the 01L reflaction. For (a) 3R twinned; and (b) 8H structure in the Laves phases. O - Obseved relative intensity, X - Calculated.

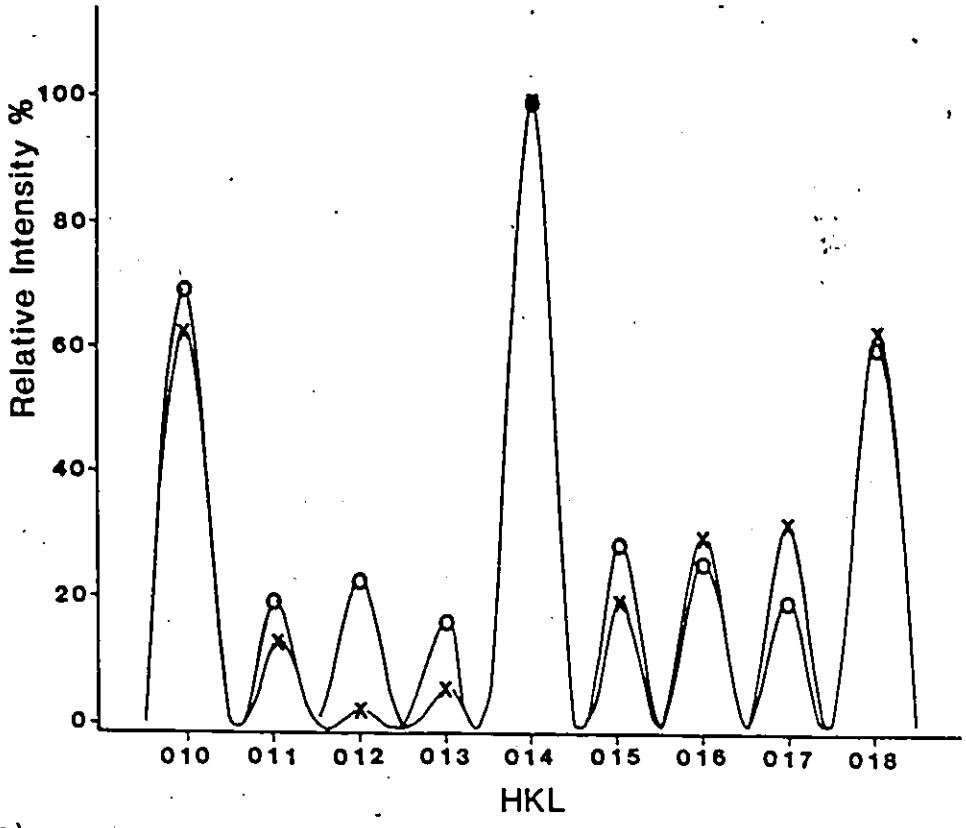
Relative Intensity %
100
80
60
40
20
0
010
011
012
013
014
015
016
017
018
HKL

(b)

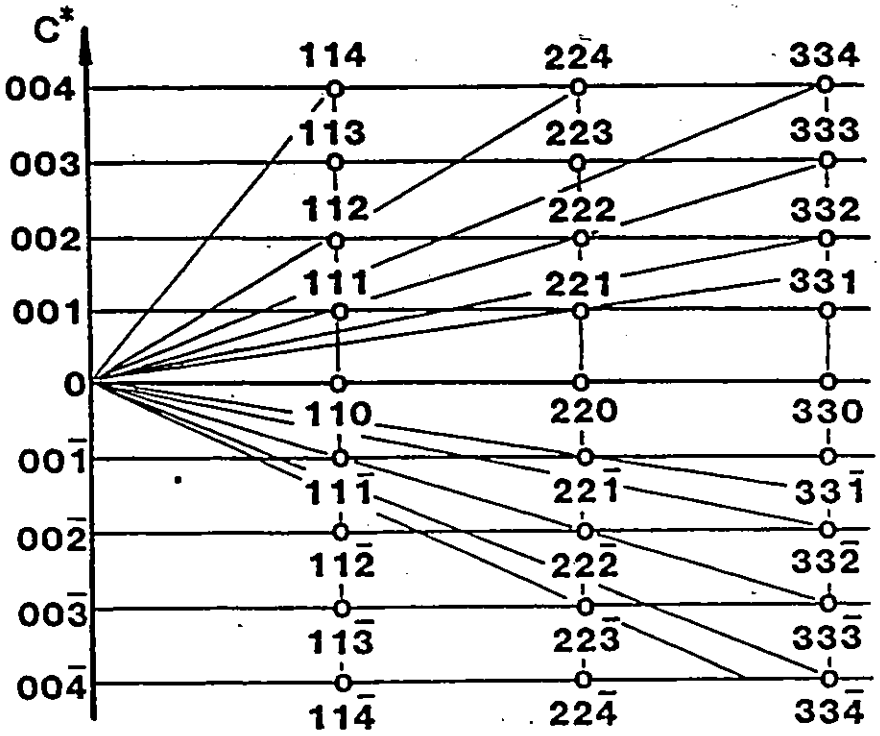

Figure 36: Projection of reciprocal lattice down $[1\bar{1}0]^*$ for hexagonal lattice $ZrCr_2$ phase.

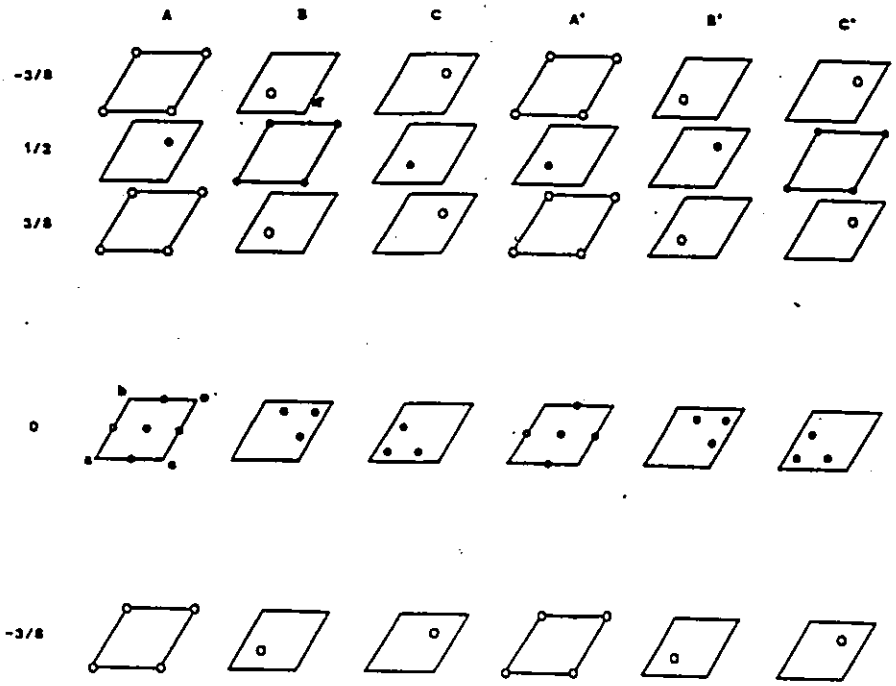

Figure 37: The fundamental stacking structures of M and M' atoms in Laves phases. The numbers show the distance between the layers.

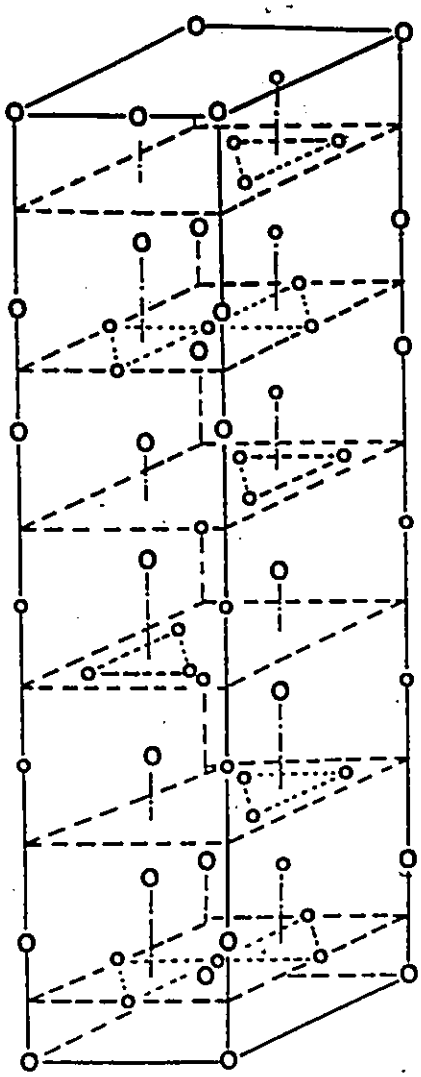

(a)

Figure 38: The structures in the $ZrCr_2$ Laves phase. (a) 6H, (b) 8H, (c) 12H and (d) 14H structures.

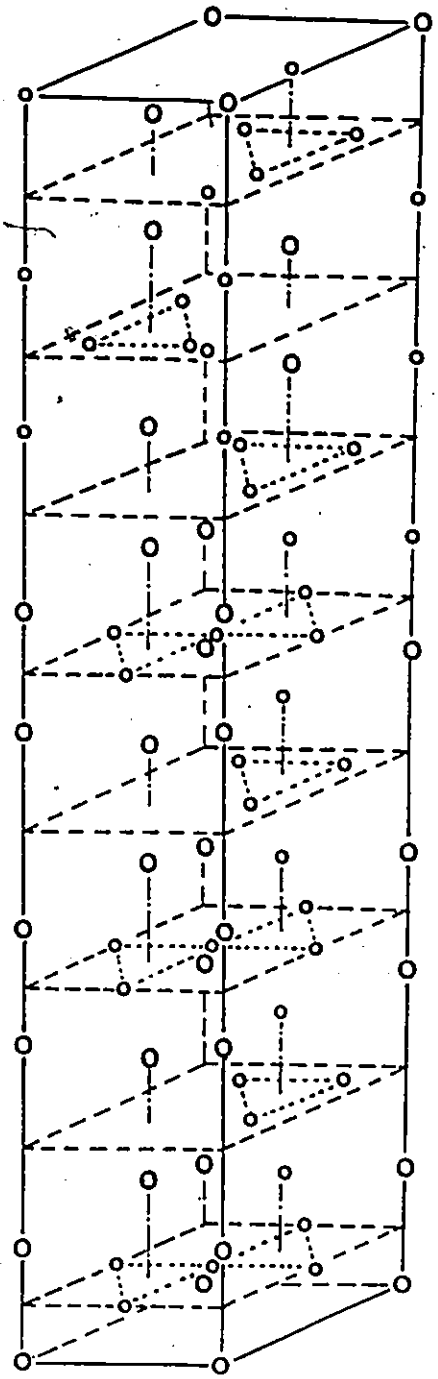

(b)

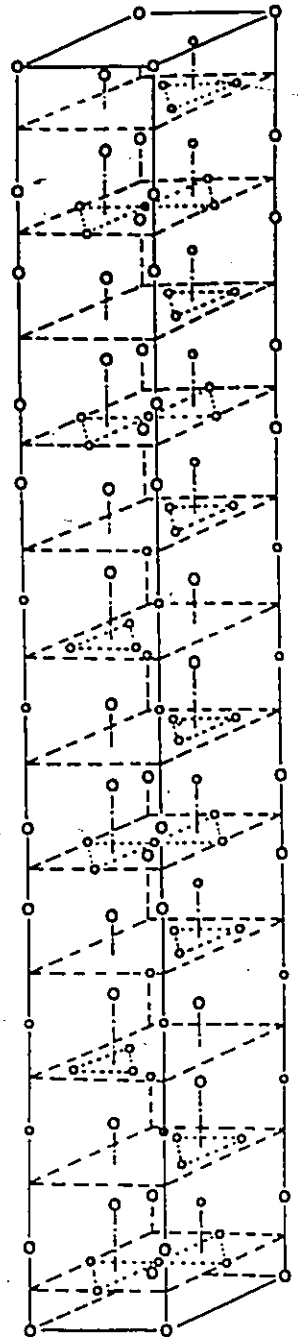

(c)

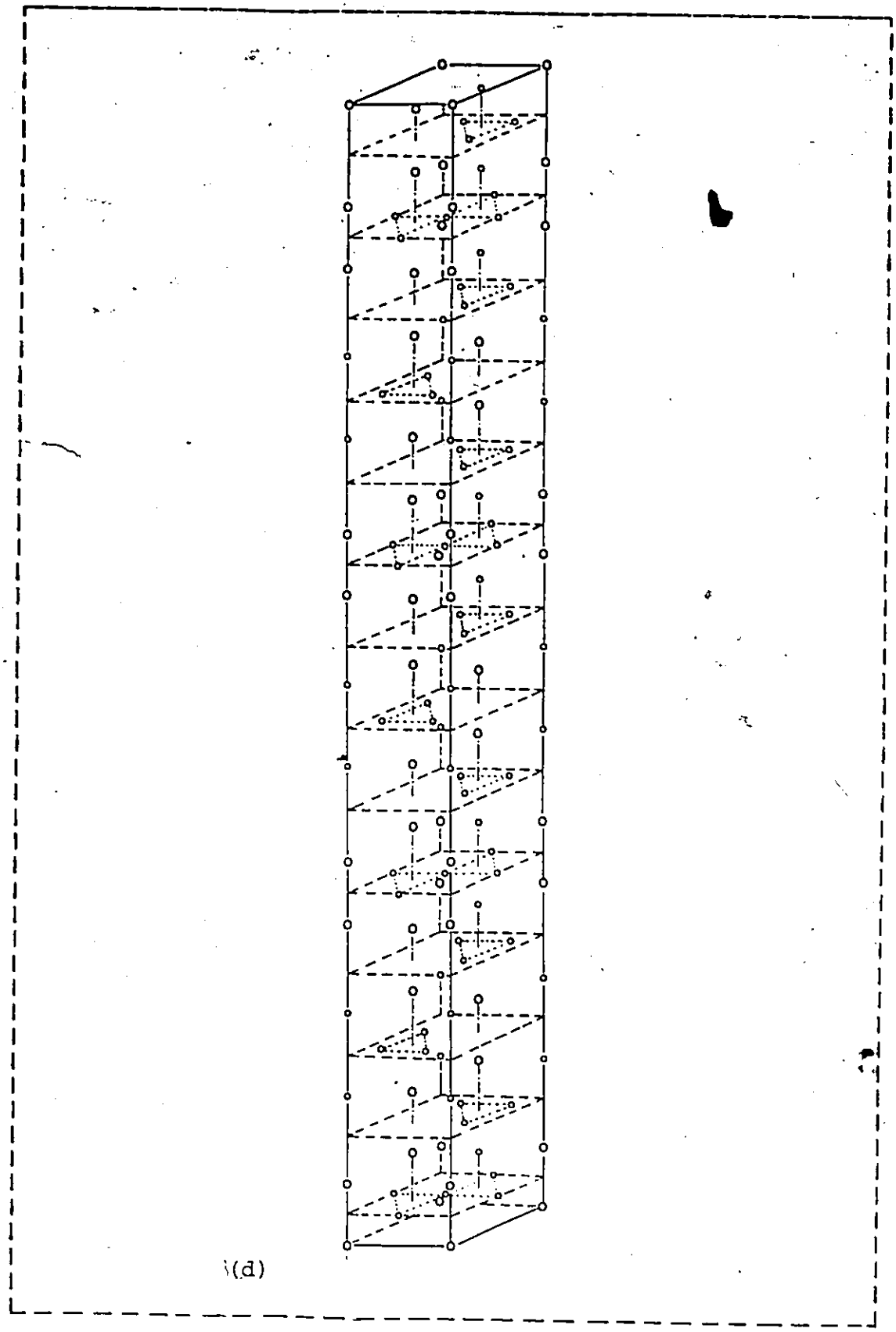

(d)

Table 1: Summary of data for binary zirconium Laves phases

MM'	Crystal Type	Parameters (Å) a	c	$D_M/D_{M'}^*$	Melting Temp. (°C)
$ZrCo_2$	$MgCu_2$	6.940		1.277	1560
$ZrCr_2$	$MgCu_2$	7.193		1.244	1700
$ZrCr_2$	$MgZn_2$	5.092	8.222	1.244	1700
$ZrFe_2$	$MgCu_2$	7.056		1.267	1645
$ZrMn_2$	$MgZn_2$	5.099	8.233	1.224	1340
$ZrMo_2$	$MgCu_2$	7.581		1.140	1880
ZrV_2	$MgCu_2$	7.43		1.181	1740
ZrW_2	$MgCu_2$	7.600		1.135	2175

* D_M and $D_{M'}$ --The diameter of M and M' atoms.

Table 2: The electron:atom ratios for binary zirconium Laves phases

Structure	Electron:Atom Ratio Calculated	Theoretical
ZrV_2	2.54	>2.32
$ZrCr_2$	2.21	<2.32, >1.80
$ZrMn_2$	1.98	<2.32, >1.80
$ZrFe_2$	1.70	<1.80
$ZrCo_2$	1.56	<1.80
Zr+0.6 Fe+1.4 V	2.29	2.32
Zr+1.8 Fe+0.2 V	1.77	1.80
Zr+0.4 Co+1.6 V	2.35	2.32
Zr+1.5 Co+0.5 V	1.81	1.80
Zr+0.8 Mn+1.2 V	2.32	2.32
Zr+0.6 Cr+1.4 Co	1.76	1.80
Zr+1.8 Cr+0.2 V	2.24	2.32

Table 3: The hydrogen capacities and sorption conditions for zirconium Laves phases

Laves Phase	Hydrogen Capacity (N atoms/molecule)	Activation Temp. (°C)	Absorption Pressure (atm)
$ZrAl_2$	0.55	700	60
ZrV_2	5.5	20	50
$ZrCr_2$	4.1	20	60
$ZrMn_2$	3.9	20	60
$ZrFe_2$	0.15	20	60
$ZrCo_2$	0.35	20	60
$ZrMo_2$	1.1	20	15

Table 4: The step height of the growth spirals and the height of the unit cell for SiC polytypes

Polytype	Interferometric Data h (Å)	X-ray Data c (Å)
6H	15±2	15.08
15R	12±2	12.5x3=37.5
33R	27±3	27.5x3=82.5
126R	102.8, 109±5	105.8x3=371.4
66H	168±3	165.88

Table 5: Known secound phases in zirconium alloys

Composition	Structure	Lattice Parameter (nm)	Heat Treatment	Reference
Zircaloy-2				
Zr-Ni-Fe	bct	a=b=0.65 c=0.55	600-700 °C 2-4 h	[47-50]
$Zr_2Ni_{0.4}Fe_{0.6}$				
$Zr_2Ni_{0.52}Fe_{0.48}$				
$Zr_2Ni_{0.5}Fe_{0.5}$				
$Zr(CrFe)_2$	hcp	a=0.51 c=0.83	600-750 °C	[49-51]
$Zr\ Fe_{0.9}Cr_{0.1}$				
$Zr(Cr_{0.6}Fe_{0.4})_2$				
$Zr_{36}Cr_{43}Fe_{21}$				
ZrCr	fcc	a=0.719		[52]
γ-hydride			600 °C 4h	[47]
Zr-Sn	orthohombic	a=0.743 b=0.582 c=0.516	750 °C 3h	[48]
Zr_5Sn_3	hexagonal	a=0.846 c=0,578		[48]
Sn	hexagonal			[48]
Sn-Ni	fcc	a=0.721	703 °C 2h	[48]
Zircaloy-4				
$Zr(Fe_{0.6}Cr_{0.4})_2$	hexagonal			[50]
$Zr_{32}Cr_{24}Fe_{44}$			702 °C 6h	[51]
$ZrCr_{0.29}Fe_{0.71}$			600 °C 2h	[48]
$Zr(CrFe)_2$				[55-59]
$Zr_xFe_5Cr_2$				[56]
$ZrCr_2$	fcc			[48]
$Zr(CrFe)_2$	amorphi-zation		Neutron irradiation at 288 °C	[54]

$Zr_2Fe_{0.85}Cr_{0.15}$				[53]
Zr-silicide	hexagonal	a=0.504 c=0.799		[57]
Zr-Cu-sulfide	amorphous			[57]
Z-phase (Zr-Fe)	hcp	a=0.79 c=0.33		[55]
$Zr_4Fe_{0.7}Cr_{0.3}$	fcc		Neutron irradiation	[54]
$Zr(FeCr)_2$				[58]
$ZrP_{0.5-1}$	orthorhombic	a=1.6715 b=2.7572 c=0.3674	1100 °C 15 min. air cooling	[53]
Zr_3P	tetragonal	a=1.07994 c=0.53545	1100 °C 15 min.	[53]
Zr_4Sn	tetragonal	a=0.69 c=1.110	1100 °C 15 min.	[60]
Zr-1%Nb				
β-Nb	bcc	a=0.345-0.357 c=0.505-0.515	600-750 °C 24 h	[47]
Zr-0.5%Nb-0.5%Cr				
$ZrCr_2$	fcc	a=0.73	600 °C 4h -quenching	[47]
Zr-1.9%Cr				
$ZrCr_2$	fcc	a=0.721		[61]
Zr-1.15%Cr-0.1%Fe				
$ZrCr_2$			1050°C 30 min. 725-800 °C 10 min.-100 h	[62-63]

Table 6: Chemical composition of Zircaloy-4 Specimens

Specimen No.	Main Alloy Elements (wt%) Sn	Fe	Cr	C	Main Impurities Content (ppm) P	Si	O	N
a	1.45	0.21	0.10	150	7	778	1380	34
b	1.50	0.193	0.085	260	60	73	1180	120
c	1.55	0.195	0.094	130	16	<25	1280	90
d	1.59	0.228	0.119	70-80	160	<20	1820	34

Table 7: Chemical analysis of Zr-1.15wt%Cr-0.1wt%Fe alloy

(wt%) Cr	Fe	O
1.14	0.08	0.110

(ppm)

Al	B	C	Cd	Co	Cu	H	Hf	Mg
<25	<0.2	90	<0.3	<5	<25	7	88	<10

Mo	N	Na	Nb	Ni	Pb	Si	Sn	Ta
<10	34	<10	<100	10	<5	40	40	<200

Ti	U	V	W	Zn
<20	<0.5	<5	<25	<50

Table 8: X-ray emission energies of Cr, Fe, Ni, Zr and their atomic scattering amplitudes for electrons

Atom	X-ray Emission Energy (KeV)						Scattering Amplitude (Å)
	K_α	K_β	K_{ab}	L_α	L_{β_1}	L_{β_2}	
Cr	5.411	5.924	5.987				4.625
Fe	6.398	7.057	7.111				4.861
Ni	7.471	8.263	8.331				4.654
Zr	15.744	17.660	17.995	2.042	2.124	2.219	7.400

Table 9: A Comparison between calculated and experimentally observed interplanar angles for $Zr(CrFe)_2$ Laves phase

Crystal Planes	Interplanar Angle ($\overset{\circ}{\alpha}$)	
	Measured	Calculated
(321)*-(211)*	10.9	10.9
(211)*-(523)*	8.1	6.6
(523)*-(312)*	3.2	4.3
(312)*-(413)*	5.0	5.2
(413)*-(110)*	46.8	52.0
(110)*-(341)*	14.8	13.9
(341)*-(231)*	4.6	5.9
(231)*-(121)*	12.0	10.9
(110)*-(121)*	31.3	30.0

Table 10: Relative intensities of 8H, 12H and 14H polytypes of $ZrCr_2$ Laves phases

HKL	8H (AB'AB'ABC'B')		12H (ABC'B'AEC'B' AB'AB')		14H (ABC'B'AEC'B'ABC'B ABC'B'AB')	
	I(cal)	I(obs)	I(cal)	I(obs)	I(cal)	I(obs)
010	62.8	68.8	33.6	32.7	27.5	30.0
011	12.3	18.9	5.0	5.3	1.3	4.9
012	2.2	23.1	2.1	4.4	1.4	6.2
013	5.0	16.0	1.5	64.1	3.7	45.5
014	100.0	100.0	0.7	2.2	0.2	17.0
015	19.8	28.8	1.2	28.1	0.1	22.5
016	30.2	26.2	100.0	100.0	0.4	11.2
017	32.2	20.2	6.6	24.6	100.0	100.0
018	62.5	60.7	9.6	25.3	1.4	27.8
019			47.1	43.6	4.3	27.2
0110			12.7	10.5	41.9	63.1
0111			12.0	6.5	47.2	11.4
0112			39.7	34.4	6.1	2.7
0113					2.8	2.7
0114					31.6	38.5

Table 11: Relative intensities of 3R twinned structure

HKL	ABC		A'C'B'	
	I(cal)	I(obs)	I(cal)	I(obs)
010	0.0	0.0	0.0	0.0
011	0.0	0.0	56.4	71.9
012	100.0	100.0	0.0	0.0
013	0.0	0.0	0.0	0.0
014	0.0	0.0	100.0	89.7
015	56.4	61.5	0.0	0.0
016	0.0	0.0	0.0	0.0

Table 12: Polytypes of $Zr(CrFe)_2$ Laves phases

Polytype[1]	Structure[2]	Alloy[3]
2H	2: AB	$ZrCr_2$
		$Zr(CrFe)_2$
3R	3: ABC	$Zr(CrFe)_2$*
3R TWIN	3: ABC and A'C'B'	$Zr(CrFe)_2$**
4H	121: AB'A'C	$ZrCr_2$
6H	2211: AEC'B'AB'	$Zr(CrFe)_2$*
8H	111122: AB'AB'ABC'B'	$ZrCr_2$
10H	11121121: AB'AB'A'CA'CAB'	$Zr(CrFe)_2$*
12H	22221111: AEC'B'ABC'B'AB'AB'	$ZrCr_2$
14H	22222211: AEC'B'ABC'B'ABC'B'AB'	$ZrCr_2$

1. H - Hexagonal lattice, R - Rhombohedral, the numbers n befor H or R - n layered repeat period along C axis.
2. The numbers represent the layer numbers in a unit cell.
3. * - in Zircaloy-4, ** - in Zr-Cr-Fe alloy.